Thermomechanical variational principles for dissipative materials with application to strain localization in bulk metallic glasses

Thesis by

Qiang Yang

In Partial Fulfillment of the Requirements

for the Degree of

Doctor of Philosophy

California Institute of Technology

Pasadena, California

2004

(Defended May 17)

To my parents

Acknowledgements

I would like to express my heartfelt gratitude to Professor Michael Ortiz, whose encouragement, guidance and ideas made this possible. I am thankful to Dr. Alejandro Mota, for his continuous help, collaboration and friendship. I would like also to thank Professor G. Ravichandran for his kindness, support and suggestion.

It would be not fair to forget all the people in Ortiz's group, specially Marta, Lydia, Adrian, Matt, Rena, Olivier, Puru, Marisol, Olga, Bill, Arash, Matias and Xiangbin, for their assistance and help. I would like also to express my deep thanks to Zhengrong, Xiaolan, Xin, Hualin, Lun, Zhengyu, Lan, Hongyu, and many other friends in Caltech C for sharing my happiness and giving me sincere care and encouragement in the past five years.

I will be eternally grateful to my wife, Hongmei, for her unconditional support and love.

The supports of the Department of Energy (DOE) through Caltech's ASCI Center for the Simulation of the Dynamic Response of Materials, the Materials Research Science and Engineering Center (MRSEC) program of the National Science Foundation (NSF) through Caltech's Center for the Science and Engineering of Materials (CSEM), and the Defense Science Office of DARPA through the Caltech's Center for Structural Amorphous Alloys are gratefully acknowledged.

Abstract

This thesis is concerned with variational principles for general coupled thermomechanical problems in dissipative materials including finite elastic and plastic deformation, non-Newtonian viscosity, rate sensitivity, arbitrary flow and hardening rule, as well as heat conduction. It is shown that there exists a potential function such that both the conservation of energy and balance of linear momentum are the Euler-Lagrange equations of its first variation. Inspired from the time-discretized version of the variational formulation, we present a procedure for variational thermomechanical update, which generalizes the isothermal approach under a variational thermodynamic framework. This variational formulation then serves as a basis for temperature change as well as constitutive updates.

An important application of the variational formulation is to optimize the shear band thickness in strain localization processes. We show that this optimization takes the form of a configurational-force equilibrium and results in a well-defined band thickness. We further implement displacement discontinuities into a class of strain-localization finite elements. These elements consist of two surfaces, attached to the abutting volume elements, which can separate and slip relative to each other, and thus enable the accurate and efficient simulation of the dynamical formation of stain localization.

The variational formulation also leads to a finite-deformation continuum modeling of bulk metallic glasses. It is shown that the strain softening of bulk metallic glasses is due to the increase of free volume (and thus the decrease of viscosity), while temperature rise accelerates the localization of the deformation. The model reproduces the constitutive behavior of $Zr_{41.2}Ti_{13.8}Cu_{12.5}Ni_{10}Be_{22.5}$ bulk metallic glass at various strain rates and temperatures.

Contents

List of Figures

Chapter 1

Introduction

It is well known that variational principles have played an important role in mechanics. The principle of minimization of elastic potential energy, for example, can be regarded as a substitute to the Euler equations of equilibrium for an elastic body, as well as a basis for the study of stability [1]. The role of variational theory in mechanics, however, goes far beyond its use as an alternative way to formulate the differential equations. One of the key features of variational statements is that all the intrinsic characteristics are compassed in a single functional, such as the governing equations, boundary and initial conditions, and even the evolutions of internal variables. An early review on variational principles for continuum mechanics can be found in Oden and Reddy's book [1]. These variational formulations can serve not only to unify diverse fields, but also to suggest new applications such as the formulation of finite-element approximations [2] and the homogenization of inelastic microstructures [3]. Nevertheless, the most compelling aspect of variational formulations is that they provide a suitable basis for error estimation and mesh adaption, specially when they take the form of a minimum principle, for both linear [4] and nonlinear problems [5, 6, 7, 8, 9].

While variational principles for quasi-static or dynamic viscoelastic boundary value problems are well understood [1], they have also been recently advanced for elastoplastic problems [10, 11, 12]. In particular, Ortiz and Stainier [12] developed a class of variational constitutive updates for general viscoplastic solids including such aspects of material behavior as finite elastic and plastic deformation, non-Newtonian viscosity, rate-sensitivity and arbitrary flow and hardening rules. The distinguishing characteristic of these constitutive updates is that, by construction, the corresponding incremental stress-strain relations derive from a pseudo-elastic stain-energy density, and the incremental deformation mapping follows from a minimum principle. This approach,

however, is limited to the isothermal process by addressing the multi-physics aspects based on a staggered procedure, i.e., during a mechanical step the internal variables governed by nonlocal kinetics such as temperature and entropy are held constant at known values.

A variational formulation for the strong coupling of thermomechanical boundary value problems has been sought for, which could serve as a basis not only for constitutive updates but also for the heat equation which governs the evolution of temperature. Since the first derivation of a variational principle for coupled thermoelastic problems by Biot [13], extensive studies have been conducted on coupled thermoelastic (and possible thermoviscoelastic) problems, e.g., [14, 15, 16]. Nevertheless, the variational formulations are comparatively less developed in the context of coupled thermodynamic problems in dissipative materials, see the work of Simo and Miehe [17], Armero and Simo [18]. The variational formulations, for example, used for mixed finite element analysis in [17], were presented in weak forms for equilibrium equations and did not form a minimum principle.

In Chapter 2, we propose a variational principle for general dissipative materials, including finite elastic and plastic deformation, non-Newtonian viscosity, rate sensitivity, arbitrary flow and hardening rule, as well as heat conduction. As a motivation, we begin with a variational formulation for thermoelastic materials in rate form by recourse to Vainberg's theorem [19]. This formulation is then extended to general thermoelasto-viscoplastic materials, resulting in a variational form for thermomechanical equations. Inspired from the time-discretized version of the variational formulation, we present a procedure for a variational thermomechanical update, which generalizes the isothermal approach of Ortiz and Stainier [12] under a variational thermodynamic framework. Based on the variational formulation, the heat equation for thermoelasto-viscoplastic materials is then studied as one of the Euler-Lagrange equations obtained from the first variation of an energy potential, and the temperature rise thus calculated in a one-dimensional case is compared with experimental data [20]. In addition, we will discuss briefly the energy-momentum tensor and its configurational forces introduced by the existence of a thermal potential in the variational formulation.

As an important application of the variational principles, we focus our attention in Chapter 3 to strain localization problems. We regard strain localization strictly as a *sub-grid* phenomenon and, consequently, the bands of strain localization are modeled as *displacement discontinuities*.

As is evident from dimensional considerations alone, the transformation of displacement jumps into a deformation gradient requires the introduction of a length parameter, namely, the band thickness. Based on an incremental variational principle, the band thickness is optimized in terms of minimizing the effective energy in the band. We show that this optimization takes the form of a configurational-force equilibrium and results in a well-defined band thickness. We further implement displacement discontinuities into a class of *strain-localization elements*. These elements consist of two surfaces, attached to the abutting volume elements, which can separate and slip relative to each other. The kinematics of the strain-localization elements is identical to the kinematics of cohesive elements proposed by Ortiz and Pandolfi [21] for the simulation of fracture. We then demonstrate the predictive ability of the approach by means of simulations of Guduru *et al.* [22] dynamic shear-band tests in pre-notched C300 steel specimens.

The variational formulation so obtained can also be used to model the constitutive equations for systems with complex microstructures such as sub-grid microstructure in martensitic materials [23] and subgrain-dislocation structures in metallic crystals [24, 25]. In Chapter 4, we present a variational finite-deformation continuum model for bulk metallic glasses. The micro-characteristic of these materials is that atoms are completely disordered such that lattice structures are absent [26]. According to free volume theory, the disorder in metallic glasses is characterized by free volume which then plays an important role in strain localization of bulk metallic glasses. While the temperature rise could accelerate the failure of metallic glasses, we show that the decrease of viscosity in bulk metallic glasses is a result of free volume increasing. The developed continuum model is then used to describe the constitutive behavior of $Zr_{41.2}Ti_{13.8}Cu_{12.5}Ni_{10}Be_{22.5}$ (Vitreloy 1) bulk metallic glass at various strain rates and temperatures, with excellent agreement between the numerical results and experimental data [27]. Further validation is obtained by finite element simulation of shear banding in a Vitreloy 1 plate subjected to symmetric bending [28].

Chapter 2

A variational formulation of thermomechanical updates

2.1 Introduction

Real systems always exhibit multi-physics phenomena. Those behaviors are normally coupled and governed by certain governing equations. In some cases, they can also be described by introducing variational minimum principles [1]. Having a variational formulation for coupled boundary value problems has attracted much interest from engineers, scientists and researchers. In particular, a variational formulation for coupled thermomechanical updates has been sought for the numerical investigation of history-dependent constitutive relations in computational plasticity.

This chapter is concerned with the development of a variational formulation for general dissipative materials including finite elastic and plastic deformation, non-Newtonian viscosity, rate-sensitivity, arbitrary flow and hardening rules, as well as heat conduction. This formulation generalizes the isothermal approach by Ortiz and Stainier [12] who developed a variational formulation for viscoplastic constitutive updates. The distinguishing characteristic of the proposed thermomechanical updates is that, by construction, the corresponding incremental stress-strain relations as well as entropy-temperature relations derive from a pseudo-thermoelastic strain-energy density.

The formulation begins with thermoelastic materials in which a variational energy potential function is proposed, by recourse to Vainbeig's theorem [19], such that the conservation of energy as well as the linear momentum balance are Euler-Lagrange equations of this potential function. After extending the formulation to general thermoelasto-viscoplastic materials, we present a time-discretized formulation for variational thermomechanical update, which indeed returns to the rate

form when time step approaching to zero.

As an example, we then focus on the temperature update governed by the heat equation which is obtained from the first variation of the energy potential. In order to compare with the experimental observation, we present a simple one-dimensional model, and the temperature rises so obtained give good agreement with experimental data [20]. Moreover, the existence of an external term, called the thermal potential, in the total energy potential, and thus in the pseudo-thermoelastic strain-energy density, introduces a *thermal* energy-momentum tensor in addition to the traditional *mechanical* Eshelby energy-momentum tensor. As a result, a thermal *J-integral* term is introduced and a simple application to crack acceleration and deceleration in a temperature-gradiented strip is conducted.

2.2 General framework

We shall be concerned with the motions and thermodynamic processes undergone by a continuous body of reference configuration $B \subset \mathbb{R}^3$. The motions of the body are described by a time-dependent deformation mapping $\boldsymbol{\varphi} : B \times [a, b] \to \mathbb{R}^3$, where $[a, b]$ is the time interval elapsed during the motion. The motions of the body obey conservation of mass

$$\frac{d}{dt} \int_U R \, dV = 0 \ , \tag{2.1}$$

conservation of linear momentum

$$\frac{d}{dt} \int_U R\boldsymbol{V} \, dV = \int_U R\boldsymbol{B} \, dV + \int_{\partial U} \boldsymbol{P}\boldsymbol{N} \, dS \ , \tag{2.2}$$

conservation of angular momentum

$$\frac{d}{dt} \int_U \boldsymbol{\varphi} \times (R\boldsymbol{V}) \, dV = \int_U \boldsymbol{\varphi} \times (R\boldsymbol{B}) \, dV + \int_{\partial U} \boldsymbol{\varphi} \times (\boldsymbol{P}\boldsymbol{N}) \, dS \ , \tag{2.3}$$

the first law of thermodynamics

$$\begin{aligned} &\frac{d}{dt} \int_U RE \, dV + \frac{d}{dt} \int_U \frac{1}{2} R|\boldsymbol{V}|^2 \, dV = \\ &\int_U R\boldsymbol{B} \cdot \boldsymbol{V} \, dV + \int_{\partial U} (\boldsymbol{P}\boldsymbol{N}) \cdot \boldsymbol{V} \, dS + \int_U RS \, dV - \int_{\partial U} \boldsymbol{H} \cdot \boldsymbol{N} \, dS \ , \end{aligned} \tag{2.4}$$

and the second law of thermodynamics

$$\frac{d}{dt}\int_U RN\,dV - \int_U \frac{RS}{T}\,dV + \int_{\partial U} \frac{\boldsymbol{H}\cdot\boldsymbol{N}}{T}\,dS \geq 0\ , \tag{2.5}$$

where $U \subset B$ is an arbitrary subbody; R is the mass density per unit undeformed volume; $\boldsymbol{V} = \dot{\boldsymbol{\varphi}}$ is the material velocity; $\boldsymbol{B}$ is the body force density per unit mass; $\boldsymbol{N}$ is the unit outward normal; $\boldsymbol{P}$ is the first Piola-Kirchhoff stress tensor; E is the internal energy per unit undeformed volume; N is the entropy per unit undeformed volume; T is the absolute temperature; S is the distributed heat source per unit mass; and $\boldsymbol{H}$ is the outward heat flux. Alternatively, these conservation laws can be expressed in local form as:

$$\dot{R} = 0\ , \tag{2.6a}$$

$$R\dot{\boldsymbol{V}} = \mathrm{Div}\boldsymbol{P} + R\boldsymbol{B}\ , \tag{2.6b}$$

$$\boldsymbol{P}\boldsymbol{F}^T = \boldsymbol{F}\boldsymbol{P}^T\ , \tag{2.6c}$$

$$\dot{E} = \boldsymbol{P}\cdot\dot{\boldsymbol{F}} + RS - \mathrm{Div}\boldsymbol{H}\ , \tag{2.6d}$$

$$\dot{\Gamma} \equiv \dot{N} - \frac{RS}{T} + \mathrm{Div}\frac{\boldsymbol{H}}{T} \geq 0\ , \tag{2.6e}$$

where $\boldsymbol{F} = \mathrm{Grad}\boldsymbol{\varphi}$ is the deformation gradient; $\dot{\Gamma}$ is the internal entropy production rate per unit undeformed volume.

In addition, we suppose that the *local thermodynamic state* of an infinitesimal material neighborhood is defined by: the local deformation gradient $\boldsymbol{F} \in GL_+(3,\mathbb{R}) \equiv$ the Lie group of invertible and orientation preserving linear transformations in $\mathbb{R}^3$; the local entropy density per unit undeformed volume $N \in \mathbb{R}$; and a collection $\boldsymbol{Z} \in M$ of additional or *internal variables*. The set M in which $\boldsymbol{Z}$ take values varies depending on the material class and cannot be specified universally. Depending on the nature of the internal variables, M may be: a vector space; a manifold, e.g., if the internal processes are subject to holonomic constraints; or a Lie group, e.g., if the internal variables are naturally composed by matrix multiplication. In addition, the attainable internal variable rates may be subject to non-holonomic constraints of the type

$$\boldsymbol{L}(\boldsymbol{Z})\dot{\boldsymbol{Z}} = \boldsymbol{0}\ . \tag{2.7}$$

We shall assume that the internal energy density and the absolute temperature are functions of the local state, i.e.,

$$E = E(\boldsymbol{F}, N, \boldsymbol{Z}) \ , \tag{2.8a}$$

$$T = T(\boldsymbol{F}, N, \boldsymbol{Z}) \ . \tag{2.8b}$$

The equilibrium stresses and the thermodynamic driving forces conjugate to the internal variables are, by definition,

$$\boldsymbol{P}^e \equiv \partial_{\boldsymbol{F}} E(\boldsymbol{F}, N, \boldsymbol{Z}) \ , \tag{2.9a}$$

$$\boldsymbol{Y} \equiv -\partial_{\boldsymbol{Z}} E(\boldsymbol{F}, N, \boldsymbol{Z}) \ . \tag{2.9b}$$

The viscous or non-equilibrium stress is then

$$\boldsymbol{P}^v \equiv \boldsymbol{P} - \boldsymbol{P}^e \ . \tag{2.10}$$

A theorem of Coleman and Noll [29] then shows that (2.8b) is necessarily of the form

$$T = \partial_N E(\boldsymbol{F}, N, \boldsymbol{Z}) \ , \tag{2.11}$$

and that all processes must comply with the dissipation inequality

$$\boldsymbol{Y} \cdot \dot{\boldsymbol{Z}} + \boldsymbol{P}^v \cdot \dot{\boldsymbol{F}} - \frac{1}{T} \boldsymbol{H} \cdot \mathrm{Grad} T \geq 0 \ . \tag{2.12}$$

Alternatively, one may introduce the Helmholtz free energy by applying the Legendre transformation

$$A(\boldsymbol{F}, T, \boldsymbol{Z}) = \inf_N \left\{ E(\boldsymbol{F}, N, \boldsymbol{Z}) - TN \right\} \ , \tag{2.13}$$

in terms of which the equilibrium relations take the form

$$N = -\frac{\partial A}{\partial T}(\boldsymbol{F}, T, \boldsymbol{Z}) \ , \tag{2.14a}$$

$$\boldsymbol{P}^e = \frac{\partial A}{\partial \boldsymbol{F}}(\boldsymbol{F}, T, \boldsymbol{Z}) \ , \tag{2.14b}$$

$$\boldsymbol{Y} = -\frac{\partial A}{\partial \boldsymbol{Z}}(\boldsymbol{F}, T, \boldsymbol{Z}) \ . \tag{2.14c}$$

Example 2.2.1. *State function for thermoelastic-plastic materials*

A theory of thermoelastic-viscoplastic materials may be based on a multiplicative decomposition of the deformation gradient $\boldsymbol{F}$ of the form [30]

$$\boldsymbol{F} = \boldsymbol{F}^e \boldsymbol{F}^p \ , \tag{2.15}$$

into an elastic part $\boldsymbol{F}^e$ and a plastic part $\boldsymbol{F}^p$. For metals, one may further assume that the elasticity and the specific heat of the material are independent of the internal processes. This leads to a free energy of the form [12]:

$$A(\boldsymbol{F}^e, T, \boldsymbol{F}^p, \boldsymbol{Z}) = W^e(\boldsymbol{F}^e, T) + W^p(T, \boldsymbol{F}^p, \boldsymbol{Z}) + RC_v T \left(1 - \log \frac{T}{T_0}\right) \ , \tag{2.16}$$

where W^e is the elastic strain-energy density, W^p is the stored energy of cold work, $\boldsymbol{Z}$ is a collection or hardening variables depending on the material type [31], C_v is the specific heat per unit mass at constant volume and T_0 is a reference temperature. In this setting, the complete set of internal variables is $\{\boldsymbol{F}^p, \boldsymbol{Z}\}$. The plastic deformation $\boldsymbol{F}^p$ must define an invertible orientation-preserving local deformation, and hence the natural domain of $\boldsymbol{F}^p$ is the multiplicative Lie group $GL_+(3, \mathbb{R})$. By material-frame indifference, it follows that W^e can only depend on $\boldsymbol{F}^e$ through the elastic right-Cauchy Green deformation tensor:

$$\boldsymbol{C}^e = \boldsymbol{F}^{eT} \boldsymbol{F}^e = \boldsymbol{F}^{p-T} \boldsymbol{C} \boldsymbol{F}^{p-1} \ , \tag{2.17}$$

whereupon (2.16) simplifies to

$$A(\boldsymbol{F}, T, \boldsymbol{F}^p, \boldsymbol{Z}) = W^e(\boldsymbol{C}^e, T) + W^p(T, \boldsymbol{F}^p, \boldsymbol{Z}) + RC_v T \left(1 - \log \frac{T}{T_0}\right) \ . \tag{2.18}$$

□

Example 2.2.2. *Flow rules*

Examples of internal variable set arise in single-crystal plasticity, where $\boldsymbol{Z} = \{\gamma_1, \ldots, \gamma_N\}$, γ_α is the slip strain on slip system α, and the rules of crystallographic slip require that [12, 32]

$$\dot{\boldsymbol{F}}^p \boldsymbol{F}^{p-1} - \sum_{\alpha=1}^{N} \dot{\gamma}_\alpha \boldsymbol{s}_\alpha \otimes \boldsymbol{m}_\alpha = \boldsymbol{0} \ , \tag{2.19}$$

where $(\boldsymbol{s}_\alpha, \boldsymbol{m}_\alpha)$ are orthogonal unit vectors characteristic of the crystal class. Evidently, the flow rule (2.19) is of the general form (2.7).

Another familiar example is provided by isotropic J_2-flow theory of plasticity [12]. In this case, $\boldsymbol{Z} = \{\varepsilon^p\}$, where ε^p is the effective plastic strain, and the Prandtl-Reuss flow rule of plastic deformation requires

$$\mathrm{tr}(\dot{\boldsymbol{F}}^p \boldsymbol{F}^{p-1}) = 0 \ , \tag{2.20a}$$

$$||\dot{\boldsymbol{F}}^p \boldsymbol{F}^{p-1}||^2 - \frac{3}{2}|\dot{\varepsilon}^p|^2 = 0 \ , \tag{2.20b}$$

which are also of the general form (2.7). □

In order to obtain a closed set of governing equations defining well-posed initial boundary-value problems, the equilibrium relations summarized above need to be supplemented with appropriate kinetic relations enabling the determination of $\boldsymbol{P}^v$, $\boldsymbol{H}$ and $\dot{\boldsymbol{Z}}$. A general form of the kinetic equations is suggested by the dissipation inequality (2.12). Start by grouping the quantities appearing in this inequality into a collection of *thermodynamic forces*:

$$\boldsymbol{X} = \{\dot{\boldsymbol{Z}}, \dot{\boldsymbol{F}}, \boldsymbol{G}\} \ , \tag{2.21}$$

where $\boldsymbol{G} = -T^{-1}\mathrm{Grad}T$, and *thermodynamic fluxes*:

$$\boldsymbol{J} = \{\boldsymbol{Y}, \boldsymbol{P}^v, \boldsymbol{H}\} \ . \tag{2.22}$$

The dissipation inequality now takes the form

$$T\dot{\Gamma} = \boldsymbol{X} \cdot \boldsymbol{J} \geq 0 \ . \tag{2.23}$$

We note that the classification of variables into forces and fluxes is, to a large extent, a matter of convenience and convention.

Suppose now that the thermodynamic fluxes are determined by the local thermodynamic forces and, possible, the local thermodynamic state. Then we may write

$$\boldsymbol{J} = \boldsymbol{J}(\boldsymbol{X}; \boldsymbol{F}, T, \boldsymbol{Z}) \ . \tag{2.24}$$

We shall assume that

$$\boldsymbol{J} = \boldsymbol{J}(\boldsymbol{0}; \boldsymbol{F}, T, \boldsymbol{Z}) = \boldsymbol{0} \ , \tag{2.25}$$

i.e., that there are no internal processes when the driving forces vanish, and the regularity property

$$\boldsymbol{J}(\boldsymbol{X}; \boldsymbol{F}, T, \boldsymbol{Z}) = o(|\boldsymbol{X}|) \ , \tag{2.26}$$

i.e., that the dissipation is negligible for thermodynamic processes close to equilibrium. If, in addition, the *Onsager reciprocity relations*

$$\frac{\partial J_i}{\partial X_j} = \frac{\partial J_j}{\partial X_i} \ , \tag{2.27}$$

then it follows that a scalar *kinetic potential* $\Delta(\boldsymbol{X}; \boldsymbol{F}, T, \boldsymbol{Z})$ exists such that

$$\boldsymbol{J} = \partial_{\boldsymbol{X}} \Delta(\boldsymbol{X}; \boldsymbol{F}, T, \boldsymbol{Z}) \ . \tag{2.28}$$

The general kinetic relations just formulated allow for fully nonlinear and coupled rate, viscosity

and heat conduction relations.

Example 2.2.3. *Rate-sensitivity*

Consider a thermoelastic-plastic material such as described in example 2.2.1. Suppose that a kinetic potential $\psi(\boldsymbol{Y}, T)$ exists such that

$$\dot{\boldsymbol{Z}} = \partial_{\boldsymbol{Y}} \psi(\boldsymbol{Y}, T) \ . \tag{2.29}$$

Introduce the dual potential

$$\psi^*(\dot{\boldsymbol{Z}}, T) = \sup_{\boldsymbol{Y}} \{\boldsymbol{Y} \cdot \dot{\boldsymbol{Z}} - \psi(\boldsymbol{Y}, T)\} \tag{2.30}$$

with the property that

$$\boldsymbol{Y} = \partial_{\dot{\boldsymbol{Z}}} \psi^*(\dot{\boldsymbol{Z}}, T) \ . \tag{2.31}$$

In this case we have $\boldsymbol{X} = \dot{\boldsymbol{Z}}$, $\boldsymbol{J} = \boldsymbol{Y}$ and $\Delta = \psi^*$. □

Example 2.2.4. *Newtonian viscosity*

A continuum is said to have Newtonian viscosity if the viscous part of the Cauchy stress tensor

$$\boldsymbol{\sigma}^v = \zeta(T) \mathrm{tr}(\boldsymbol{d}) \boldsymbol{I} + 2\eta(T) \boldsymbol{d} \ , \tag{2.32}$$

where

$$\boldsymbol{d} = \mathrm{sym}(\dot{\boldsymbol{F}} \boldsymbol{F}^{-1}) \tag{2.33}$$

is the rate of deformation tensor, and $\zeta(T)$ and $\eta(T)$ are viscosity parameters. The viscosity law (2.32) may be expressed explicitly as a function of $\dot{\boldsymbol{F}}$ and $(\boldsymbol{F}, T)$ in the form

$$\boldsymbol{\sigma}^v(\dot{\boldsymbol{F}}; \boldsymbol{F}, T) = \zeta(T) \mathrm{tr}(\dot{\boldsymbol{F}} \boldsymbol{F}^{-1}) \boldsymbol{I} + \eta(T)(\dot{\boldsymbol{F}} \boldsymbol{F}^{-1} + \boldsymbol{F}^{-T} \dot{\boldsymbol{F}}^T) \ . \tag{2.34}$$

The corresponding viscous part of the first Piola-Kirchoff stress tensor is

$$\boldsymbol{P}^v(\dot{\boldsymbol{F}}; \boldsymbol{F}, T) = J \boldsymbol{\sigma}^v(\dot{\boldsymbol{F}}; \boldsymbol{F}, T) \boldsymbol{F}^{-T} \ , \tag{2.35}$$

where $J = \det(\boldsymbol{F})$ is the Jacobian determinant of deformation gradient $\boldsymbol{F}$. A simple calculation shows that the Newtonian viscosity law possesses the potential structure

$$\boldsymbol{P}^v = \partial_{\dot{\boldsymbol{F}}}\phi(\dot{\boldsymbol{F}}, \boldsymbol{F}, T) \ , \tag{2.36}$$

where the viscous potential per unit undeformed volume is

$$\phi(\dot{\boldsymbol{F}}, \boldsymbol{F}, T) = J \left\{ \frac{\zeta(T)}{2} \mathrm{tr}(\boldsymbol{d})^2 + \eta(T)\boldsymbol{d} \cdot \boldsymbol{d} \right\} \ . \tag{2.37}$$

In this case we have $\boldsymbol{X} = \dot{\boldsymbol{F}}$, $\boldsymbol{J} = \boldsymbol{P}^v$ and $\Delta = \phi$. □

Example 2.2.5. *Heat conduction*

Let

$$\boldsymbol{G} = -\mathrm{Grad} \log(\frac{T}{T_0}) = -\frac{1}{T}\mathrm{Grad}T \tag{2.38}$$

for some reference temperature T_0, and if a Fourier potential $\chi(\boldsymbol{G}, T)$ exists such that

$$\boldsymbol{H} = \partial_{\boldsymbol{G}}\chi(\boldsymbol{G}, T) \ , \tag{2.39}$$

in this case, we have $\boldsymbol{X} = \boldsymbol{G}$, $\boldsymbol{J} = \boldsymbol{H}$ and $\Delta = \chi$. □

Example 2.2.6. *Uncoupled rate sensitivity, viscosity and heat conduction*

The case in which rate sensitivity, viscosity and heat conduction are all operative but uncoupled is characterized by the kinetic potential

$$\Delta = \psi^*(\dot{\boldsymbol{Z}}, T) + \phi(\dot{\boldsymbol{F}}, \boldsymbol{F}, T) + \chi(\boldsymbol{G}, T) \ . \tag{2.40}$$

The total dissipation is therefore given by

$$T\dot{\Gamma} = \boldsymbol{X} \cdot \boldsymbol{J} = \boldsymbol{Y} \cdot \dot{\boldsymbol{Z}} + \boldsymbol{P}^v \cdot \dot{\boldsymbol{F}} + \boldsymbol{G} \cdot \boldsymbol{H} \ . \tag{2.41}$$

□

Specific examples of the thermodynamic and kinetic potentials introduced in the foregoing will

be given subsequently.

2.3 Variational form of the thermomechanical equations

We proceed to develop a variational restatement of the above thermomechanical equations, which will subsequently serve as a basis for the formulation of variational updates. The formulation generalizes the approach of Ortiz and Stainier [12], which was restricted to isothermal processes.

2.3.1 Thermoelastic materials

By way of motivation, we begin by considering the case of a conducting thermoelastic material characterized by an internal energy density of the form

$$E = E(\boldsymbol{F}, N) \ , \tag{2.42}$$

and the equilibrium relations of the form

$$\boldsymbol{P} = \partial_{\boldsymbol{F}} E(\boldsymbol{F}, N) \ , \tag{2.43a}$$

$$\Theta = \partial_N E(\boldsymbol{F}, N) \ , \tag{2.43b}$$

where Θ is the local equilibrium temperature defined by the local thermodynamic state. Here, we differentiate between Θ and the "external" temperature field T. At equilibrium, these two quantities will be equal everywhere, but this condition is not imposed *a priori* and will come out of the variational principle itself, in which N acts as an additional independent variable (minimizer).

In this case, the governing equations are

$$\mathrm{Div}\partial_{\boldsymbol{F}} E + R\boldsymbol{B} = \boldsymbol{0} \ , \tag{2.44a}$$

$$\dot{E} = \boldsymbol{P} \cdot \dot{\boldsymbol{F}} + RS - \mathrm{Div}\boldsymbol{H} \ , \tag{2.44b}$$

$$\partial_N E - T = 0 \ . \tag{2.44c}$$

The heat equation (2.44b) can be written in entropy form as

$$\dot{N} - \frac{RS}{\Theta} + \frac{\mathrm{Div}\boldsymbol{H}}{\Theta} = 0 \ . \tag{2.45}$$

More generally [1], we may rephrase the governing equations as

$$\mathrm{Div}\partial_{\boldsymbol{F}} E + R\boldsymbol{B} = \boldsymbol{0} \ , \tag{2.46a}$$

$$\lambda_1(\Theta, T)\dot{N} - \frac{RS}{\Theta} + \frac{\mathrm{Div}\boldsymbol{H}}{\Theta} = 0 \ , \tag{2.46b}$$

$$\partial_N E - \lambda_2(\Theta, T)T = 0 \ , \tag{2.46c}$$

where $\lambda_1(\Theta, T)$ and $\lambda_2(\Theta, T)$ are two dimensionless multipliers such that, at equilibrium state, $\lambda_1 = \lambda_2 = 1$. The temperature gradient which appears in $\boldsymbol{H}$ is computed from the "external" temperature T. The weak form of the governing equations is

$$\int_B \left(\partial_{\boldsymbol{F}} E \cdot \mathrm{Grad}\dot{\boldsymbol{v}} - R\boldsymbol{B} \cdot \dot{\boldsymbol{v}}\right) dV - \int_{\partial_D B} \bar{\boldsymbol{T}} \cdot \dot{\boldsymbol{v}} \, dS = 0 \ , \tag{2.47a}$$

$$\int_B \left(\lambda_1 \dot{N} \ \eta - \frac{RS}{\Theta} \ \eta\right) dV - \int_B \boldsymbol{H} \cdot \mathrm{Grad}\frac{\eta}{\Theta} \, dV + \int_{\partial_T B} \bar{H} \frac{\eta}{\Theta} \, dS = 0 \ , \tag{2.47b}$$

$$\int_B \left(\partial_N E \dot{n} - \lambda_2 T \dot{n}\right) \, dV = 0 \ , \tag{2.47c}$$

where $\dot{\boldsymbol{v}}$, η and $\dot{n}$ are admissible variations of $\dot{\boldsymbol{\varphi}}$, T and $\dot{N}$, respectively, i.e., variations such that

$$\dot{\boldsymbol{v}} = \boldsymbol{0}, \ \text{in} \ \partial B \backslash \partial_D B \ , \tag{2.48a}$$

$$\eta = 0, \ \text{in} \ \partial B \backslash \partial_T B \ , \tag{2.48b}$$

where $\partial_D B$ and $\partial_T B$ are displacement and temperature boundaries, respectively. Here $\dot{N}$ acts as an internal variable.

[1] Of course, the governing equations could be made more general by multiplying any non-zero arbitrary factor to each equation. Here we consider only a simple form.

Then, we obtain the residual

$$
\begin{aligned}
&b[\dot{\boldsymbol{\varphi}}, T, \dot{N}](\dot{\boldsymbol{v}}, \eta, \dot{n}) = \\
&\left\{ \begin{array}{l}
-\int_B \partial_{\boldsymbol{F}} E \cdot \mathrm{Grad}\dot{\boldsymbol{v}}\, dV + \int_B R\boldsymbol{B} \cdot \dot{\boldsymbol{v}}\, dV + \int_{\partial_D B} \bar{\boldsymbol{T}} \cdot \dot{\boldsymbol{v}}\, dS \\[2ex]
-\int_B \left(\lambda_1 \dot{N}\ \eta - \frac{RS}{\Theta}\ \eta - \boldsymbol{H} \cdot \mathrm{Grad}\frac{\eta}{\Theta} \right) dV - \int_{\partial_T B} \bar{H}\ \frac{\eta}{\Theta}\, dS \\[2ex]
-\int_B \left(\partial_N E\ \dot{n} - \lambda_2 T\ \dot{n} \right)\, dV
\end{array} \right\} = 0\ .
\end{aligned}
\tag{2.49}
$$

The linearization of these equations under perturbations of the form $\dot{\boldsymbol{\varphi}} \to \dot{\boldsymbol{\varphi}} + \dot{\boldsymbol{u}}$, $\log(T/T_0) \to \log(T/T_0) + \theta/T$ and $\dot{N} \to \dot{N} + \dot{m}$ is

$$
a[\dot{\boldsymbol{\varphi}}, T, \dot{N}](\dot{\boldsymbol{v}}, \eta, \dot{n}; \dot{\boldsymbol{u}}, \theta, \dot{m}) = D\, b[\dot{\boldsymbol{\varphi}}, T, \dot{N}](\dot{\boldsymbol{v}}, \eta, \dot{n})
\tag{2.50}
$$

where

$$
\begin{aligned}
&a[\dot{\boldsymbol{\varphi}}, T, \dot{N}](\dot{\boldsymbol{v}}, \eta, \dot{n}; \dot{\boldsymbol{u}}, \theta, \dot{m}) = \\
&\left\{ \begin{array}{l}
\int_B \left[\partial_{\boldsymbol{F}\boldsymbol{F}} E \cdot (\mathrm{Grad}\dot{\boldsymbol{v}} \otimes \mathrm{Grad}\dot{\boldsymbol{u}}) + \partial_{\boldsymbol{F}N} E \cdot (\mathrm{Grad}\dot{\boldsymbol{v}}\, \dot{m}) \right] dV \\[2ex]
\int_B \left[\lambda_1\ \eta\dot{m} + \partial_T \lambda_1\ \dot{N}\ \eta\theta + \partial_{\boldsymbol{G}} \boldsymbol{H} \cdot \left(\mathrm{Grad}(\frac{\eta}{\Theta}) \otimes \mathrm{Grad}(\frac{\theta}{T}) \right) \right] dV \\[2ex]
\int_B \left[\partial_{N\boldsymbol{F}} E \cdot (\dot{n}\mathrm{Grad}\dot{\boldsymbol{u}}) + (-\lambda_2 - T\partial_T \lambda_2)\ \dot{n}\theta + \partial_{NN} E\ \dot{n}\dot{m} \right] dV
\end{array} \right\}
\end{aligned}
\tag{2.51}
$$

is the Dirichlet form. It is clear that the Dirichlet form is symmetric provided that $\lambda_1 = -\lambda_2 - T\partial_T \lambda_2 \equiv \lambda$, and a Fourier potential $\chi(\boldsymbol{G}, T)$ exits such that Fourier's law of heat conduction is of

the form (2.39). In this case (2.49) and (2.51) take the form

$$
\begin{aligned}
&b[\dot{\boldsymbol{\varphi}}, T, \dot{N}](\dot{\boldsymbol{v}}, \eta, \dot{n}) = \\
&\left\{ \begin{array}{l}
-\int_B \partial_{\boldsymbol{F}} E \cdot \mathrm{Grad}\dot{\boldsymbol{v}}\, dV + \int_B R\boldsymbol{B} \cdot \dot{\boldsymbol{v}}\, dV + \int_{\partial_D B} \bar{\boldsymbol{T}} \cdot \dot{\boldsymbol{v}}\, dS \\[2ex]
-\int_B \left(\lambda \dot{N}\ \eta - \frac{RS}{\Theta}\ \eta + \partial_{\boldsymbol{G}} \chi \cdot \mathrm{Grad}\frac{\eta}{\Theta} \right) dV - \int_{\partial_T B} \bar{H}\ \frac{\eta}{\Theta}\, dS \\[2ex]
-\int_B \left(\partial_N E\ \dot{n} - \lambda T\ \dot{n} \right)\, dV
\end{array} \right\} = 0
\end{aligned}
\tag{2.52}
$$

and

$$
\begin{aligned}
&a[\dot{\boldsymbol{\varphi}}, T, \dot{N}](\dot{\boldsymbol{v}}, \eta, \dot{n}; \dot{\boldsymbol{u}}, \theta, \dot{m}) = \\
&\left\{ \begin{array}{l}
\int_B \left[\partial_{\boldsymbol{FF}} E \cdot (\mathrm{Grad}\dot{\boldsymbol{v}} \otimes \mathrm{Grad}\dot{\boldsymbol{u}}) + \partial_{\boldsymbol{F}N} E \cdot (\mathrm{Grad}\dot{\boldsymbol{v}}\, \dot{m}) \right] dV \\[2ex]
\int_B \left[\lambda\ \eta\dot{m} + \partial_T \lambda\ \dot{N}\ \eta\theta + \partial_{\boldsymbol{GG}} \chi \cdot \left(\mathrm{Grad}(\frac{\eta}{\Theta}) \otimes \mathrm{Grad}(\frac{\theta}{T}) \right) \right] dV \\[2ex]
\int_B \left[\partial_{N\boldsymbol{F}} E \cdot (\dot{n}\mathrm{Grad}\dot{\boldsymbol{u}}) + \lambda\ \dot{n}\theta + \partial_{NN} E\ \dot{n}\dot{m} \right]\, dV
\end{array} \right\}
\end{aligned}
\tag{2.53}
$$

respectively. According to Vainberg's theorem [19], the symmetry of a shows that there exists a potential $\Phi[\dot{\boldsymbol{\varphi}}, T, \dot{N}]$ such that the residual b is its first variation, i.e.,

$$
b[\dot{\boldsymbol{\varphi}}, T, \dot{N}](\dot{\boldsymbol{v}}, \eta, \dot{n}) = -D\Phi[\dot{\boldsymbol{\varphi}}, T, \dot{N}](\dot{\boldsymbol{v}}, \eta, \dot{n})\ , \tag{2.54}
$$

where the potential can be written in rate form as

$$
\begin{aligned}
\Phi[\dot{\boldsymbol{\varphi}}, T, \dot{N}] = &\int_B \left[\dot{E} - \lambda T \dot{N} + \chi(\boldsymbol{G}) \right] dV \\
&- \int_B R\boldsymbol{B} \cdot \dot{\boldsymbol{\varphi}}\, dV - \int_B RS \log \frac{T}{T_0}\, dV \\
&- \int_{\partial_D B} \bar{\boldsymbol{T}} \cdot \dot{\boldsymbol{\varphi}}\, dS + \int_{\partial_T B} \bar{H} \log \frac{T}{T_0}\, dS\ .
\end{aligned}
\tag{2.55}
$$

Then, the variational principle is

$$
\boxed{\inf_{\dot{\boldsymbol{\varphi}}, T, \dot{N}} \quad \Phi(\dot{\boldsymbol{\varphi}}, T, \dot{N})}\ , \tag{2.56}
$$

which yields the thermomechanical equations of previous section. Indeed, variations with respect to the different admissible fields give

$$\langle D_{\dot{\varphi}}\Phi, \delta\dot{\boldsymbol{\varphi}}\rangle = \int_B \partial_{\boldsymbol{F}} E(\boldsymbol{F}, N)\cdot \mathrm{Grad}\delta\dot{\boldsymbol{\varphi}}\, dV - \int_B R\boldsymbol{B}\cdot\delta\dot{\boldsymbol{\varphi}}\, dV - \int_{\partial_D B}\bar{\boldsymbol{T}}\cdot\delta\dot{\boldsymbol{\varphi}}\, dS = 0\ , \tag{2.57a}$$

$$\begin{aligned}\langle D_T\Phi, \delta T\rangle = &\int_B (-\lambda - \partial_T\lambda\ T)\dot{N}\ \delta T\, dV \\ &- \int_B \partial_{\boldsymbol{G}}\chi(\boldsymbol{G})\cdot\mathrm{Grad}\frac{\delta T}{T}\, dV - \int_B RS\frac{\delta T}{T}\, dV + \int_{\partial_T B}\bar{H}\frac{\delta T}{T}\, dS = 0\ ,\end{aligned} \tag{2.57b}$$

$$\langle D_{\dot{N}}\Phi, \delta\dot{N}\rangle = \int_B (\partial_N E(\boldsymbol{F}, N) - \lambda T)\,\delta\dot{N}\, dV = \int_B (\Theta - \lambda T)\,\delta\dot{N}\, dV = 0\ . \tag{2.57c}$$

Stationarity condition (2.57c) states that, in equilibrium configurations, the thermodynamic temperature and the external temperature field should coincide, i.e., $\Theta = T$ and $\lambda = 1$. Integrating by parts in equation (2.57a) yields

$$-\int_B (\mathrm{Div}\boldsymbol{P} + R\boldsymbol{B})\cdot\delta\dot{\boldsymbol{\varphi}}\, dV + \int_{\partial_T B}(\boldsymbol{P}\cdot\boldsymbol{N} - \bar{\boldsymbol{T}})\cdot\delta\dot{\boldsymbol{\varphi}}\, dS = 0\ , \tag{2.58}$$

which provides the quasistatic balance equation. A similar manipulation of equation (2.57b) yields

$$\int_B \left((-\lambda - T\partial_T\lambda)\dot{N} + \frac{\mathrm{Div}\boldsymbol{H}}{T} - \frac{RS}{T}\right)\delta T\, dV - \int_{\partial_T B}(\boldsymbol{H}\cdot\boldsymbol{N} - \bar{H})\frac{\delta T}{T}\, dS = 0\ , \tag{2.59}$$

which gives the energy conservation provided that $(-\lambda - T\partial_T\lambda) = 1$ at equilibrium.

Now we turn to the selection of $\lambda_1(\Theta, T)$ and $\lambda_2(\Theta, T)$ such that

$$\lambda \equiv \lambda_1 = -\lambda_2 - T\partial_T\lambda_2\ , \tag{2.60}$$

and, at equilibrium,

$$(-\lambda - T\partial_T\lambda)|_{\Theta=T} = \lambda|_{\Theta=T} = \lambda_1|_{\Theta=T} = (-\lambda_2 - T\partial_T\lambda_2)|_{\Theta=T} = 1\ . \tag{2.61}$$

A simple calculation shows that the only selection of λ which satisfies above conditions is

$$\lambda\ (= \lambda_1 = \lambda_2) = \frac{\Theta^2}{T^2} \tag{2.62}$$

whereupon (2.55) becomes

$$\begin{aligned}\Phi[\dot{\boldsymbol{\varphi}}, T, \dot{N}] = &\int_B \left[\dot{E} - \frac{\Theta^2}{T}\dot{N} + \chi(\boldsymbol{G})\right] dV \\ &- \int_B R\boldsymbol{B}\cdot\dot{\boldsymbol{\varphi}}\, dV - \int_B RS\log\frac{T}{T_0}\, dV \\ &- \int_{\partial_D B} \bar{\boldsymbol{T}}\cdot\dot{\boldsymbol{\varphi}}\, dS + \int_{\partial_T B} \bar{H}\log\frac{T}{T_0}\, dS\ ,\end{aligned} \tag{2.63}$$

which gives the potential energy function for thermoelastic materials.

2.3.2 Extension to viscoplastic materials

Extension of the thermoelastic potential to the general thermoelastic-viscoplastic materials follows the same line for thermoelastic materials. Particularly, we seek the potential function for the materials with uncoupled rate sensitivity, viscosity and heat conduction.

Motivated by (2.63), we assume the energy potential takes the form of

$$\begin{aligned}\Phi[\dot{\boldsymbol{\varphi}}, T, \dot{N}, \dot{\boldsymbol{Z}}] = &\int_B \left[\dot{E} - \frac{\Theta^2}{T}\dot{N} + \Delta(\dot{\boldsymbol{F}}, \dot{\boldsymbol{Z}}, \boldsymbol{F}, \boldsymbol{Z}, T, \Theta)\right] dV \\ &- \int_B R\boldsymbol{B}\cdot\dot{\boldsymbol{\varphi}}\, dV - \int_B RS\log\frac{T}{T_0}\, dV \\ &- \int_{\partial_D B} \bar{\boldsymbol{T}}\cdot\dot{\boldsymbol{\varphi}}\, dS + \int_{\partial_T B} \bar{H}\log\frac{T}{T_0}\, dS\ ,\end{aligned} \tag{2.64}$$

where $\Delta(\dot{\boldsymbol{F}}, \dot{\boldsymbol{Z}}, \boldsymbol{F}, \boldsymbol{Z}, T, \Theta)$ is a general kinetic potential. In the case of uncoupled rate sensitivity, viscosity and heat conduction, Δ is of form (2.40), i.e.,

$$\Delta = \psi^*(\frac{\Theta}{T}\dot{\boldsymbol{Z}}, \boldsymbol{Z}, \Theta) + \phi^*(\frac{\Theta}{T}\dot{\boldsymbol{F}}, \boldsymbol{F}, \Theta) + \chi(\boldsymbol{G}(T), \Theta)\ , \tag{2.65}$$

where a factor $\frac{\Theta}{T}$ is introduced for the purpose of variational formulation. Obviously, at equilibrium, (2.65) takes the same form as (2.40). For thermoelastic material, $\Delta = \chi(\boldsymbol{G}(T), \Theta)$, and the potential reduces to the previous thermoelastic version.

Then, the solution to the thermomechanical boundary value problem in rate form now derives

from a variational minimization principle

$$\boxed{\inf_{\dot{\boldsymbol{\varphi}},T,\dot{N},\dot{\boldsymbol{Z}}} \quad \Phi(\dot{\boldsymbol{\varphi}},T,\dot{N},\dot{\boldsymbol{Z}})} \ . \tag{2.66}$$

Explicitly, we have

$$\begin{aligned}\langle D_{\dot{\varphi}}\Phi,\delta\dot{\boldsymbol{\varphi}}\rangle &= \int_B \left[\boldsymbol{P}^e + \partial_{\dot{\boldsymbol{F}}}\phi^*(\frac{\Theta}{T}\dot{\boldsymbol{F}},\boldsymbol{F},\Theta)\right]\cdot \mathrm{Grad}\delta\dot{\boldsymbol{\varphi}}\,dV \\ &\quad - \int_B R\boldsymbol{B}\cdot\delta\dot{\boldsymbol{\varphi}}\,dV - \int_{\partial_D B}\bar{\boldsymbol{T}}\cdot\delta\dot{\boldsymbol{\varphi}}\,dS = 0\ ,\end{aligned} \tag{2.67a}$$

$$\begin{aligned}\langle D_T\Phi,\delta T\rangle &= \int_B \frac{\Theta^2}{T^2}\dot{N}\delta T\,dV - \frac{\Theta}{T^2}(\boldsymbol{Y}\cdot\dot{\boldsymbol{Z}} + \boldsymbol{P}^v\cdot\dot{\boldsymbol{F}}) \\ &\quad - \int_B \partial_{\boldsymbol{G}}\chi(\boldsymbol{G},\Theta)\cdot\mathrm{Grad}\frac{\delta T}{T}\,dV - \int_B RS\frac{\delta T}{T}\,dV + \int_{\partial_T B}\bar{H}\frac{\delta T}{T}\,dS = 0\ ,\end{aligned} \tag{2.67b}$$

$$\langle D_{\dot{N}}\Phi,\delta\dot{N}\rangle = \int_B \left(\partial_N E(\boldsymbol{F},N) - \frac{\Theta^2}{T}\right)\delta\dot{N}\,dV = \int_B \frac{\Theta}{T}\,(T-\Theta)\,\delta\dot{N}\,dV = 0\ , \tag{2.67c}$$

$$\langle D_{\dot{\boldsymbol{Z}}}\Phi,\delta\dot{\boldsymbol{Z}}\rangle = \int_B \left[-\boldsymbol{Y} + \partial_{\dot{\boldsymbol{Z}}}\psi^*(\frac{\Theta}{T}\dot{\boldsymbol{Z}},\boldsymbol{Z},\Theta)\right]\cdot\delta\dot{\boldsymbol{Z}}\,dV = 0\ . \tag{2.67d}$$

As stationarity condition (2.67c) prevails, above conditions give the desired Euler equations. Specially, the kinetic relations (2.31) and(2.36) are recovered, i.e.,

$$\boldsymbol{Y} - \partial_{\dot{\boldsymbol{Z}}}\psi^* = \boldsymbol{0}\ , \tag{2.68a}$$

$$\boldsymbol{P}^v - \partial_{\dot{\boldsymbol{F}}}\phi^* = \boldsymbol{0}\ . \tag{2.68b}$$

The quasi-static balance equation is as same as previous thermoelastic version, and heat equation is given by

$$T\dot{N} - \boldsymbol{Y}\cdot\dot{\boldsymbol{Z}} - \boldsymbol{P}^v\cdot\dot{\boldsymbol{F}} - RS + \mathrm{Div}\boldsymbol{H} = 0\ . \tag{2.69}$$

2.4 Variational thermomechanical updates

In this section, we concern the time-discretized version of the variational form outlined in previous section. Let us consider an incremental procedure, and more particularly a generic time interval $[t_n, t_{n+1}]$. Let the fields describing the state of the body at time t_n ($\boldsymbol{\varphi}_n$, T_n N_n, $\boldsymbol{Z}_n$) be known. We then seek to characterize the updated fields, at time t_{n+1}, as *minimizers* of a suitably chosen

function, inspired from (2.64). To this end, we define the incremental energy function

$$
\begin{aligned}
&\Phi_n(\boldsymbol{\varphi}_{n+1}, T_{n+1}, N_{n+1}, \boldsymbol{Z}_{n+1}; \boldsymbol{\varphi}_n, T_n, N_n, \boldsymbol{Z}_n) = \\
&\quad \int_B \left\{ [E(\boldsymbol{F}_{n+1}, N_{n+1}, \boldsymbol{Z}_{n+1}) - E_n] - \frac{T_n^2}{T_{n+1}} (N_{n+1} - N_n) \right\} dV \\
&\quad + \int_B \triangle t \Big[\psi^*(\frac{T_n}{T_{n+1}} \frac{\boldsymbol{Z}_{n+1} - \boldsymbol{Z}_n}{\triangle t}, \boldsymbol{Z}_{n+\alpha}, T_{n+\alpha}) + \phi^*(\frac{T_n}{T_{n+1}} \frac{\boldsymbol{F}_{n+1} - \boldsymbol{F}_n}{\triangle t}, \boldsymbol{F}_{n+\alpha}, T_{n+\alpha}) \\
&\qquad\qquad + \chi(\boldsymbol{G}_{n+1}, T_{n+\alpha}) \Big] dV \\
&\quad - \int_B R\boldsymbol{B}(t_{n+1}) \cdot (\boldsymbol{\varphi}_{n+1} - \boldsymbol{\varphi}_n)\, dV - \int_{\partial_D B} \bar{\boldsymbol{T}}(t_{n+1}) \cdot (\boldsymbol{\varphi}_{n+1} - \boldsymbol{\varphi}_n)\, dS \\
&\quad - \int_B \triangle t RS(t_{n+1}) \log \frac{T_{n+1}}{T_n}\, dV + \int_{\partial_T B} \triangle t \bar{H}(t_{n+1}) \log \frac{T_{n+1}}{T_n}\, dS \ ,
\end{aligned}
\tag{2.70}
$$

where we write

$$
\boldsymbol{F}_{n+\alpha} = (1-\alpha)\boldsymbol{F}_n + \alpha \boldsymbol{F}_{n+1} \ , \tag{2.71a}
$$

$$
T_{n+\alpha} = (1-\alpha)T_n + \alpha T_{n+1} \ , \tag{2.71b}
$$

$$
\boldsymbol{Z}_{n+\alpha} = (1-\alpha)\boldsymbol{Z}_n + \alpha \boldsymbol{Z}_{n+1} \ , \tag{2.71c}
$$

in terms of an algorithmic parameter $\alpha \in [0, 1]$.

The updated fields are then solutions to the following variational principle

$$
\boxed{\inf_{\boldsymbol{\varphi}_{n+1}, T_{n+1}, N_{n+1}, \boldsymbol{Z}_{n+1}} \Phi_n(\boldsymbol{\varphi}_{n+1}, T_{n+1}, N_{n+1}, \boldsymbol{Z}_{n+1}; \boldsymbol{\varphi}_n, T_n, N_n, \boldsymbol{Z}_n)} \ . \tag{2.72}
$$

Indeed, the Euler-Lagrange equations of the above minimization problem are given by

$$
\begin{aligned}
&-\int_B \mathrm{Div}\left(\boldsymbol{P}^e+\frac{T_n}{T}\boldsymbol{P}^v\right)\,dV+\int_{\partial_D B}\left(\boldsymbol{P}^e+\frac{T_n}{T}\boldsymbol{P}^v\right)\cdot\boldsymbol{N}\,dS\\
&\qquad\qquad -\int_B R\boldsymbol{B}\,dV-\int_{\partial_D B}\bar{\boldsymbol{T}}\,dS=0\ ,
\end{aligned}
\tag{2.73a}
$$

$$
\begin{aligned}
&\int_B\frac{T_n}{T^2}\left[T_n(N-N_n)-\boldsymbol{Y}\cdot\dot{\boldsymbol{Z}}-\boldsymbol{P}^v\cdot\dot{\boldsymbol{F}}\right]\,dV\\
&\qquad\qquad +\int_B\frac{1}{T}\triangle t\ \mathrm{Div}\partial_{\boldsymbol{G}}\chi(\boldsymbol{G},T_n)\,dV-\int_{\partial_T B}\frac{1}{T}\triangle t\ \partial_{\boldsymbol{G}}\chi(\boldsymbol{G},T_n)\cdot\boldsymbol{N}\,dS\\
&\qquad\qquad -\int_B\frac{1}{T}\triangle t\ RS\,dV+\int_{\partial_T B}\frac{1}{T}\triangle t\ \bar{H}\,dS=0\ ,
\end{aligned}
\tag{2.73b}
$$

$$
\int_B\left[\partial_N E(\boldsymbol{F},N,\boldsymbol{Z})-\frac{T_n^2}{T}\right]\,dV=0\ ,
\tag{2.73c}
$$

$$
\int_B\left[\partial_{\boldsymbol{Z}}E(\boldsymbol{F},N,\boldsymbol{Z})+\frac{T_n}{T}\boldsymbol{Y}\right]\,dV=0\ ,
\tag{2.73d}
$$

where we dropped subscripts $n+1$ and took $\alpha=0$ to preserve conciseness in writing. Clearly, the extension to cases where $0<\alpha\leq 1$ is straightforward. In these equations, $\boldsymbol{Y}$ stands for

$$
\boldsymbol{Y}=\partial_{\dot{\boldsymbol{Z}}}\psi^*\left(\frac{T_n}{T}\frac{\boldsymbol{Z}-\boldsymbol{Z}_n}{\triangle t},\boldsymbol{Z}_n,T_n\right)\ ,
\tag{2.74}
$$

while $\boldsymbol{P}^v$ stands for

$$
\boldsymbol{P}^v=\partial_{\dot{\boldsymbol{F}}}\phi^*\left(\frac{T_n}{T}\frac{\boldsymbol{F}-\boldsymbol{F}_n}{\triangle t},\boldsymbol{F}_n,T_n\right)\ ,
\tag{2.75}
$$

Equation (2.73c) gives the updated temperature as a function of the other state variables and corresponds exactly to (2.67c), written at time t_{n+1}. Equation (2.73d) is the incremental counterpart to (2.67d). Note that the factor $T/T_n\to 1$ as $\triangle t\to 0$, demonstrating the consistency of the incremental equation (2.73d) with respect to its continuous equivalent.

Equation (2.73a) yields the quasi-static balance equation

$$
\mathrm{Div}\boldsymbol{P}+R\boldsymbol{B}=0\quad\text{and}\quad\boldsymbol{P}\cdot\boldsymbol{N}=\bar{\boldsymbol{T}}\,\text{on}\,\partial_D B\ ,
\tag{2.76}
$$

where the effective incremental stress $\boldsymbol{P}$ is defined by

$$
\boldsymbol{P}=\boldsymbol{P}^e+\frac{T_n}{T}\boldsymbol{P}^v\ .
\tag{2.77}
$$

Once more, as the time step $\triangle t \to 0$, $T \to T_n$ and we retrieve the continuous definition of the stress tensor (2.10). Equation (2.73b) yields an incremental heat equation:

$$T_n(N - N_n) = \boldsymbol{Y} \cdot (\boldsymbol{Z} - \boldsymbol{Z}_n) + \boldsymbol{P}^v \cdot (\boldsymbol{F} - \boldsymbol{F}_n) - \frac{T}{T_n} (\triangle t \, \mathrm{Div}\boldsymbol{H} + \triangle t \, RS) \ . \tag{2.78}$$

This equation tends to the continuous heat equation (2.69) when taking the limit $\triangle t \to 0$, which completes the demonstration of the consistency of the proposed variational incremental formulation with the continuous thermomechanical equations.

Remark 2.4.1. Note that, even in the case of a finite time increment, the factor T_n/T which appears in the above incremental equations is always close to unity for typical step sizes. Consider for example an increment of 5 degrees around room temperature ($293K$), which is quite large compared to typical numerical simulations of thermomechanical processes. Then we have $T_n/T = 0.983$, or a deviation of less than 2% from unity. □

The unknown state variables can formally be separated between actual field variables and local variables. Indeed, incremental energy function (2.70) does not involve any spatial gradient of either entropy N or internal variables $\boldsymbol{Z}$, contrarily to the deformation mapping $\boldsymbol{\varphi}$ and temperature T. This suggests rewriting the variational principle (2.72) in terms of a local variational constitutive update and a field pseudo-thermoelastic variational principle. To this end, we define the incremental pseudo-thermoelastic energy density

$$\begin{aligned} W_n(\boldsymbol{F}_{n+1}, T_{n+1}; \boldsymbol{F}_n, T_n, N_n, \boldsymbol{Z}_n) = \triangle t \, \phi^*(\frac{T_n}{T_{n+1}} \frac{\boldsymbol{\Delta F}}{\triangle t}, \boldsymbol{F}_{n+\alpha}, T_{n+\alpha}) \\ + \inf_{N_{n+1}, \boldsymbol{Z}_{n+1}} \Big\{ [E(\boldsymbol{F}_{n+1}, N_{n+1}, \boldsymbol{Z}_{n+1}) - E_n] - \frac{T_n^2}{T_{n+1}} (N_{n+1} - N_n) \\ + \triangle t \, \psi^*(\frac{T_n}{T_{n+1}} \frac{\boldsymbol{\Delta Z}}{\triangle t}, \boldsymbol{Z}_{n+\alpha}, T_{n+\alpha}) \Big\} \ . \end{aligned} \tag{2.79}$$

Effecting the minimization with respect to N_{n+1} and $\boldsymbol{Z}_{n+1}$ in (2.79) respectively yields relations (2.73c) and (2.73d) in local form. Note that in the isothermal case ($T_{n+1} = T_n = T_0$), (2.79) reduces

to the following form, by introducing Helmholtz free energy by way of (2.13),

$$W_n(\boldsymbol{F}_{n+1}, T_{n+1}; \boldsymbol{F}_n, \boldsymbol{Z}_n) = \triangle t\, \phi^*(\frac{\Delta \boldsymbol{F}}{\triangle t}, \boldsymbol{F}_{n+\alpha}) \\ + \inf_{\boldsymbol{Z}_{n+1}} \left[A(\boldsymbol{F}_{n+1}, T_{n+1}, \boldsymbol{Z}_{n+1}) - A_n + \triangle t\, \psi^*(\frac{\Delta \boldsymbol{Z}}{\triangle t}, \boldsymbol{Z}_{n+\alpha}) \right] , \quad (2.80)$$

which is exactly the incremental energy density introduced in [12]. This shows that the preceding formulation generalizes the isothermal approach under a variational thermodynamic framework. The incremental energy density (2.79) now acts as a potential for the gradient of deformation $\boldsymbol{F}$ and the temperature T, with

$$\frac{\partial W_n}{\partial \boldsymbol{F}}(\boldsymbol{F}_{n+1}, T_{n+1}) = \boldsymbol{P} , \quad (2.81a)$$

$$\frac{\partial W_n}{\partial T}(\boldsymbol{F}_{n+1}, T_{n+1}) = \frac{T_n^2}{T_{n+1}^2}(N_{n+1} - N_n - \frac{1}{T_n}\boldsymbol{P}^v \cdot \Delta \boldsymbol{F} - \frac{1}{T_n}\boldsymbol{Y} \cdot \Delta \boldsymbol{Z}) , \quad (2.81b)$$

where $\boldsymbol{P}$, $\boldsymbol{P}^v$ and $\boldsymbol{Y}$ are defined by (2.77), (2.75) and (2.74), respectively.

The field variational principle can now be written as

$$\boxed{\inf_{\boldsymbol{\varphi}_{n+1}, T_{n+1}} \Phi_n(\boldsymbol{\varphi}_{n+1}, T_{n+1})} \quad (2.82)$$

with

$$\Phi_n(\boldsymbol{\varphi}_{n+1}, T_{n+1}) = \int_B W_n(\boldsymbol{F}_{n+1}, T_{n+1})\, dV + \int_B \triangle t \chi(\boldsymbol{G}_{n+1}, T_{n+\alpha})\, dV \\ - \int_B RbB(t_{n+1}) \cdot (\boldsymbol{\varphi}_{n+1} - \boldsymbol{\varphi}_n)\, dV - \int_{\partial_D B} \bar{\boldsymbol{T}}(t_{n+1}) \cdot (\boldsymbol{\varphi}_{n+1} - \boldsymbol{\varphi}_n)\, dS \quad (2.83) \\ - \int_B \triangle t RS(t_{n+1}) \log \frac{T_{n+1}}{T_n}\, dV + \int_{\partial_T B} \triangle t \bar{H}(t_{n+1}) \log \frac{T_{n+1}}{T_n}\, dS .$$

2.5 Heat equation

As shown in previous section, the heat equation which governs the evolution of temperature for thermoelasto-viscoplastic materials can be written in entropy form of

$$T\dot{N} = \boldsymbol{Y} \cdot \dot{\boldsymbol{Z}} + \boldsymbol{P}^v \cdot \dot{\boldsymbol{F}} + RS - \mathrm{Div}\boldsymbol{H} . \quad (2.84)$$

Note that

$$T\dot{N} = -T\partial_T \dot{A} = -T(\partial_T \boldsymbol{P}^e \cdot \dot{\boldsymbol{F}} + \partial^2_{TT} A\ \dot{T} - \partial_T \boldsymbol{Y} \cdot \dot{\boldsymbol{Z}}) \ . \tag{2.85}$$

Introducing the heat capacity per unit undeformed volume at constant deformation as

$$C_v = -T\partial^2_{TT} A \ , \tag{2.86}$$

and rearranging the terms, we obtain

$$C_v \dot{T} = \boldsymbol{Y} \cdot \dot{\boldsymbol{Z}} + \boldsymbol{P}^v \cdot \dot{\boldsymbol{F}} + T\partial_T \boldsymbol{P}^e \cdot \dot{\boldsymbol{F}} - T\partial_T \boldsymbol{Y} \cdot \dot{\boldsymbol{Z}} + RS - \mathrm{Div}\boldsymbol{H} \ . \tag{2.87}$$

We see from this equation that several factors contribute to raising the temperature of the body: the dissipation due to internal process, accounted for by the term $\boldsymbol{Y} \cdot \dot{\boldsymbol{Z}}$; the dissipation of viscous friction $\boldsymbol{P}^v \cdot \dot{\boldsymbol{F}}$; the elastic-pastic structural heating associated to the non-dissipative (latent) elastic and plastic structural changes, e.g., thermal dilatation, accounted for by the term $T\partial_T \boldsymbol{P}^e \cdot \dot{\boldsymbol{F}} - T\partial_T \boldsymbol{Y} \cdot \dot{\boldsymbol{Z}}$; and the external heat sources and heat conduction, accounted for by the term $RS - \mathrm{Div}\boldsymbol{H}$.

Define

$$\beta = 1 - \frac{-T\partial_T \boldsymbol{P}^e \cdot \dot{\boldsymbol{F}} + T\partial_T \boldsymbol{Y} \cdot \dot{\boldsymbol{Z}}}{\boldsymbol{Y} \cdot \dot{\boldsymbol{Z}}} \ , \tag{2.88}$$

whereupon the heat equation becomes

$$C_v \dot{T} = \beta \boldsymbol{Y} \cdot \dot{\boldsymbol{Z}} + \boldsymbol{P}^v \cdot \dot{\boldsymbol{F}} + RS - \mathrm{Div}\boldsymbol{H} \tag{2.89}$$

We see from this definition that β may be interpreted as the fraction of internal dissipation rate which is converted into heat. Therefore, the present definition generalizes the classical definition of Taylor [33] of the fraction of plastic power converted into heat. It bears emphasis that the thermodynamic framework just outlined suggests that β follows directly from the internal energy and kinetic equations, and therefore is not an independent thermodynamic function. In particular, it cannot be modeled independently.

One-dimensional validation of heat equation

The study on heating from plastic power goes back to the pioneering work of Taylor and Quinney, who performed the first experiments investigating this issue in 1937 [33]. It has been generally assumed in the theoretical and numerical analysis that the temperature rise is a partition of plastic power and is taken to be a constant, typically chosen between 0.8 and 1.0 (e.g., [17, 34, 35]). Mason *et al.* [36] made the first attempt to measure the temperature rise via fully dynamic experiments performed over a wide range of strains and strain rates. The results show dramatic variations of this fraction with both strain and strain rate for engineering materials. Hodowany *et al.* [37] improved the resolution of thermal detectors by using a high-speed HgCdTe photoconductive technique and, hence, is said to have higher accuracy to measure the partition of plastic work into heat under adiabatic conditions. Rosakis *et al.* [38] set up a semi-analytical expression for the relationship between temperature rise and plastic power based on an internal variable model.

In this section, we examine the ability of the thermodynamic framework formulated in the foregoing to provide a consistent interpretation the bar experimental data of Hodowany *et al.* [37]. The experimental setup concerns a sample placed between the input and output bars of the Kolsky (split-Hopkinson) pressure bar for dynamic experiments while a servohydraulic load frame was used to measure mechanical properties at lower strain rates. The temperature was measured by high-speed infrared photonconductive detectors. For the purpose of comparison, we present here a one-dimensional constitutive model.

One-dimensional constitutive model

In the case of one-dimensional framework, we assume that the usual additive decomposition of strain holds, i.e.,

$$\epsilon = \epsilon^e + \epsilon^p \ , \tag{2.90}$$

where ϵ^e and ϵ^p are the elastic and plastic part of the strain. We further assume that ϵ^p is the only internal variable, which, in this case, coincides with the plastic strain. The internal energy density is taken in the simple form of

$$E(\epsilon, \eta, \epsilon^p) = \frac{C}{2}[\epsilon^e - \alpha(\theta - \theta_0)]^2 + c_v\theta(\eta) \ , \tag{2.91}$$

where η is the entropy, C is the elastic modulus, c_v is the specific heat at constant volume, α is the thermal expansion coefficient, θ is the absolute temperature, θ_0 is the reference temperature, and it is assumed that the internal energy density depends on ϵ^p only through the elastic strain, i.e., $\epsilon^e = \epsilon - \epsilon^p$. The dependence of θ on η is given by inverting the the total entropy equation

$$\eta = c_v \log \frac{\theta}{\theta_0} + \alpha C[\epsilon^e - \alpha(\theta - \theta_0)] \ . \tag{2.92}$$

This expression leads, after performing a Legendre transformation, to the following explicit result for the free energy density

$$A(\epsilon, \theta, \epsilon^p) = \frac{C}{2}[\epsilon^e - \alpha(\theta - \theta_0)]^2 + c_v\theta\left(1 - \log\frac{\theta}{\theta_0}\right) \ . \tag{2.93}$$

Furthermore, we assume a dual kinetic potential of the form

$$\psi^*(\dot{\epsilon^p}, \theta) = \frac{m}{m+1}\sigma_y(\theta)\dot{\epsilon_0^p}\left(1 + \frac{\dot{\epsilon^p}}{\dot{\epsilon_0^p}}\right)^{\frac{m+1}{m}} + (\sigma_0 - \sigma_y(\theta))\dot{\epsilon^p} \ , \tag{2.94}$$

where $\sigma_y(\theta)$ is the yield stress, $\dot{\epsilon_0^p}$ is a reference plastic strain rate, m is the rate hardening exponent, and σ_0 is the quasi-static flow stress with plastic strain hardening given by

$$\sigma_0 = \sigma_y(\theta)\left(1 + \frac{\epsilon^p}{\epsilon_0^p}\right)^{1/n} \ , \tag{2.95}$$

where ϵ_0^p is a reference plastic strain and n is the hardening exponent. We further assume a linear thermal softening of yield stress in the form of

$$\sigma_y(\theta) = \sigma_y(\theta_0)[1 - \omega(\theta - \theta_0)] \ , \tag{2.96}$$

where ω is the thermal softening coefficient [39] and $\theta_0(= 293\text{K})$ is the reference temperature.

It is followed by the inverse kinetic relations as

$$y = \frac{\partial\psi^*}{\partial\dot{\epsilon^p}} = \sigma_y(\theta)\left(1 + \frac{\dot{\epsilon^p}}{\dot{\epsilon_0^p}}\right)^{\frac{1}{m}} + \sigma_0(\epsilon^p, \theta) - \sigma_y(\theta) \ . \tag{2.97}$$

A direct specialization of the Euler-Lagrange equations (2.68a) and (2.69) for one dimensional case gives

$$-\sigma + y = 0 \ , \tag{2.98}$$

$$\theta\dot{\eta} = \sigma\dot{\epsilon^p} + \rho s - \nabla \cdot \boldsymbol{h} \ , \tag{2.99}$$

where

$$\sigma = C[\epsilon^e - \alpha(\theta - \theta_0)] \tag{2.100}$$

is the effective stress, ρ is the mass density, s is the external heat source and $\boldsymbol{h}$ is the heat flux. (2.98) can be solved for ϵ^p numerically, e.g., by a Newton-Raphson iteration. And (2.99) governs the evolution of temperature. If, further, the adiabatic heating prevails, (2.99) becomes

$$\theta\dot{\eta} = \sigma\dot{\epsilon^p} \ . \tag{2.101}$$

We note from this equation that all the plastic work is converted into the incremental entropy. Following (2.87), we have

$$c_v\dot{\theta} = \sigma\dot{\epsilon^p} - \alpha\theta C\dot{\epsilon} - \theta\frac{\partial y}{\partial\theta}\dot{\epsilon^p} \ , \tag{2.102}$$

or,

$$c_v\dot{\theta} = \beta\sigma\dot{\epsilon^p} \ , \tag{2.103}$$

where

$$\beta = 1 - \frac{\alpha\theta C\dot{\epsilon} + \theta\frac{\partial y}{\partial\theta}\dot{\epsilon^p}}{\sigma\dot{\epsilon^p}} \tag{2.104}$$

is the fraction of plastic power converted into heat.

Numerical results

We now apply this model to two materials: rate-dependent α-titanium and rate-independent Al2024-T3. The material parameters used in the calculations are tabulated in Table 2.1.

The resulting temperature evolution is calculated by solving (2.98) and (2.102) numerically. In the calculation, strain rates $\dot{\epsilon} = 1\ \mathrm{s}^{-1}$ and $\dot{\epsilon} = 3000\ \mathrm{s}^{-1}$ are adopted. The stress-strain curves for

Material	C	$\sigma_y(\theta_0)$	c_v $(\times 10^6)$	ϵ_0^p	$\dot{\epsilon}_0^p$	n	m	ω	$\alpha(\times 10^{-6})$
α-titanium	116 GPa	400 MPa	2.33Jm^{-3}	0.1	0.1	1.45	35	0.0019K^{-1}	1.1K^{-1}
Al2024-T3	69 GPa	380 MPa	2.43Jm^{-3}	0.0015	0.5	5.8	10000	0.0007K^{-1}	2.0K^{-1}

Table 2.1: Material constants for α-titanium [40] and Al2024-T3.

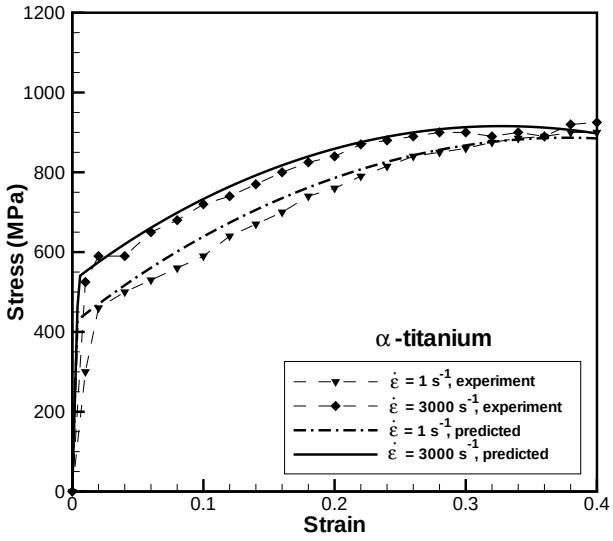

Figure 2.1: Stress-strain curves of α-titanium at strain rate of 1 s^{-1} and 3000 s^{-1}. Experimental data are taken from [37].

α-titanium at strain rates of 1 s^{-1} and 3000 s^{-1} are plotted in Fig. 2.1. It shows that the flow stress of α-titanium is clearly dependent on the strain rate during loading. Materials properties such as strain hardening exponent and strain rate hardening exponent must be exercised to match this dependence. As a result, Fig. 2.2 shows the theoretical prediction of temperature rise versus plastic strain and its comparison with experimental date of Hodowany *et al.* [37] for strain rates of 1 s^{-1} and 3000 s^{-1}. The temperature evolution including its strain rate dependence is well captured by heat equation (2.102).

Another comparison is conducted for Al2024-T3. The predicted stress strain curves and temperature rise at strain rate of 1 s^{-1} and 3000 s^{-1} are plotted in Fig. 2.3 and Fig. 2.4 respectively. In contrast to α-titanium, the predicted temperature rises are essentially rate-insensitive as observed by the experiments [37]. This is achieved by setting the rate hardening exponent in (2.97) a relative

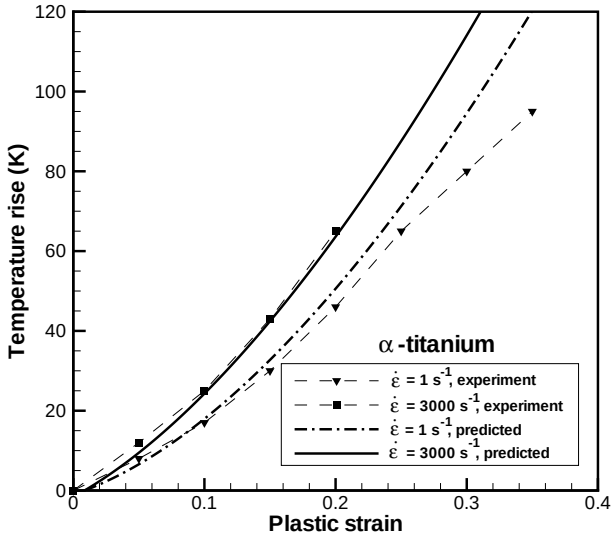

Figure 2.2: Adiabatic temperature rise as a function of plastic strain for α-titanium at strain rate of 1 s^{-1} and 3000 s^{-1}. Experimental data are taken from [37].

large number, e.g., $m = 10000$.

Remark 2.5.1. The fraction of plastic power converted into heating can also be calculated based on selected material parameters. While the model indicates that the fraction is a function of strain (and also a function of strain rate for general strain-rate dependent materials), the calculated fraction is different from those obtained in [37]. This difference is understood to be due to the strong sensitivity of β on data fitting. Small perturbations of strain-stress and strain-temperature curves will affect the calculation a lot and it seems impossible to capture these small perturbations by any simple hardening and softening functions. In addition, the difference may also come from the possible different definitions of β fraction used in current model and [37]. Thus, one should be careful when trying to obtain temperature rise as a partition of plastic power. Indeed, it is strongly suggested to update temperature more precisely and directly from the heat equation (2.87) as illustrated in this section.

□

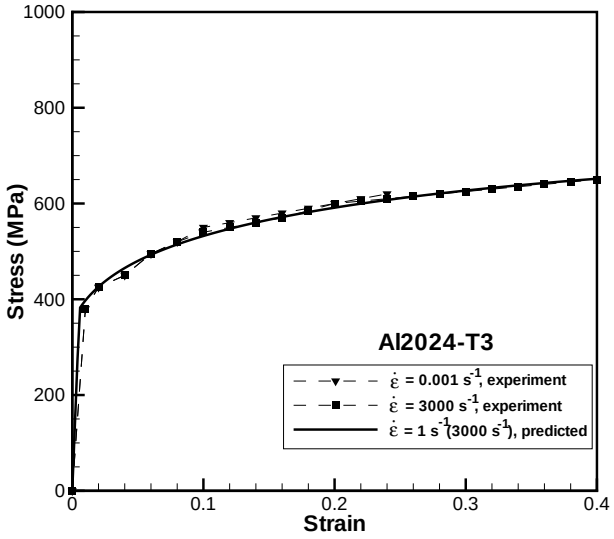

Figure 2.3: Stress-strain curves of Al2024-T3 at strain rate 1 s^{-1} and 3000 s^{-1}. Experimental data are taken from [37].

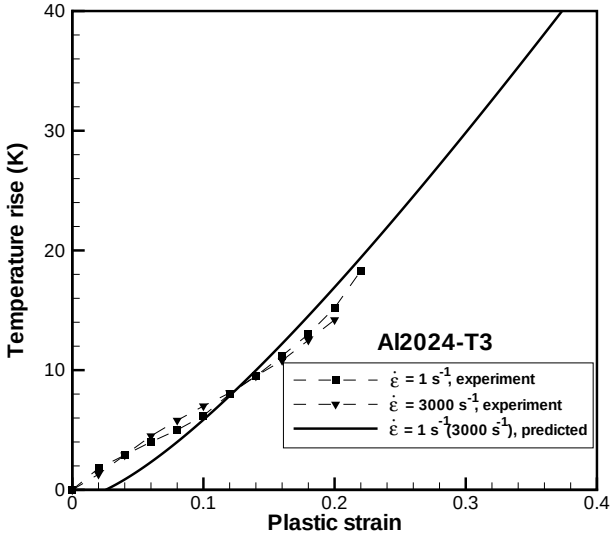

Figure 2.4: Adiabatic temperature rise as a function of plastic strain for Al2024-T3 at strain rate of 1 s^{-1} and 3000 s^{-1}. Experimental data are taken from [37].

2.6 Energy-momentum tensor and configurational forces

This section is concerned with energy-momentum tensor and configurational forces, which are generalized to the coupled thermomechanical boundary value problems by the existence of a energy potential presented in previous sections.

Let us consider a heterogenous body characterized by an incremental pseudo-thermoelastic potential energy of the form

$$\Phi_n(\boldsymbol{\varphi}, T) = \int_B W_n^*(\boldsymbol{X}, \boldsymbol{\varphi}(\boldsymbol{X}), \mathrm{Grad}\boldsymbol{\varphi}(\boldsymbol{X}), T(\boldsymbol{X}), \mathrm{Grad}T(\boldsymbol{X}))\, dV + \text{forcing terms} \,, \tag{2.105}$$

where we write $W_n^* = W_n + \triangle t\chi$ for simplicity in (2.83). The heterogeneity of the system is represented by the explicit dependence of W_n^* on $\boldsymbol{X}$. We note that the first variation of $\Phi_n(\boldsymbol{\varphi}, T)$ as defined in (2.105) is

$$D\Phi_n(\boldsymbol{\varphi}, T)(\boldsymbol{v}, \eta) = \left\{ \begin{array}{l} \int_B \partial_{\boldsymbol{F}} E \cdot \mathrm{Grad}\boldsymbol{v}\, dV - \int_B R\boldsymbol{B} \cdot \boldsymbol{v}\, dV - \int_{\partial_D B} \bar{\boldsymbol{T}} \cdot \boldsymbol{v}\, dS \\ \\ \int_B \left[\frac{T_n^2}{T^2}(N - N_n - \frac{\boldsymbol{Y}\cdot\triangle\boldsymbol{Z}}{T_n} - \frac{\boldsymbol{P}^v\cdot\triangle\boldsymbol{F}}{T_n})\, \eta - \triangle t \frac{RS}{T}\, \eta - \triangle t \partial_{\boldsymbol{G}}\chi \cdot \mathrm{Grad}\frac{\eta}{T} \right] dV - \triangle t \int_{\partial_T B} \bar{H}\, \frac{\eta}{T}\, dS \end{array} \right\} , \tag{2.106}$$

where, by comparison, we have

$$\begin{aligned} &\frac{\partial W_n^*}{\partial \boldsymbol{\varphi}}(\boldsymbol{X}, \boldsymbol{\varphi}, \boldsymbol{F}, T, \mathrm{Grad}T) = -R\boldsymbol{B} \,, \\ &\frac{\partial W_n^*}{\partial \boldsymbol{F}}(\boldsymbol{X}, \boldsymbol{\varphi}, \boldsymbol{F}, T, \mathrm{Grad}T) = \boldsymbol{P} \,, \\ &\frac{\partial W_n^*}{\partial T}(\boldsymbol{X}, \boldsymbol{\varphi}, \boldsymbol{F}, T, \mathrm{Grad}T) = \frac{T_n^2}{T^2}(N - N_n - \frac{\boldsymbol{Y}\cdot\triangle\boldsymbol{Z}}{T_n} - \frac{\boldsymbol{P}^v\cdot\triangle\boldsymbol{F}}{T_n}) - \triangle t\frac{RS}{T} + \triangle t\boldsymbol{H}\cdot\frac{\mathrm{Grad}T}{T} \,, \\ &\frac{\partial W_n^*}{\partial \mathrm{Grad}T}(\boldsymbol{X}, \boldsymbol{\varphi}, \boldsymbol{F}, T, \mathrm{Grad}T) = -\triangle t\, \frac{1}{T}\boldsymbol{H} \,. \end{aligned} \tag{2.107}$$

Within the framework just outlined, configurational forces arise naturally as energetic forces conjugate to rearrangements of the heterogeneity of the system. The configurational force field $\boldsymbol{J}$

corresponding to the rearrangement is given by

$$\boldsymbol{J} = \left(\frac{\partial W_n^*}{\partial \boldsymbol{X}}\right)_{\text{expl}} , \tag{2.108}$$

where the label "expl" signifies that the partial derivatives are taken with respect to the *explicit* dependence of W_n^* on $\boldsymbol{X}$. Evidently, if the material is homogeneous, the configurational force field vanishes identically, as required.

Energetic methods derive much of their power from the fact that the configurational force field can be expressed in conservation form, i.e., as the divergence of a tensor field known as the energy-momentum tensor field. In order to obtain this conservation form of the configurational forces, we note the identities

$$\begin{aligned}
\left(\frac{\partial W_n^*}{\partial X_I}\right)_{\text{expl}} &= \frac{\partial W_n^*}{\partial X_I} - \frac{\partial W_n^*}{\partial \varphi_i}\varphi_{i,I} - \frac{\partial W_n^*}{\partial F_{iJ}}\varphi_{i,JI} - \frac{\partial W_n^*}{\partial T}T_{,I} - \frac{\partial W_n^*}{\partial T_{,J}}T_{,JI} \\
&= \frac{\partial W_n^*}{\partial X_I} + (RB_i\varphi_{i,I} - P_{iJ}\varphi_{i,JI}) \\
&\qquad - \left[\frac{T_n^2}{T}(N - N_n - \frac{\boldsymbol{Y}\cdot\triangle\boldsymbol{Z}}{T_n} - \frac{\boldsymbol{P}^v\cdot\triangle\boldsymbol{F}}{T_n}) - \triangle t RS + \triangle t\, H_J\frac{T_{,J}}{T}\right]\frac{T_{,I}}{T} + \triangle t\frac{H_J}{T}T_{,JI} \\
&= \frac{\partial W_n^*}{\partial X_I} - [(P_{iJ,J} + RB_i)F_{iI} - (P_{iJ}F_{iI})_{,J}] \\
&\qquad - \left[\frac{T_n^2}{T}(N - N_n - \frac{\boldsymbol{Y}\cdot\triangle\boldsymbol{Z}}{T_n} - \frac{\boldsymbol{P}^v\cdot\triangle\boldsymbol{F}}{T_n}) - \triangle t RS + \triangle t H_{J,J}\right]\frac{T_{,I}}{T} + \triangle t(H_J\frac{T_{,I}}{T})_{,J} \\
&= \frac{\partial W_n^*}{\partial X_I} - (P_{iJ}F_{iI})_{,J} + \triangle t(H_J\frac{T_{,I}}{T})_{,J} \\
&= (W_n\delta_{IJ} - F_{iI}P_{iJ})_{,J} + \triangle t(\chi\delta_{IJ} - G_I H_J)_{,J} ,
\end{aligned} \tag{2.109}$$

where δ_{IJ} is the Kronecker delta, W_n is the incremental pseudo-thermoelastic strain energy defined in (2.79) and $G_I = -T_{,I}/T$ such that $\boldsymbol{H} = \partial_{\boldsymbol{G}}\chi$.

Define

$$\boldsymbol{M}_{\text{mech}} = W_n\boldsymbol{I} - \boldsymbol{F}^T\boldsymbol{P} \tag{2.110}$$

the *mechanical* energy-momentum tensor, and

$$\boldsymbol{M}_{\text{therm}} = \chi\boldsymbol{I} - \boldsymbol{G}\otimes\boldsymbol{H} \tag{2.111}$$

the *thermal* energy-momentum tensor. The total Eshelby energy-momentum tensor is then the sum of two parts, i.e.,

$$\boldsymbol{M}_{\text{total}} = \boldsymbol{M}_{\text{mech}} + \triangle t\, \boldsymbol{M}_{\text{therm}} \ . \tag{2.112}$$

Thus, for the coupled thermomechanical problem, we obtain the identity

$$\boldsymbol{J} = \text{Div}\boldsymbol{M}_{\text{total}} = \text{Div}(\boldsymbol{M}_{\text{mech}} + \triangle t\, \boldsymbol{M}_{\text{therm}}) \ , \tag{2.113}$$

which generalizes the traditional definition of configurational forces and energy-momentum tensor [41]. Evidently, $\boldsymbol{M}_{\text{therm}}$ vanishes for isothermal processes and $\boldsymbol{J}$ reduces to the traditional definition.

Example 2.6.1. *J-integral*

By additivity, the total configurational force acting on a subbody $P \subset B$ is

$$\boldsymbol{J}(P) = \int_P \boldsymbol{J}(\boldsymbol{X})\, dV = \int_P \text{Div}\boldsymbol{M}_{\text{total}}\, dV \ , \tag{2.114}$$

or, by the divergence theorem,

$$\boldsymbol{J}(P) = \int_{\partial P} \boldsymbol{M}_{\text{total}}\boldsymbol{N}\, dS \tag{2.115}$$

which is known as the *J-integral*. If W_n is independent of $\boldsymbol{X}$ within an open subset $U \subset B$, then it follows that $\boldsymbol{J}(E) = 0$ for any subbody $E \subset U$.

A generally used J-integral is the first component of the configurational force, i.e.,

$$J_1 = \int_\Gamma \left(W_n N_1 - T_i F_{i1}\right)\, dS + \triangle t \int_\Gamma \left(\chi N_1 - G_1 H_J N_J\right)\, dS \tag{2.116}$$

which is a generalized expression of Rice [42]. According to Rice, the value of the J-integral vanishes along a closed contour if the energy potential density is uniquely determined and there are no singularities inside the contour. Rice and co-workers proved the path independence of the J-integral around a crack tip or notch root [42], and a shear band tip [43] in their study of over-consolidated clay. In both cases, the thermal effects were not considered. However, it can be shown that the configurational force (*J-integral*) introduced in (2.116) is also path-independent by following similar procedures to Rice [42]. □

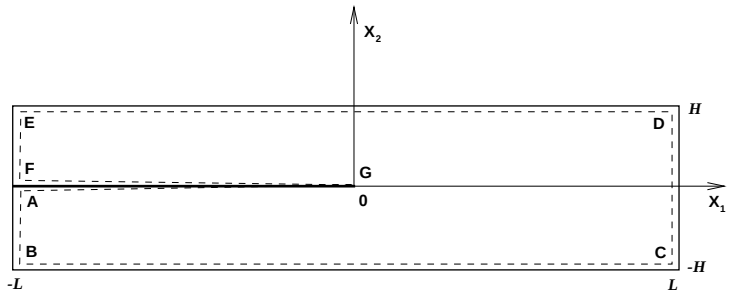

Figure 2.5: Two-dimensional strip with finite length $2L$ and height $2H$.

Example 2.6.2. *Effect of temperature gradient on crack propagation*

As an example, we shall consider the effect of temperature gradient on the propagation of a crack in a two-dimensional strip. As shown in (2.116), existence of a temperature gradient introduces an additional thermal term into the traditional J-integral. For the structure considered in Fig. 2.5, this additional term can be evaluated through a particular contour as

$$\triangle J_T = \triangle t \int_{ABCDEFGA} (\chi N_1 - G_1 H_I N_I)\, dS \ , \tag{2.117}$$

where we assume a Fourier kinetic potential of the form

$$\chi = \frac{1}{2}\frac{kT_0}{T^2}\left[\left(\frac{\partial T}{\partial X_1}\right)^2 + \left(\frac{\partial T}{\partial X_2}\right)^2\right] \ , \qquad G_1 = -\frac{1}{T}\frac{\partial T}{\partial X_1} \ , \qquad H_I = -\frac{kT_0}{T}\frac{\partial T}{\partial X_I} \tag{2.118}$$

and N_I is the normal on I direction.

Particularly, we assume a linear temperature gradient along X_1 direction, i.e.,

$$T(X_1) = a + bX_1 \ , \qquad \text{with} \quad a = \frac{T_R + T_L}{2} \quad \text{and} \quad b = \frac{T_R - T_L}{2L} \tag{2.119}$$

where T_R and T_L are the temperature on $X_1 = L$ and $X_1 = -L$ respectively, and $\partial T/\partial X_1 = b$. Here we have assumed a uniform temperature distribution alone X_2 direction, i.e., $\partial T/\partial X_2 = 0$

everywhere. We further note that $N_1 = 0$ on BC, DE, FG, GA. These simplify the integral into

$$\begin{aligned}\triangle J_T &= \triangle t \int_{AB,CD,EF} (\chi - G_1 H_1)\, dS \\ &= \triangle t \int_{-H}^{H} \frac{-1}{2} \frac{kT_0}{T_R^2} \left(\frac{\partial T}{\partial X_1}\right)^2 dX_2 + \triangle t \int_{H}^{-H} \frac{-1}{2} \frac{kT_0}{T_L^2} \left(\frac{\partial T}{\partial X_1}\right)^2 dX_2 \\ &= \triangle t k T_0 b^2 H \left(\frac{T_R^2 - T_L^2}{T_R^2 T_L^2}\right) .\end{aligned} \tag{2.120}$$

We can see from this equation that

$$\triangle J_T \begin{cases} > 0, & \text{when } T_L < T_R, \text{ i.e., positive temperature gradient along } X_1 , \\ = 0, & \text{when } T_L = T_R, \text{ i.e., uniform temperature distribution along } X_1 , \\ < 0, & \text{when } T_L > T_R, \text{ i.e., negative temperature gradient along } X_1 . \end{cases}$$

Since an increase of the J-integral makes it closer to the fracture criterion J_{IC}, we conclude that a positive temperature gradient accelerates the initialization and propagation of a crack, while a negative temperature gradient reduces the propagation of a crack. This is actually consistent with the experimental observations, e.g., [44]. Unlike the general arguments that the main effect of the temperature gradient on crack initiation is that it makes the materials nonhomogeneous regarding their temperature-dependent mechanical properties, our result, however, validates for any materials including the thermoelastic materials which have weak temperature dependence. □

2.7 Summary and conclusions

In this section, we have developed a variational formulation for general coupled thermomechanical problems in dissipative materials including finite elastic and plastic deformation, non-Newtonian viscosity, rate sensitivity and heat conduction. A potential function is proposed such that both energy conservation and linear momentum balance are Euler-Lagrange equations of its first variation. The time-discretized version of the variational formulation generalizes the isothermal approach under a variational thermodynamic framework. Following the variational formulation, the heat equation for thermoelasto-viscoplastic materials is studied, and the temperature rise thus calculated in a one-dimensional case is compared with experimental data. Finally, we give a general

expression for energy-momentum tensor and configurational forces. It is followed by the introduction of the J-integral and its application to crack propagation by considering a strip with a certain temperature gradient.

Chapter 3

A class of variational strain-localization finite elements

3.1 Introduction

Solids deforming at high rates often develop narrow layers of intense shearing [45, 46, 47, 48, 49, 50, 51]. Outstanding features of these dynamic shear bands are their thinness, with typical widths of 10-100 μm [52]; high local shear strains, which can reach values of up to 100 [50, 51, 53]; ultra-high local shear strain rates, often in excess of 10^6 s^{-1} [50, 51, 53]; local temperature rises of several hundred degrees [54, 55, 56, 57, 58, 36]; and high propagation speeds, sometimes in excess of 1000 m/s [59, 60, 36, 61, 62]. In addition, cracks, whether the result of brittle fracture [49, 63], or of microvoid growth and coalescence [64, 65, 66, 67, 36], often form along shear bands. Shear bands may also occur in over-consolidated soils deforming in shear (e.g., [68, 69, 70, 71]). In these cases, the deformation across the band may include a certain degree of dilatancy in addition to shear. Finally, spallation in metals may be regarded as the result of a process of damage localization leading to the formation of void sheets [72, 73, 74, 75, 76, 77, 78].

The computational modeling of strain localization has been the subject of extensive work. Ortiz *et al.* [79, 70, 71], and subsequently others, devised specialized elements by embedding discontinuous deformation modes into finite elements, with the geometry and orientation of the deformation discontinuities determined from a local bifurcation analysis. While this approach ameliorates the dependence of shear band paths on the mesh orientation, the mesh sizes sets the maximum spatial resolution of the calculation. Another approach consists of resolving the shear band thickness, either with a fixed mesh [62], or by recourse to mesh adaption [80]. However,

the simultaneous resolution of fine shear bands and coarse geometrical features, such as grains and shear-band arrays, may result in exceedingly large meshes, specially in three dimensions. Yet another approach consists of the use of mesh-free Galerkin methods [81, 82, 83]. This approach is well-suited to the computation of arbitrary shear-band paths, but the maximum spatial resolution afforded by the method is still limited by the density of nodes.

In this chapter, we regard strain localization strictly as a *sub-grid* phenomenon and, consequently, the bands of strain localization are modelled as *displacement discontinuities*. These displacement discontinuities are confined to volume-element interfaces and are enabled by the insertion of specialized *strain-localization elements*. These elements consist of two surfaces, attached to the abutting volume elements, which can separate and slip relative to each other. The kinematics of the strain-localization elements is identical to the kinematics of cohesive elements proposed by Ortiz and Pandolfi [21] for the simulation of fracture. In contrast to cohesive elements, the behavior of strain-localization elements is governed directly by the same constitutive relation which governs the deformation of the volume elements. As is evident from dimensional considerations alone, the transformation of displacement jumps into a deformation gradient requires the introduction of a length parameter, namely, the band thickness. In this chapter, the band thickness is optimized on the basis of an incremental variational principle, as presented in Chapter 2. We show that this optimization takes the form of a configurational-force equilibrium and results in a well-defined band thickness. The predictive ability of the approach is demonstrated by means of simulations of Guduru *et al.* [22] dynamic shear-band tests in pre-notched C300 steel specimens.

3.2 General framework

We consider a solid of reference configuration B undergoing a motion defined by a deformation mapping $\boldsymbol{\varphi} : B \times [0,T] \to \mathbb{R}^3$, where $[0,T]$ denotes a time interval. The deformation of the solid includes a thin band of strain localization defined by its midsurface $S \subset B$ and its local thickness h, Fig. 3.1. In addition, let $[\![\boldsymbol{\varphi}]\!]$ be the displacement jump across S and let $\boldsymbol{N}$ be the unit normal to S. Motivated by the multiplicative decomposition of the deformation gradient for the formulation of single-crystal plasticity [84], we represent the deformation gradient $\boldsymbol{F}$ within the band in the

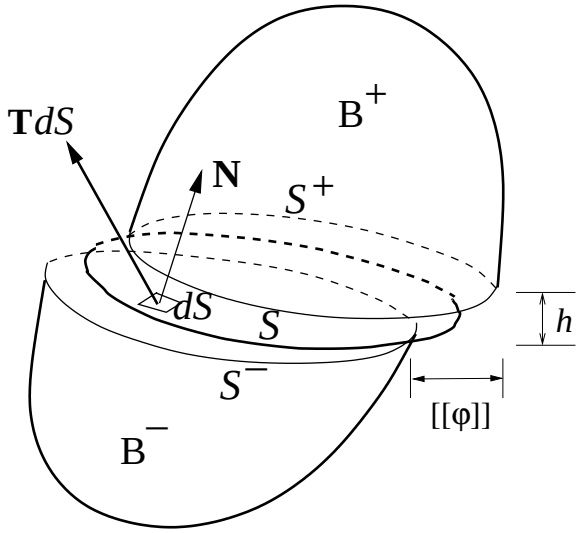

Figure 3.1: Shear band surface traversing a 3-D body. S^+ and S^- are the top and bottom surface of band attached to the subbody B^+ and B^-, respectively. $\boldsymbol{T}$ is the traction acting on the midsurface S.

form

$$\boldsymbol{F} = \boldsymbol{F}^{\parallel}\boldsymbol{F}^{\perp} \ , \tag{3.1}$$

where $\boldsymbol{F}^{\parallel}$ is the in-plane or *membrane deformation* of the band, constrained by the identity

$$\boldsymbol{F}^{\parallel}\boldsymbol{N} = \boldsymbol{N} \tag{3.2}$$

and

$$\boldsymbol{F}^{\perp} = \boldsymbol{I} + \frac{[\![\varphi]\!]}{h} \otimes \boldsymbol{N} \tag{3.3}$$

is the *transverse deformation* of the band. This is essentially consistent with the Hadamard condition for the deformation gradient across a discontinuous surface. The various work-conjugacy

relations of the localized solid are exhibited by the deformation power expression

$$\begin{aligned} P^D &= \sum_{\pm} \int_{B^{\pm}} \boldsymbol{P} \cdot \dot{\boldsymbol{F}}\, dV + \int_S \boldsymbol{P} \cdot \dot{\boldsymbol{F}} h\, dS \\ &= \sum_{\pm} \int_{B^{\pm}} \boldsymbol{P} \cdot \dot{\boldsymbol{F}}\, dV + \int_S \boldsymbol{P} \cdot \left[\dot{\boldsymbol{F}}^{\parallel} \boldsymbol{F}^{\perp} + \boldsymbol{F}^{\parallel} \dot{\boldsymbol{F}}^{\perp} \right] h\, dS \\ &= \sum_{\pm} \int_{B^{\pm}} \boldsymbol{P} \cdot \dot{\boldsymbol{F}}\, dV + \int_S \left[\boldsymbol{P} (\boldsymbol{F}^{\perp})^T \cdot \dot{\boldsymbol{F}}^{\parallel} + (\boldsymbol{F}^{\parallel})^T \boldsymbol{P} \boldsymbol{N} \cdot \frac{[\![\dot{\boldsymbol{\varphi}}]\!]}{h} \right] h\, dS \\ &= \sum_{\pm} \int_{B^{\pm}} \boldsymbol{P} \cdot \dot{\boldsymbol{F}}\, dV + \int_S \left(h \boldsymbol{P}^{\parallel} \cdot \dot{\boldsymbol{F}}^{\parallel} + \boldsymbol{P}^{\perp} \boldsymbol{N} \cdot [\![\dot{\boldsymbol{\varphi}}]\!] \right) dS \\ &= \sum_{\pm} \int_{B^{\pm}} \boldsymbol{P} \cdot \dot{\boldsymbol{F}}\, dV + \int_S \left(h \boldsymbol{P}^{\parallel} \cdot \dot{\boldsymbol{F}}^{\parallel} + \boldsymbol{T} \cdot [\![\dot{\boldsymbol{\varphi}}]\!] \right) dS\ , \end{aligned} \tag{3.4}$$

where

$$\boldsymbol{P}^{\parallel} = \boldsymbol{P} (\boldsymbol{F}^{\perp})^T \tag{3.5}$$

is the *membrate stress tensor component*,

$$\boldsymbol{P}^{\perp} = (\boldsymbol{F}^{\parallel})^T \boldsymbol{P} \tag{3.6}$$

is the *transverse stress tensor* component, and

$$\boldsymbol{T} = \boldsymbol{P}^{\perp} \boldsymbol{N} \tag{3.7}$$

is the traction on S.

Consider now a process of incremental deformation in which the deformation mapping is sampled at discrete times $t = 0,\ \ldots,\ t_n,\ t_{n+1} = t_n + \triangle t,\ \ldots$. Suppose in addition that the incremental plastic behavior of the material in the bulk is characterized by means of a *variational update* (cf [12] and Chapter 2), so that the first Piola-Kirchhoff stress tensor at time t_{n+1} is given by an effective constitutive relation of the form

$$\boldsymbol{P}_{n+1} = \frac{\partial W_n}{\partial \boldsymbol{F}_{n+1}} (\boldsymbol{F}_{n+1})\ , \tag{3.8}$$

where $W_n(\boldsymbol{F}_{n+1})$ is an effective strain-energy density for the time step $[t_n, t_{n+1}]$. One of the principal aims of this paper concerns the application of variational techniques in order to determine an

effective incremental energy density $\phi_n(\boldsymbol{F}^{\shortparallel}_{n+1}, [\![\boldsymbol{\varphi}_{n+1}]\!])$ per unit area of the band, i.e., an effective *shear band energy*, such that

$$\boldsymbol{P}^{\shortparallel}_{n+1} = \frac{1}{h_{n+1}} \frac{\partial \phi_n}{\partial \boldsymbol{F}^{\shortparallel}_{n+1}}(\boldsymbol{F}^{\shortparallel}_{n+1}, [\![\boldsymbol{\varphi}_{n+1}]\!]) \ , \tag{3.9a}$$

$$\boldsymbol{T}_{n+1} = \frac{\partial \phi_n}{\partial [\![\boldsymbol{\varphi}_{n+1}]\!]}(\boldsymbol{F}^{\shortparallel}_{n+1}, [\![\boldsymbol{\varphi}_{n+1}]\!]) \ . \tag{3.9b}$$

The corresponding incremental potential energy is then

$$I_n[\boldsymbol{\varphi}_{n+1}] = \sum_{\pm} \int_{B^{\pm}} W_n(\boldsymbol{F}_{n+1})\, dV + \int_S \phi_n(\boldsymbol{F}^{\shortparallel}_{n+1}, [\![\boldsymbol{\varphi}_{n+1}]\!])\, dS + \text{forcing terms} \tag{3.10}$$

which, upon minimization, yields the updated deformation mapping $[\![\boldsymbol{\varphi}_{n+1}]\!]$.

The determination of the effective incremental shear band energy $\phi_n(\boldsymbol{F}^{\shortparallel}_{n+1}, [\![\boldsymbol{\varphi}_{n+1}]\!])$ entails the optimization of the local internal state of the material within the band (cf [12] and Chapter 2) and the optimization of the shear band thickness as well. As we shall see, the latter optimization may be regarded as a statement of configurational equilibrium consisting of the vanishing of the component of the Eshelby energy-momentum tensor normal to the band. This statement of configurational equilibrium supplies and additional field equation over S which, provided that the stabilizing effect of heat conduction is properly taken into account, determines the optimal local value of the band thickness.

3.3 Adiabatic shear banding

In order to complete the formulation, we need to determine the effective incremental energy density $\phi_n(\boldsymbol{F}^{\shortparallel}_{n+1}, [\![\boldsymbol{\varphi}_{n+1}]\!])$ per unit area which governs the incremental behavior of the band. By way of example, in this section we consider the case of adiabatic shear banding. Assume, for definiteness, a conventional multiplicative decomposition

$$\boldsymbol{F} = \boldsymbol{F}^e \boldsymbol{F}^p \tag{3.11}$$

of the deformation gradient into elastic and plastic parts. Assume in addition, that the solid obeys the J_2-flow theory of plasticity. In a variational setting (cf [12] and Chapter 2), this assumption simply means that $\boldsymbol{F}^p$ is subject to a flow rule of the form

$$\dot{\boldsymbol{F}}^p \boldsymbol{F}^{p-1} = \dot{\epsilon}^p \boldsymbol{M}, \tag{3.12}$$

where ϵ^p is an effective, or Mises, plastic strain, and $\boldsymbol{M}$ is any tensor such that

$$\mathrm{tr}(\boldsymbol{M}) = 0 \ , \tag{3.13a}$$

$$\boldsymbol{M}^T = \boldsymbol{M} \ , \tag{3.13b}$$

$$\boldsymbol{M} \cdot \boldsymbol{M} = \frac{3}{2} \ . \tag{3.13c}$$

We consider a free-energy density per unit undeformed volume of the form

$$A(\boldsymbol{F}^e, T, \epsilon^p) = W^e(\boldsymbol{F}^e, T) + W^p(\epsilon^p, T) + RC_v T \left(1 - \log \frac{T}{T_0}\right) \ , \tag{3.14}$$

where T is the absolute temperature, R is the mass density per unit undeformed volume, C_v is the heat capacity per unit mass at constant volume, and T_0 is a reference temperature. Coleman's equilibrium relations are

$$\boldsymbol{P} = \frac{\partial A}{\partial \boldsymbol{F}}(\boldsymbol{F}^e, T, \epsilon^p) = \frac{\partial W^e}{\partial \boldsymbol{F}^e}(\boldsymbol{F}^e, T)\boldsymbol{F}^{p-T} \ , \tag{3.15a}$$

$$N = -\frac{\partial A}{\partial T}(\boldsymbol{F}^e, T, \epsilon^p) = -\frac{\partial W^e}{\partial T}(\boldsymbol{F}^e, T) - \frac{\partial W^p}{\partial T}(\epsilon^p, T) + RC_v \log \frac{T}{T_0} \ , \tag{3.15b}$$

$$y = -\frac{\partial A}{\partial \epsilon^p}(\boldsymbol{F}^e, T, \epsilon^p) = \left(\boldsymbol{F}^{eT} \frac{\partial W^e}{\partial \boldsymbol{F}^e}(\boldsymbol{F}^e, T)\right) \cdot \boldsymbol{M} - \frac{\partial W^p}{\partial \epsilon^p}(\epsilon^p, T) \equiv \sigma - \sigma_c \ , \tag{3.15c}$$

where N is the entropy per unit undeformed volume, y is the thermodynamic force conjugate to ϵ^p, or overstress, σ is the effective Mises stress and σ_c is the flow stress. Alternatively, the internal energy density corresponding to (3.14) is

$$E(\boldsymbol{F}^e, N(T), \epsilon^p) = W^e(\boldsymbol{F}^e, T) + RC_v T + W^p(\epsilon^p, T) \ . \tag{3.16}$$

In order to complete the model we shall assume a kinetic relation of the form

$$\dot{\epsilon}^p = \frac{\partial \psi}{\partial y}(y), \tag{3.17}$$

where $\psi(y)$ is a kinetic potential. We shall also find it useful to introduce the dual kinetic potential through the Legendre transformation

$$\psi^*(\dot{\epsilon}^p) = \max_y \{ y\dot{\epsilon}^p - \psi(y) \} \ , \tag{3.18}$$

which has the property that

$$y = \frac{\partial \psi^*}{\partial \dot{\epsilon}^p}(\dot{\epsilon}^p), \tag{3.19}$$

which effectively inverts relation (3.17). Finally, we shall assume a Fourier law of heat conduction of the general form

$$\boldsymbol{H} = \frac{\partial \chi}{\partial \boldsymbol{G}} \ , \tag{3.20}$$

where $\boldsymbol{H}$ is the referential heat flux,

$$\boldsymbol{G} = -\frac{1}{T}\mathrm{Grad}T \tag{3.21}$$

and χ is a kinetic potential.

The reduction of the preceding constitutive equations to the effective incremental form (3.8) requires the application of a variational equation-of-state update. We may regard shear bands as the inner solution, or *boundary layer* in a matched asymptotic expansion [85, 86]. In order to ascertain the local structure of the shear band, it therefore suffices to consider a planar band separating two semi-infinite bodies in a uniform state. Following Chapter 2, we introduce the functional

$$\begin{aligned} f_n(\boldsymbol{\varphi}_{n+1}, T_{n+1}, \epsilon^p_{n+1}, \boldsymbol{M}) = \\ \int_{-\infty}^{\infty} \Big\{ E(\boldsymbol{F}_{n+1}\boldsymbol{F}^{p-1}_{n+1}, N_{n+1}, \epsilon^p_{n+1}) - E_n - \frac{T_n^2}{T_{n+1}}(N_{n+1} - N_n) \\ + \triangle t \phi^* \left(\frac{T_n}{T_{n+1}} \frac{\epsilon^p_{n+1} - \epsilon^p_n}{\triangle t} \right) + \triangle t \chi(\boldsymbol{G}_{n+1}) \Big\} dZ \ , \end{aligned} \tag{3.22}$$

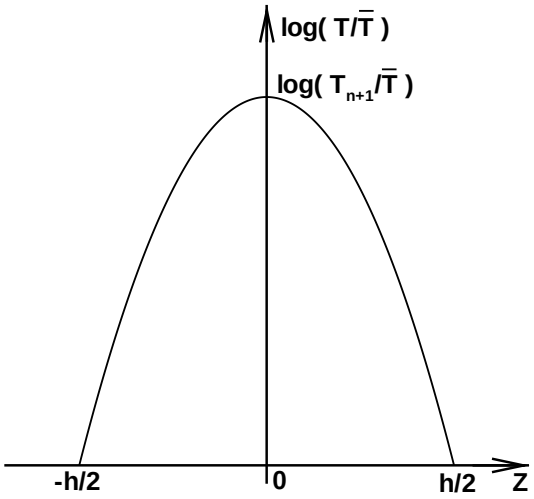

Figure 3.2: Gaussian temperature distribution in a shear band.

where Z is the coordinate normal to the band, all state variables are functions of Z, and we write

$$\boldsymbol{F}^p_{n+1} = \exp\left[(\epsilon^p_{n+1} - \epsilon^p_n)\boldsymbol{M}\right] \boldsymbol{F}^p_n \tag{3.23}$$

in order to express $\boldsymbol{F}^p_{n+1}$ as a function of ϵ^p_{n+1} and $\boldsymbol{M}$. The shear band profile follows as the minimizer of the functional $f_n(\boldsymbol{\varphi}_{n+1}, T_{n+1}, \epsilon^P_{n+1}, \boldsymbol{M})$ with appropriate boundary conditions at infinity.

In order to reduce the update to the solution of an algebraic problem we resort to a number of numerical approximations. Thus, we begin by assuming that the band is confined to the region $-h_{n+1}/2 \leq Z \leq h_{n+1}/2$, and, consequently, the integral in (3.22) is restricted to this interval. In addition, we adopt the kinematics (3.1), with the result that the uniform deformation $\boldsymbol{F}_{n+1}$ in the band follows directly from $\boldsymbol{F}^{\|}_{n+1}$ and $[\![\boldsymbol{\varphi}_{n+1}]\!]$, which are known from the deformation of the matrix surrounding the band. We additionally approximate the temperature profile across the shear band as being Gaussian, Fig. 3.2, i.e., as

$$\log \frac{T(Z, t_{n+1})}{\bar{T}_{n+1}} = \log \frac{T_{n+1}}{\bar{T}_{n+1}} \left[1 - \left(\frac{2Z}{h_{n+1}}\right)^2\right], \tag{3.24}$$

where $\bar{T}_{n+1}$ is the temperature of the surrounding matrix and T_{n+1} designates the temperature at the center of the band, which is the sole unknown parameter of the temperature profile. Other characteristic temperature profiles have been suggested by Wright and Ravichandran [86] and can be used in lieu of (3.24). Finally, we assume that the material obeys a linear Fourier law of the form

$$\boldsymbol{H} = kT_0\boldsymbol{G} \ , \tag{3.25}$$

where k is the thermal conductivity and T_0 is a reference temperature, so that

$$\chi = \frac{kT_0}{2}|\boldsymbol{G}|^2 \ . \tag{3.26}$$

In particular, the outward heat flux from the shear band is

$$H_{n+1} = \frac{4kT_0}{h_{n+1}} \log \frac{T_{n+1}}{\bar{T}_{n+1}} \ . \tag{3.27}$$

By virtue of this choice of χ and temperature profile across the band, the last term in (3.22) can be evaluated explicitly, with the result

$$\begin{aligned} &f_n(\boldsymbol{F}^{\parallel}_{n+1}, [\![\boldsymbol{\varphi}_{n+1}]\!], T_{n+1}, \epsilon^p_{n+1}, h_{n+1}, \boldsymbol{M}, \triangle t) = \\ &h_{n+1} \Big\{ E(\boldsymbol{F}_{n+1}\boldsymbol{F}^{p-1}_{n+1}, N_{n+1}, \epsilon^p_{n+1}) - E_n - \frac{T_n^2}{T_{n+1}}(N_{n+1} - N_n) \\ &+ \triangle t \phi^* \left(\frac{T_n}{T_{n+1}} \frac{\epsilon^p_{n+1} - \epsilon^p_n}{\triangle t} \right) \Big\} + \triangle t \, \frac{8kT_0}{3h_{n+1}} \left(\log \frac{T_{n+1}}{\bar{T}_{n+1}} \right)^2 \ , \end{aligned} \tag{3.28}$$

where we have additionally used the midpoint rule in order to evaluate the first term. The incremental state update may now be expressed in variational form as

$$\begin{aligned} &\phi_n(\boldsymbol{F}^{\parallel}_{n+1}, [\![\boldsymbol{\varphi}_{n+1}]\!]) \equiv \\ &\inf_{\{T_{n+1}, \epsilon^p_{n+1}, h_{n+1}, \boldsymbol{M}\}} f_n(\boldsymbol{F}^{\parallel}_{n+1}, [\![\boldsymbol{\varphi}_{n+1}]\!], T_{n+1}, \epsilon^p_{n+1}, h_{n+1}, \boldsymbol{M}, \triangle t) \ , \end{aligned} \tag{3.29}$$

subject to constraints (3.13a-3.13c). The Euler-Lagrange equations corresponding to (3.29) are

$$\frac{\partial f_n}{\partial T_{n+1}} = \frac{h_{n+1}T_n}{T_{n+1}^2}\left[T_n(N_{n+1}-N_n) - y(\epsilon^p_{n+1}-\epsilon^p_n)\right] + \triangle t\,\frac{16kT_0}{3h_{n+1}T_{n+1}}\log\frac{T_{n+1}}{\bar{T}_{n+1}} = 0\ , \tag{3.30a}$$

$$\frac{\partial f_n}{h\partial\epsilon^p_{n+1}} = -\sigma_{n+1} + \sigma_c(\epsilon^p_{n+1}, T_{n+1}) + \frac{T_n}{T_{n+1}}y = 0\ , \tag{3.30b}$$

$$\frac{\partial f_n}{h\partial \boldsymbol{M}} = -\left(\boldsymbol{F}^{eT}\frac{\partial W^e}{\partial \boldsymbol{F}^e}(\boldsymbol{F}^e, T)\right) - p\boldsymbol{I} - q\boldsymbol{M} = 0\ , \tag{3.30c}$$

$$\begin{aligned}\frac{\partial f_n}{\partial h_{n+1}} = \Big\{\, & E(\boldsymbol{F}_{n+1}\boldsymbol{F}^{p-1}_{n+1}, N_{n+1}, \epsilon^p_{n+1}) - E_n - \frac{T_n^2}{T_{n+1}}(N_{n+1}-N_n) \\ & + \triangle t\phi^*\left(\frac{T_n}{T_{n+1}}\frac{\epsilon^p_{n+1}-\epsilon^p_n}{\triangle t}\right)\Big\} - \triangle t\,\frac{8kT_0}{3h^2_{n+1}}\left(\log\frac{T_{n+1}}{\bar{T}_{n+1}}\right)^2 - \boldsymbol{T}_{n+1}\cdot\frac{[\![\boldsymbol{\varphi}_{n+1}]\!]}{h_{n+1}} = 0\ .\end{aligned} \tag{3.30d}$$

Eq. (3.30a) gives a time-discretized energy conservation equation for the band (cf Chapter 2). Eq. (3.30b) enforces the kinetic equation (3.19). Eq. (3.30c) optimizes the direction of incremental plastic deformation and thus enforces the Prandtl-Reuss flow rule and enforces constraints (3.13a) and (3.13c) by means of the Lagrange multipliers p and q. Finally, (3.30d) enforces the configurational equilibrium condition, and thus selects an optimal shear-band thickness. We note that the fraction of plastic work converted to heat (cf [38, 20]) need not be modelled independently, but follows as a consequence of the variational principle. At the optimum values of T_{n+1}, ϵ^p_{n+1} and $\boldsymbol{M}$, eq. (3.30d) simplifies to

$$\begin{aligned}h_{n+1}\frac{\partial f_n}{\partial h_{n+1}} &= \phi_n(\boldsymbol{F}^{\parallel}_{n+1}, [\![\boldsymbol{\varphi}_{n+1}]\!]) - \boldsymbol{T}_{n+1}\cdot[\![\boldsymbol{\varphi}_{n+1}]\!] - \triangle t\int_{-h/2}^{h/2}\boldsymbol{H}\otimes\boldsymbol{G}\,dZ \\ &= \boldsymbol{N}\cdot\boldsymbol{S}_{n+1}\boldsymbol{N}\ ,\end{aligned}$$

where

$$\boldsymbol{S} = h_{n+1}W_n\boldsymbol{I} - \boldsymbol{F}^T\boldsymbol{P} - \triangle t\int_{-h/2}^{h/2}\boldsymbol{H}\otimes\boldsymbol{G}\,dZ \tag{3.31}$$

is the generalized Eshelby's energy-momentum tensor (2.112) within the band for the coupled thermomechanical problem, $\boldsymbol{N}$ is the unit normal to the band, and $W_n = \phi_n/h_{n+1}$ is the effective energy density within the band. It follows from these identities that eq. (3.30d) is a statement of configurational equilibrium which requires the normal component of Eshelby's energy-momentum tensor to vanish across the band.

In order to derive the fundamental relations (3.9a) and (3.9b) we may consider perturbations

$$\boldsymbol{F}^{\parallel}_{n+1} \to \boldsymbol{F}^{\parallel}_{n+1} + \delta\boldsymbol{F}^{\parallel}_{n+1} \ ,$$
$$[\![\boldsymbol{\varphi}_{n+1}]\!] \to [\![\boldsymbol{\varphi}_{n+1}]\!] + [\![\delta\boldsymbol{\varphi}_{n+1}]\!] \ ,$$

inducing perturbations

$$T_{n+1} \to T_{n+1} + \delta T_{n+1} \ ,$$
$$\epsilon_{n+1} \to \epsilon_{n+1} + \delta\epsilon_{n+1} \ ,$$
$$\boldsymbol{M} \to \boldsymbol{M} + \delta\boldsymbol{M} \ ,$$
$$h_{n+1} \to h_{n+1} + \delta h_{n+1}$$

in the updated internal state. The corresponding variation of f_n is

$$\delta f_n = \frac{\partial E_{n+1}}{\partial \boldsymbol{F}^{\parallel}_{n+1}} \cdot \delta\boldsymbol{F}^{\parallel}_{n+1} + \frac{\partial E_{n+1}}{\partial [\![\boldsymbol{\varphi}_{n+1}]\!]} \cdot [\![\delta\boldsymbol{\varphi}_{n+1}]\!] + \frac{\partial f_n}{\partial T_{n+1}}\delta T_{n+1} + \frac{\partial f_n}{\partial \epsilon_{n+1}}\delta\epsilon_{n+1} + \frac{\partial f_n}{\partial \boldsymbol{M}} \cdot \delta\boldsymbol{M} + \frac{\partial f_n}{\partial h_{n+1}}\delta h_{n+1}. \tag{3.34}$$

But at the optimum point, the last four terms vanish by virtue of (3.30a-3.30d), and we obtain

$$\delta\phi_n = \frac{\partial E_{n+1}}{\partial \boldsymbol{F}^{\parallel}_{n+1}} \cdot \delta\boldsymbol{F}^{\parallel}_{n+1} + \frac{\partial E_{n+1}}{\partial [\![\boldsymbol{\varphi}_{n+1}]\!]} \cdot [\![\delta\boldsymbol{\varphi}_{n+1}]\!] \tag{3.35}$$

whence, recalling that the perturbations $\delta\boldsymbol{F}^{\parallel}_{n+1}$ and $[\![\delta\boldsymbol{\varphi}_{n+1}]\!]$ are arbitrary, (3.9a) and (3.9b) follow.

In order to illustrate how the variational approach just outlined determines a well-defined shear band thickness, we consider a model material characterized by: 1) an elastic internal energy density of the form

$$W^e(\boldsymbol{F}^e, T) = \frac{1}{2}\big(\log\sqrt{\boldsymbol{C}^e} - (T - T_0)\boldsymbol{\alpha}\big)\mathbb{C}\big(\log\sqrt{\boldsymbol{C}^e} - (T - T_0)\boldsymbol{\alpha}\big), \tag{3.36}$$

where

$$\boldsymbol{C}^e = \boldsymbol{F}^{eT}\boldsymbol{F}^e \tag{3.37}$$

is the elastic right Cauchy-Green deformation tensor, and $\mathbb{C}$ and $\boldsymbol{\alpha}$ are (possibly anisotropic) elastic

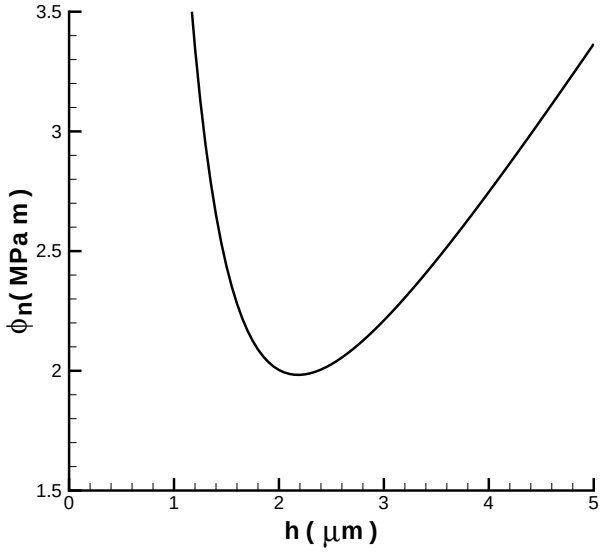

Figure 3.3: Variational shear band update of Ti-6Al-4V. The incremental work function ϕ_n is minimized at the band thickness of 2.2 μm.

moduli and thermal expansion coefficients, respectively; 2) the power-law stored-energy function

$$W^p = \frac{n\sigma_0(T)\varepsilon_0^p}{n+1}\left(1+\frac{\varepsilon^p}{\varepsilon_0^p}\right)^{(n+1)/n}, \tag{3.38}$$

where n is the hardening exponent, ε_0^p is a reference plastic strain, and $\sigma_0(T)$ is the flow stress; 3) a thermal-softening law of the form

$$\sigma_0(T) = \sigma_y\left(1-\frac{T}{T_m}\right)^l, \tag{3.39}$$

where σ_y is the yield stress at zero absolute temperature, l is the thermal softening exponent, and T_m is the melting temperature; and 4) a dual kinetic potential of the power-law form

$$\psi^* = \frac{m\sigma_y\dot{\varepsilon}_0^p}{m+1}\left(1+\frac{\dot{\varepsilon}^p}{\dot{\varepsilon}_0^p}\right)^{\frac{m+1}{m}} - \sigma_y\dot{\varepsilon}^p, \tag{3.40}$$

where m is the rate-sensitivity exponent and $\dot{\varepsilon}_0^p$ is a reference strain rate (cf, e.g., [6, 12]).

Consider a planar shear band undergoing a slip rate $[\![\dot{\boldsymbol{\varphi}}]\!] = 1$ m/s. The band is undeformed at

C	$\sigma_y(T_0)$	R	C_v	ϵ_0^p	$\dot{\epsilon}_0^p$	n	m	T_m	T_0	l
120 GPa	500 MPa	4480 Kg/m^3	523 J/Kg	0.05	0.0005	10	40	1500 K	293 K	1.0

Table 3.1: Material constants for Ti-6Al-4V [40].

time t_n and $T_n = T_0$. We wish to ascertain the state of the band at time $t_{n+1} = t_n + \triangle t$, with $\triangle t = 1 \times 10^{-6}$ s. The function obtained by minimizing the functional f_n with respect to T_{n+1}, ϵ^p_{n+1}, and $\boldsymbol{M}$ in (3.28) is shown in Fig. 3.3 for Ti-6Al-4V. The material constants used in this example are tabulated in Table 3.1. In addition, the thermal conductivity is $k = 18.8$ W/mK. As is evident from the figure, the resulting function $f_n(h_{n+1})$ has a well-defined minimum at $h_{n+1} \approx 2.2$ μm. This value is roughly within the range of experimental observation, e.g., in explosively deformed Ti-6Al-4V thick-walled cylinders [87].

3.4 Finite-element implementation

The effective incremental potential energy (3.10) arrived at in the preceding section is formally identical to the potential energy of an elastic solid containing cohesive cracks [21], and can be given an entirely analogous computational treatment. Following Ortiz and Pandolfi [21], we directly embed the strain-localization model into surface-like finite elements, leading to the formulation of *strain-localization elements*.

The class of elements considered here consists of two surface elements which coincide in space in the reference configuration of the solid, Fig. 3.4. Each of the surface elements has n nodes. The total number of nodes for the strain-localization band element is, therefore, $2n$. The particular case of six-node triangular elements is depicted in Fig. 3.4 by way of illustration. These elements are compatible with three-dimensional tetrahedral elements, Fig. 3.5.

The standard shape functions for each of the constituent surface elements are denoted by $N_a(s_1, s_2), a = 1, \ldots, n$, where (s_1, s_2) are the natural coordinates of each of the surface elements in some convenient standard configuration. We designate one of the surface elements as S^- and the other as S^+. All geometrical operations such as the computation of the normal are carried out

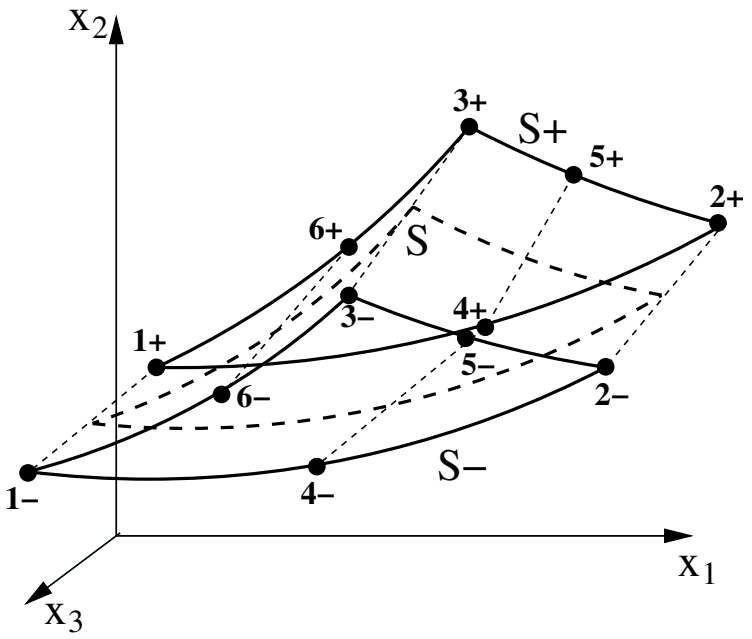

Figure 3.4: Geometry of shear band element. The surface S^- and S^+ coincide in the reference configuration of the solid.

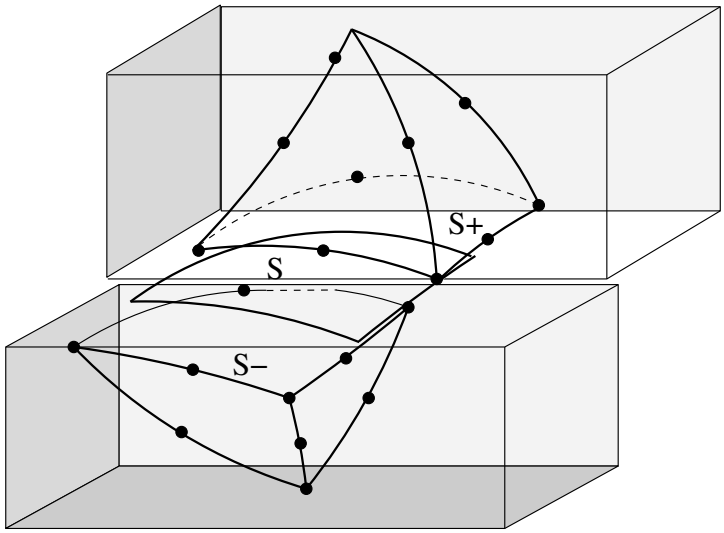

Figure 3.5: Assembly of one 12-node triangular shear band element and two 10-node tetrahedral elements.

on the *mid-surface* S of the element. The two surfaces of the element are defined parametrically as

$$\boldsymbol{X}(\boldsymbol{s}) = \sum_{a=1}^{n} \bar{\boldsymbol{X}}_a N_a(\boldsymbol{s}), \tag{3.41}$$

where

$$\bar{\boldsymbol{X}}_a = \frac{1}{2}\left(\boldsymbol{X}_a^+ + \boldsymbol{X}_a^-\right), \tag{3.42}$$

and $\boldsymbol{X}_a^{\pm}, a = 1, \ldots, n$ are the coordinates of the nodes in the undeformed configuration of the element. The natural coordinates (s_1, s_2) thus define a convenient system of curvilinear coordinates for the mid-surface of the element. The corresponding tangent basis vectors are

$$\boldsymbol{G}_\alpha(\boldsymbol{s}) = \boldsymbol{X}_{,\alpha}(\boldsymbol{s}) = \sum_{a=1}^{n} \bar{\boldsymbol{X}}_a N_{a,\alpha}(\boldsymbol{s}). \tag{3.43}$$

Here and subsequently, the conventions that Greek indices run from 1 to 2, and a comma denotes partial differentiation, are used. The unit normal to S is

$$\boldsymbol{N} = \frac{\boldsymbol{G}_1 \times \boldsymbol{G}_2}{|\boldsymbol{G}_1 \times \boldsymbol{G}_2|}, \tag{3.44}$$

which, conventionally, points from S^- to S^+. The displacement-jump vector is

$$[\![\boldsymbol{\varphi}]\!](\boldsymbol{s}) = \sum_{a=1}^{n} [\![\boldsymbol{x}_a]\!] N_a(\boldsymbol{s}), \tag{3.45}$$

where

$$[\![\boldsymbol{x}_a]\!] = \boldsymbol{x}_a^+ - \boldsymbol{x}_a^-. \tag{3.46}$$

where $\boldsymbol{x}_a^{\pm}, a = 1, \ldots, n$ are the coordinates of the nodes in the deformed configuration of the element. Evidently, $[\![\boldsymbol{\varphi}]\!]$ remains invariant under superposed rigid translations of the element.

In view of (3.10), the nodal forces contributed by the band are

$$f_{ia}^{\pm} = \frac{\partial}{\partial x_{ia}^{\pm}} \int_S \phi_n(\boldsymbol{F}_{n+1}^{\parallel}, [\![\boldsymbol{\varphi}_{n+1}]\!])\, dS, \tag{3.47}$$

which evaluate to

$$f_{ia}^{\pm} = \int_S \frac{\partial \phi_n}{\partial F_{mL}} \frac{\partial F_{mL}}{\partial x_{ia}^{\pm}} dS = \int_S h P_{mL} \frac{\partial F_{mL}}{\partial x_{ia}^{\pm}} dS. \tag{3.48}$$

In order to complete the formulation, the computation of the deformation gradient and its derivative with respect to the nodal positions is required. To this end, let $\boldsymbol{g}_\alpha$ denote the tangent basis vectors in the deformed configuration and $\boldsymbol{n}$ the unit normal defined by $\boldsymbol{g}_\alpha$. The definition of these bases is analogous to their reference configuration counterparts $\boldsymbol{G}_\alpha$ and $\boldsymbol{N}$, as given in (3.43) and (3.44). The in-plane deformation gradient then follows as (e.g., [88, 89])

$$\boldsymbol{F}^{\parallel} = \boldsymbol{g}_i \otimes \boldsymbol{G}^i \tag{3.49}$$

where $\boldsymbol{G}^i$ is the dual basis. Here and subsequently we adopt the the convention that $\boldsymbol{g}_3 = \boldsymbol{n}$ and $\boldsymbol{G}_3 = \boldsymbol{N}$. Recalling (3.1), we have

$$\frac{\partial F_{mL}}{\partial x_{ia}^{\pm}} = \frac{\partial F_{mk}^{\parallel}}{\partial x_{ia}^{\pm}} F_{kL}^{\perp} + F_{mk}^{\parallel} \frac{\partial F_{kL}^{\perp}}{\partial x_{ia}^{\pm}}. \tag{3.50}$$

Additionally, it follows from (3.3) and (3.45) that

$$\frac{\partial F_{kL}^{\perp}}{\partial x_{ia}^{\pm}} = \pm \delta_{ki} \frac{1}{h} N_a N_L, \tag{3.51}$$

where δ_{ki} is the Kronecker delta. Finally, from (3.49), (3.43) and (3.42), we obtain

$$\frac{\partial F_{mk}^{\parallel}}{\partial x_{ia}^{\pm}} = \frac{1}{2} \frac{\partial F_{mk}^{\parallel}}{\partial \bar{x}_{ia}} = \frac{1}{2} \delta_{mi} N_{a,\alpha} G^{\alpha k} + \frac{1}{2} \frac{\partial n_m}{\partial \bar{x}_{ia}} G^{3k}, \tag{3.52}$$

where (cf. [21])

$$\frac{\partial n_m}{\partial \bar{x}_{ia}} = \frac{e_{irs}}{2|\boldsymbol{g}_1 \times \boldsymbol{g}_2|} (g_{2r} N_{a,1} - g_{1r} N_{a,2})(\delta_{ms} - n_m n_s), \tag{3.53}$$

with e_{irs} the alternator tensor. The nodal forces now follow by substituting (3.50), (3.51) and (3.52) into (3.48). It should be noted that the integral extends over the undeformed surface of the element in its reference configuration. As is customary in isoparametric finite elements, the integral may conveniently be approximated by using numerical quadrature.

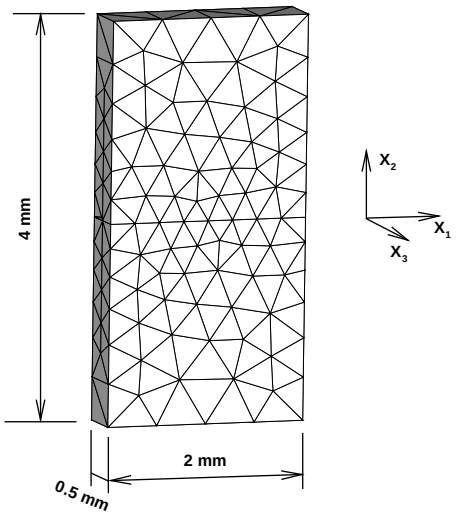

Figure 3.6: Geometry for the simple shear test: 558 tetrahedral elements and 32 strain-localization elements.

3.5 Simple-shear test

The simple shear test provides an elementary illustration of the ability of the strain-localization element to capture displacement discontinuities. The geometry of the specimen and the computational mesh are shown in Fig. 3.6. The mid-section of the specimen that lies in the $X_1 - X_2$ plane is tiled with strain-localization elements. In order to further simplify the calculations we constrain the displacements in the X_2 (transverse) and X_3 (thickness) directions throughout the calculations. Thus, the only unconstrained degrees of freedom are the displacements in the X_1 or shearing direction. The specimen is given an initial velocity field $V_1 = \dot{\gamma} X_2$, and velocities $V_1 = \mp \dot{\gamma} L/2$ are prescribed on the top and bottom surfaces of the specimen, respectively, where L is the length of the specimen and $\dot{\gamma}$ is a nominal strain rate. The time step used in the calculations is $\triangle t = 1 \times 10^{-8}$s. The material obeys the J_2-plasticity model (3.36 – 3.40). The material constants used in the calculations correspond to C300 steel are collected in Table 3.2.

The coupled thermomechanical problem can be solved using the variational formulation described in Chapter 2. In particular, since the heat flux (3.27) emanating from the shear band has

Mass density	$R = 7830$ kg m^{-3}
Young's modulus	$E = 200$ GPa
Poisson's ratio	$\nu = 0.3$
Yield stress	$\sigma_y = 2000$ MPa
Reference plastic strain	$\epsilon_0^p = 0.01$
Reference plastic strain rate	$\dot{\epsilon}_0^p = 0.001$ s^{-1}
Hardening exponent	$n = 100$
Rate sensitivity exponent	$m = 70$
Melting temperature	$T_m = 1570$ K
Reference temperature	$T_0 = 293$ K
Specific heat	$C_v = 448$ J(kg $\cdot$ K)$^{-1}$
Thermal softening exponent	$l = 0.75$
Thermal expansion exponent	$\alpha = 11.2 \times 10^{-6}$ K^{-1}
Taylor-Quinney beta	$\beta = 0.9$

Table 3.2: Material constants for C300 steel.

almost no effect on shear band velocity [90], for simplicity we restrict the problem to the case of adiabatic heating and assume 90% plastic power is converted into heat. The evolution of the deformation and effective plastic strain field for a nominal strain rate of 10^4 s^{-1} is shown in Fig. 3.7. Clearly, the onset of the displacement discontinuity is well captured by the strain-localization element. The evolution of the displacement jump is plotted in Fig. 3.8. Since the mesh is relatively coarse and no mesh refining is used to resolve the large deformation in the band, this actually shows the key advantage of using strain-localization elements. Moreover, the variational formulation of shear band thickness update proposed in the current model does give the optimized shear band thickness, which indeed is a function of deformation, as indicated by Fig. 3.9.

3.6 Dynamic shear bands

In this section, we present a numerical investigation of the initiation and propagation characteristics of dynamic shear bands in C300 maraging steel. Our simulations attempt to reproduce the behavior observed in the experiments of Guduru *et al.* [22] in which pre-notched specimens, with a fatigue-induced notch tip, are impacted on the edge just below the notch by a cylindrical projectile in order to induce shear-dominated stress fields. The geometry of the specimen and impact arrangements are shown in Fig. 3.10. The dimensions of the sample are 254 mm $\times$ 95 mm $\times$ 12 mm. The projectile is 127 mm long and 50 mm in diameter. The computational mesh is shown in Fig. 3.11. The mesh is very fine along the expected shear band path. It is also finer in the bottom half of the sample,

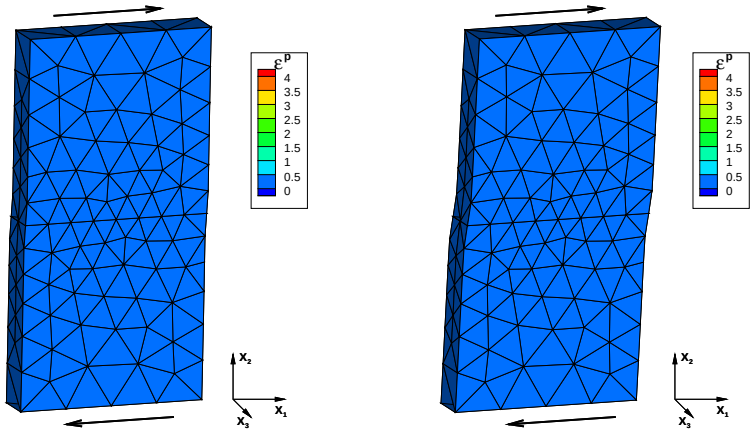

(a) $t = 3\ \mu$s (b) $t = 7\ \mu$s

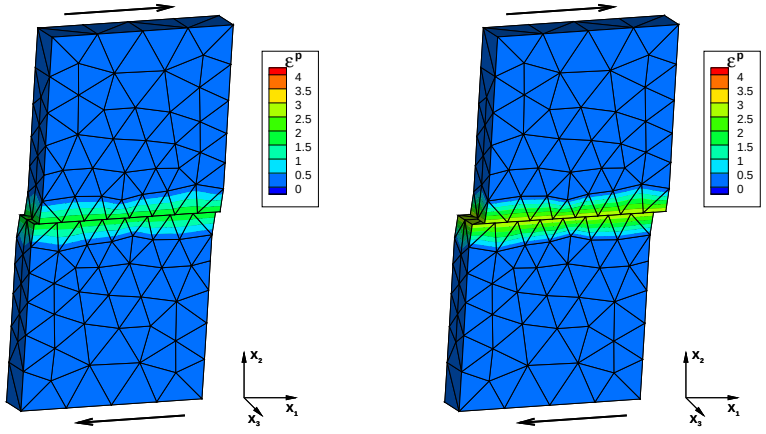

(c) $t = 9\ \mu$s (d) $t = 11\ \mu$s

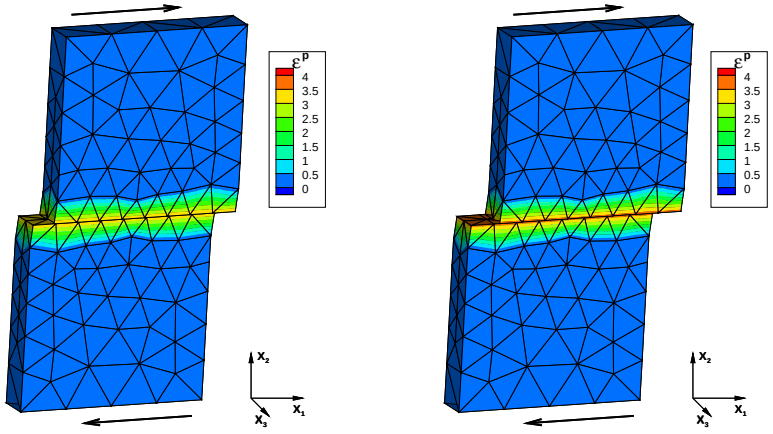

(e) $t = 13\ \mu$s (f) $t = 15\ \mu$s

Figure 3.7: Deformed mesh of simple shear test and contours of effective plastic strain.

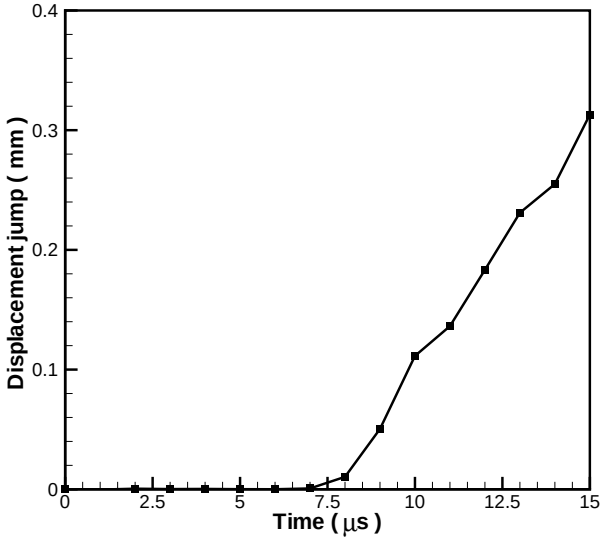

Figure 3.8: Evolution of displacement discontinuity for simple shear test.

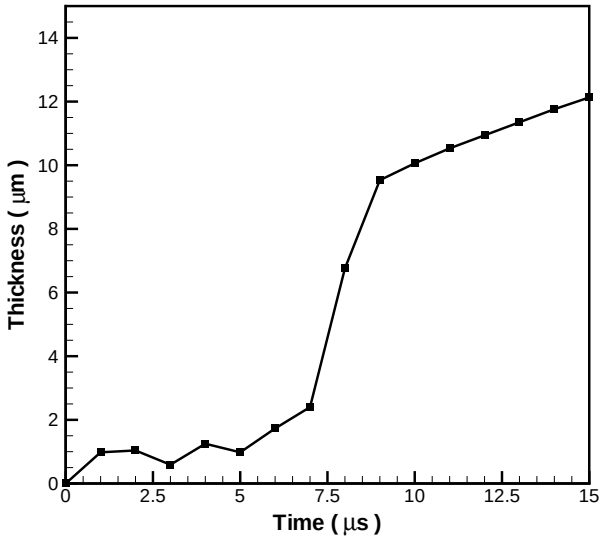

Figure 3.9: Variational shear band thickness update for simple shear test.

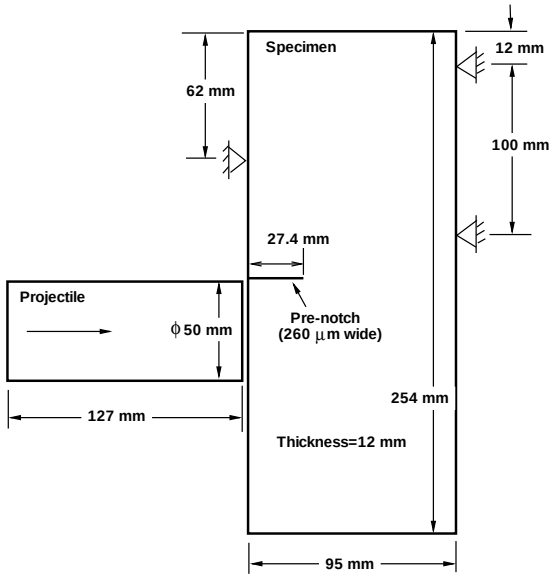

Figure 3.10: Configuration of specimen and impact arrangement [22].

where the impact occurs, and coarser in the top half. The minimum mesh size along the expected shear band path is 1mm, and thus the shear band thickness is not resolved by the mesh. Strain-localization elements are inserted adaptively between the surfaces of 10-nodes tetrahedral elements when the effective plastic strain reaches a critical level, e.g., 0.02. The material constants used in the calculations are again collected in Table 3.2. The steel projectile strikes the sample at 35 m/s and is assumed to remain elastic throughout the calculations.

A sequence of shear stress distributions after impact is shown in Fig. 3.12. The white line along the center of the shear stress concentration (blue) is the trace of the adiabatic shear band. The calculated shear band path replicates well the experimental observations by Guduru *et al.* [22]. The shear band advance as a function of time is plotted in Fig. 3.13. For purposes of comparison, experimental data at different impact speeds of 32 m/s, 35.3 m/s and 38 m/s are also plotted in the figure. The time of shear band initiation is somewhat delayed in the calculations due to the uncertainty in the notch-tip conditions and likely discrepancies between the computational model and experiment. By contrast, the computed shear-band speed following initiation is in good agreement with experiment. Thus, the computed average and peak shear-band speeds are roughly

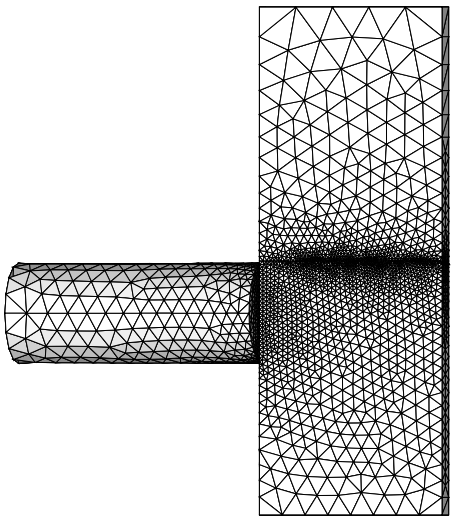

Figure 3.11: 3D mesh: $h_{\min} = 1$mm, $50,582$ nodes and $31,656$ elements.

500 m/s and 1000 m/s, respectively, which compares well with the experimental measurement of 1100 m/s at peak speed [22].

It bear emphasis that the shear-band thickness is updated variationally throughout the simulation. Fig. 3.14 illustrates the computed evolution of the thickness at the notch tip. It is interesting to note that the thickness grows steadily by one order of magnitude in the duration of the calculation. The computed thickness profile along the shear band path is plotted in Fig. 3.15. The thickness profile is in good agreement with the two-dimensional unsteady boundary-layer solutions of Gioia and Ortiz [85]. The calculated maximum band thickness of 15μm is also in good agreement with the experimental observations of Guduru *et al.* [22] which are indicative of shear bands roughly 20μm in thickness.

3.7 Summary and conclusion

We have developed a three-dimensional finite-deformation strain-localization element which enables the accurate and efficient simulation of strain-localization processes such as dynamic shear-band formation and propagation. The element treats the strain localization process as occurring at the

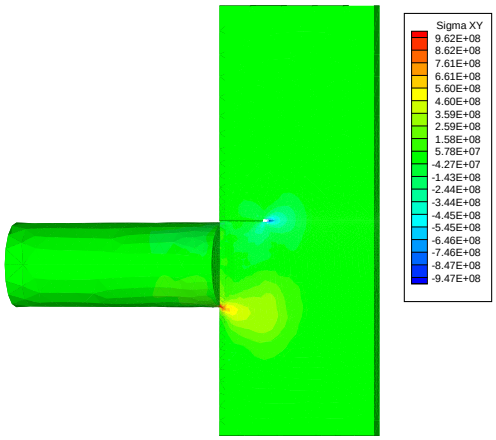

(a) $t = 10\ \mu$s

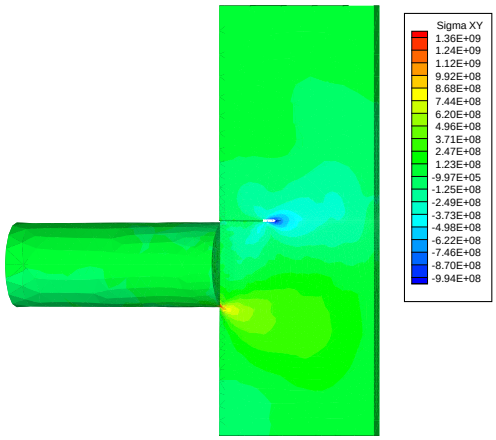

(b) $t = 20\ \mu$s

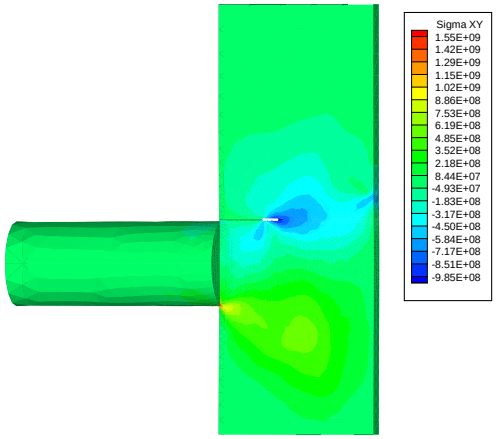

(c) $t = 30\ \mu$s

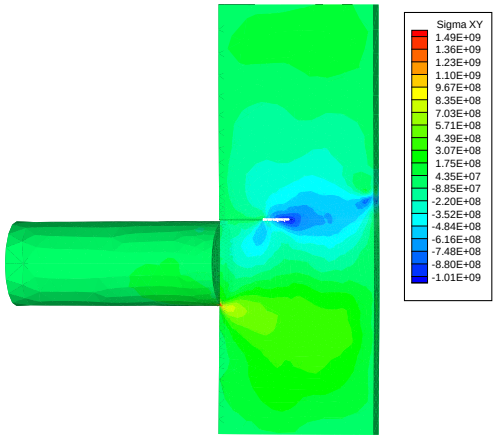

(d) $t = 40\ \mu$s

Figure 3.12: Sequence of images of deformed configurations showing the propagation of the shear band. Contours of shear stress (σ_{xy}) (Pa).

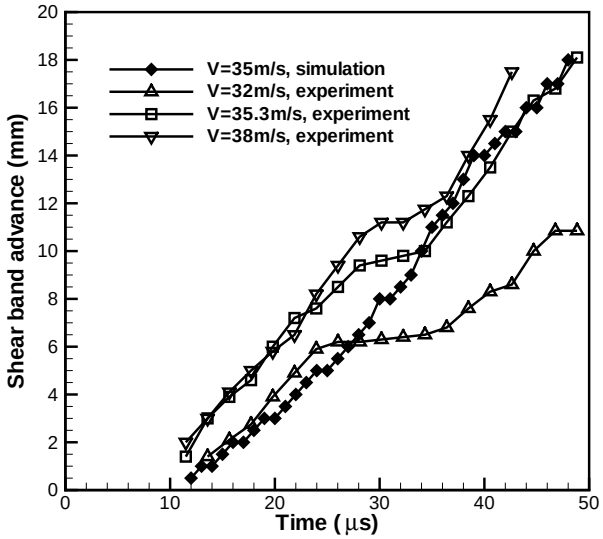

Figure 3.13: Shear band advance as a function of time. Experimental data are taken from [22].

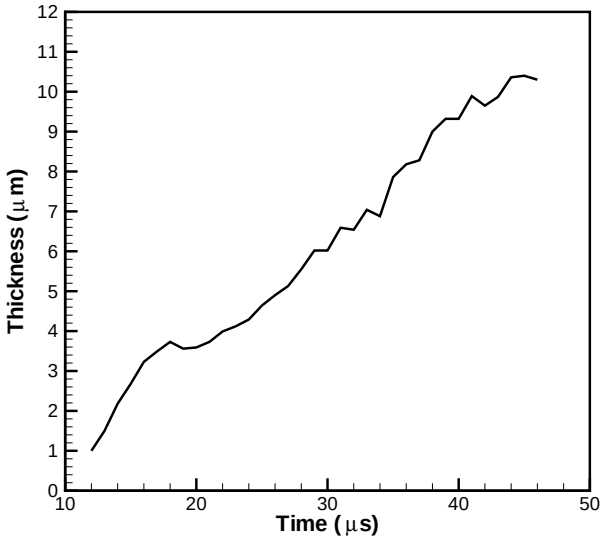

Figure 3.14: Shear band thickness as a function of time at the notch tip.

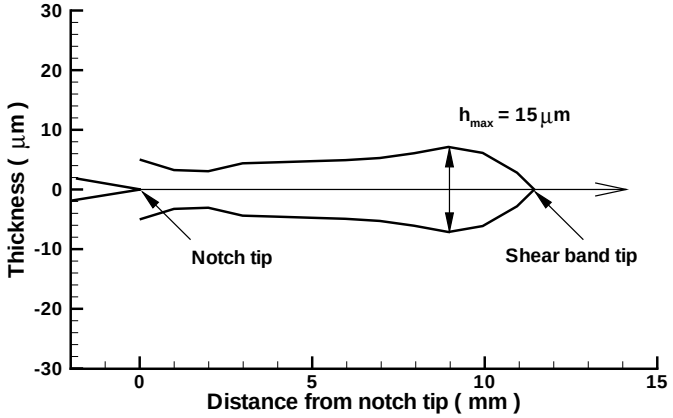

Figure 3.15: Shear band thickness profile along the path of shear band propagation at $t = 36$ μs.

sub-grid scale and thus the localized deformations appear as displacement discontinuities on the scale of the mesh. The band obeys the same constitutive law which governs bulk behavior, and no additional constitutive relations are necessary. The thickness of the band is determined as part of the solution by recourse to a variational principle. The strain-localization elements are endowed with full finite kinematics and are compatible with a conventional finite element discretization of the bulk material. The versatility and predictive ability of the method has been demonstrated through the simulation of dynamic shear band propagation. Good agreement between the numerical simulations and experimental results is obtained.

Chapter 4

A finite-deformation continuum model of bulk metallic glasses

4.1 Introduction

The first liquid-metal alloy (also known as metallic glass or amorphous metal) vitrified by cooling from the molten state was Au-Si, as reported by Klement *et al.* [91] in 1960. This was accomplished by using the rapid quenching techniques for chilling metallic liquids at very high strain rates of $10^5 \sim 10^6$ Ks^{-1}. The limited achievable size (normally in the range of microns) confined the study and application of metallic glasses until the development of bulk metallic glasses (BMGs) with much lower critical cooling rates (< 100 Ks^{-1}). The strong glass forming ability of the recently developed family of Zr-Ti-Cu-Ni-Be glasses by Peker and Johnson [92], with significantly lower critical cooling rates around 1 Ks^{-1}, allows these alloys to be cast in form of fully glassy rods with diameters ranging up to 50∼100 mm. This enables mechanical testing under a much wider range of loading conditions, including tension, compression and bending [93, 94, 95, 96, 27, 97, 98, 28]. Thus, the unique mechanical properties of metallic glasses, such as their ultra-high yield strength, large elastic strain limit and high fracture toughness, have been investigated extensively and thoroughly.

Quasi-static tests by Bruck *et al.* [93] indicate that $\mathrm{Zr}_{41.2}\mathrm{Ti}_{13.8}\mathrm{Cu}_{12.5}\mathrm{Ni}_{10}\mathrm{Be}_{22.5}$ bulk metallic glass (Vitreloy 1) exhibits a yield strength of 1.9 GPa and a 2% elastic strain in tension or compression at room temperature. The failure strains for compression tests are of the order of 3.5∼4%, which are slightly higher than the failure strains in tensile experiments [93]. Bruck *et al.* [94] reported later that the ultimate fracture stress is insensitive to the strain-rate in their dynamic compression tests at room temperature. All these properties were further confirmed experimentally

by Subhash *et al.* [97] and Lu *et al.* [27, 98]. It has been observed, however, that the deformation of Vitreloy 1 BMG is very sensitive to the loading rate and temperature when the latter is near or above the glass transition temperature, T_g, i.e., in the supercooled liquid region [27, 98]. Furthermore, a fracture toughness of 55$\sim$59 MPa$\sqrt{\text{m}}$ has been measured in a 3-point single notch bending configuration by Conner *et al.* [95]. Wider ranges of fracture toughness for the Vitreloy family were also reported by Lowhaphandu *et al.* [96] on specimens with various notch root radii. Due to their unique properties, bulk metallic glasses and their composites have been proposed for many potential applications, ranging from golf clubs to ballistic penetrators [99].

The development of bulk metallic glasses also allows the study of the kinetic properties of metallic glasses in the equilibrium melt or supercooled state. Experimental studies show that the viscosity of Vitreloy 1 decreases exponentially with the increase of temperature with a variation over 15 orders of magnitude [100, 99]. Based on the free volume model by Cohen and Grest (CG) [101], the viscosity can be expressed alternatively in terms of the average free volume per atom by using a linear relation between the free volume and the temperature [102]. Better agreement with experimental data can be achieved by using a non-linear temperature-dependent free volume relation [102, 103]. In the supercooled liquid region, the flow is Newtonian and therefore the viscosity in this region is called Newtonian viscosity. Beyond this region, a transition from Newtonian to non-Newtonian flow was observed by Lu *et al.* in uniaxial compression tests [27, 98]. When the temperature is close to or below the transition temperature, it was found that higher strain rates lead to a remarkable decrease in the viscosity. Based on these experimental data, a phenomenological expression for the viscosity as a function of the temperature and strain rate was obtained [104] to describe their effects on stress-strain curves of Vitreloy 1 in the homogeneous regime [27, 98].

Various micromechanical theories have been proposed to account for the mechanical behavior of metallic glasses. It has been shown [105] that the flow in metallic glasses is extremely inhomogeneous at high stresses and low temperatures, and that the highly localized deformation (stain softening) in shear bands is related to a local change in viscosity. Particularly, there are two competing hypotheses that explain strain localization in BMGs in terms of a decrease in viscosity. Originated by Spaepen [106], the first hypothesis argues that this decrease is due to the formation of free volume and the introduced inhomogeneous flow is therefore controlled by the competition between

the stress-driven creation and diffusional annihilation of free volume. This hypothesis was then demonstrated by Argon [107], who analyzed the flow localization in a band of material by perturbing the strain rate due to the creation of free volume. Steif *et al.* [108] extended Spaepen's model by assuming an infinite body containing an initial band of slightly weaker material and deriving an expression for the critical stress at which catastrophic softening due to the creation of free volume occurs. On the other hand, the second hypothesis argues that the decrease in viscosity is due to temperature rise by local adiabatic heating beyond the glass transition temperature [109]. Nevertheless, no significant temperature increase was obtained by Wright *et al.* [110] in their quasi-static uniaxial compression tests based on the calculation of local adiabatic heating due to plastic work. Direct measurements of the temperature rise by using high-speed infrared detection [94] indicated, however, that the temperature in the shear band was indeed increased by 480K, with a temperature much higher than the transition temperature of Vitreloy 1, approaching to the melting temperature of 936K [92]. Further studies and investigations are needed to uncover the precise nature of the strain localization mechanisms of bulk metallic glasses.

One of the primary interests of having a continuum model of BMG is its application to numerical simulations by the finite element method. To the best of our knowledge, very few models have been proposed to this end. For instance, Huang *et al.* [111] provide a framework within the context of continuum mechanics in which an inelastic dilatational strain associated with the excess free volume is introduced as an internal variable, in addition to the deviatoric plastic flow. This model, however, is limited to a qualitative analysis and cannot account for the finite, typically large deformation in shear bands due to its assumption of small strains.

In this chapter, we present a general macroscopic description of the constitutive behavior of bulk metallic glass by assuming that it can be treated as a uniform continuum material. Following the finite deformation framework advanced by Ortiz and Stainier [12], we propose a constitutive model for bulk metallic glasses based on a free volume model. The free volume acts as an order parameter in the proposed staggered solution procedure. By modeling the transition of Newtonian viscosity to non-Newtonian viscosity with a universal free volume expression at various temperatures and strain rates, we show that it is the increase of free volume (thus the decrease of viscosity) that leads to strain softening of bulk metallic glasses, while temperature rise accelerates the localization of

deformation.

To investigate the behavior of our model in uniaxial compression, numerical simulations are performed in which two rigid blocks are joined by an inclined shear band. The developed continuum model is then used to reproduce the constitutive behavior of Vitreloy 1 BMG. The simulations are performed at various strain rates and temperatures, with excellent agreement between the numerical results and experimental data. Further validation is obtained by the finite element simulation of the shear banding in a Vitreloy 1 BMG plate subjected to symmetric bending. The strain-localization finite elements introduced in Chapter 3 are used to account for the multiple shear bands networking.

4.2 General formulation

Physically, the formation of metallic glasses is the consequence of frustrating the process of crystallization when melting alloys are cooling down [26]. This results in the highly disordered atomic microstructure containing plenty of free volume. Free volume of an atom, by definition, is its neighbor cage in which the atom can move without change of energy. According to [106], free volume acts as a measure of disorder in the system. Its role is essentially the same as what temperature does in finite plasticity, e.g., increasing free volume will decrease the flow stress. Moreover, evolution of free volume is also determined by the (effective) shear stress. Provided the similarities of these two phenomena, we shall formulate a continuum model for bulk metallic glasses, based on the formation of J_2 finite plasticity.

Following the variational formulation of J_2 finite plasticity, we assume a multiplicative decomposition of the deformation gradient $\boldsymbol{F}$ of the form

$$\boldsymbol{F} = \boldsymbol{F}^e \boldsymbol{F}^v \boldsymbol{F}^p \ , \tag{4.1}$$

in which $\boldsymbol{F}^e$ is the elastic part, $\boldsymbol{F}^p$ is the plastic part and $\boldsymbol{F}^v$ is the dilatational part associated with the free volume (to be defined later). We further assume that the elasticity and specific heat of the material are structure-insensitive, i.e., independent of internal processes. This leads to a free

energy density per unit undeformed volume of the form [12]

$$A(\boldsymbol{F}, \boldsymbol{F}^p, T, \xi, \boldsymbol{q}) = W^e(\boldsymbol{F}^e, T, \xi) + W^p(T, \xi, \boldsymbol{q}, \boldsymbol{F}^p) \ , \tag{4.2}$$

where W^e is the elastic strain-energy density, W^p is the stored energy of cold work, T is the absolute temperature, $\boldsymbol{q}$ is some appropriate set of internal variables and ξ is the concentration of free volume defined by

$$\xi = \frac{v_f}{v^*} \tag{4.3}$$

with v_f the average free volume per atom and v^* the critical (hard-sphere) volume. By material frame-indifference, the free energy simplifies to

$$A(\boldsymbol{F}, \boldsymbol{F}^p, T, \xi, \varepsilon^p) = W^e(\boldsymbol{C}^e, T, \xi) + W^p(T, \xi, \varepsilon^p) \ , \tag{4.4}$$

with $\boldsymbol{C}^e = \boldsymbol{F}^{p-T}\boldsymbol{C}\boldsymbol{F}^{p-1}$ the elastic right-Cauchy Green deformation tensor and ε^p the effective plastic strain. Here we restrict our attention to isotropic hardening and softening, hence ε^p may conveniently be identified as the sole internal variable.

Previous work has suggested that a von Mises criterion is suitable to describe the onset of flow localization and failure of metallic glasses [93]. Following the theory of J_2 plasticity, we assume that the flow rule which governs the evolution of $\boldsymbol{F}^p$ is of the form

$$\dot{\boldsymbol{F}}^p\boldsymbol{F}^{p-1} = \dot{\varepsilon}^p\boldsymbol{M} \ , \tag{4.5}$$

where $\boldsymbol{M}$ is the tensor that defines the direction of plastic flow, which can be any symmetric tensor satisfying the kinematic constraint

$$\mathrm{tr}\boldsymbol{M} = 0 \ , \tag{4.6}$$

$$\frac{2}{3}\boldsymbol{M}\cdot\boldsymbol{M} = 1 \ , \tag{4.7}$$

but is otherwise unspecified.

Further simplification is obtained by assuming that the volumetric and deviatoric elastic re-

sponses are decoupled, i.e.,

$$W^e(\boldsymbol{C}^e, T, \xi) = W^{e,\mathrm{vol}}(J^e, T, \xi) + W^{e,\mathrm{dev}}(\boldsymbol{C}^{e,\mathrm{dev}}, T), \tag{4.8}$$

where $J^e = \det(\boldsymbol{F}^e)$ is the Jacobian of the elastic deformation and $\boldsymbol{C}^{e,\mathrm{dev}} = J^{e-2/3}\boldsymbol{C}^e$ is the deviatoric elastic right Cauchy-Green deformation tensor.

Assume, for simplicity, that the isothermal bulk modulus and the specific heat at constant volume are constant. Then, the function $W^{e,\mathrm{vol}}(J^e, T, \xi)$ which embodies the equation of state of the material is found to be of the simple form

$$W^{e,\mathrm{vol}}(J^e, T) = \frac{K}{2}\left[\theta^e - \alpha_T(T - T_0) - (\xi - \xi_0)\right]^2 + \rho_0 C_v T\left(1 - \log\frac{T}{T_0}\right), \tag{4.9}$$

where $\theta^e = \log J^e$ is the elastic volumetric strain, K is the isothermal bulk modulus, α_T is the thermal coefficient, T_0 is a reference absolute temperature, ξ_0 is the initial reference concentration of free volume, ρ_0 is the mass density per unit undeformed volume, and C_v is the specific heat per unit mass at constant volume. The volumetric elastic energy define in (4.9) gives rise to a contribution of the free volume to the deformation gradient of the form

$$\boldsymbol{F}^v = \exp\left[-(\xi - \xi_0)\right]\boldsymbol{I}\ . \tag{4.10}$$

This expression is an extension of the small strain definition introduced by Huang *et al.* [111] to finite deformations.

We assume that the deviatoric elastic strain-energy density $W^{e,\mathrm{dev}}$ is quadratic in the deviatoric logarithmic elastic strain and is assumed to be of the form

$$W^{e,\mathrm{dev}} = \mu|\boldsymbol{e}^e|^2, \tag{4.11}$$

where μ is the shear modulus and $\boldsymbol{e}^e$ is the deviatoric part of the logarithmic elastic strain, i.e., $\boldsymbol{e}^e = \frac{1}{2}\log(\boldsymbol{C}^{e,\mathrm{dev}})$.

The computation of W^e and the corresponding dependence of the elastic moduli requires the evaluation of the exponential and logarithmic mappings and their first and second linearizations.

Simple explicit formulae for the evaluation of these objects may be found in [112].

The thermodynamic force conjugate to ε^p is

$$y = -\frac{\partial A}{\partial \varepsilon^p} = \sigma - \sigma_c \ , \tag{4.12}$$

where

$$\sigma = -\frac{\partial W^e}{\partial \varepsilon^p} = 2\frac{\partial W^e}{\partial \boldsymbol{C}^e} \cdot \boldsymbol{M} \tag{4.13}$$

is the effective Mises stress and

$$\sigma_c = \frac{\partial W^p}{\partial \varepsilon^p} \tag{4.14}$$

is the flow stress. We describe the rate-sensitivity of the material through a kinetic equation of the form

$$\dot{\varepsilon}^p = \frac{\partial \psi}{\partial y}(y) \ , \tag{4.15}$$

where $\psi(y)$ is a kinetic potential. Alternatively, (4.15) can be expressed in inverse form as

$$y = \frac{\partial \psi^*}{\partial \dot{\varepsilon}^p}(\dot{\varepsilon}^p) \ , \tag{4.16}$$

where the dual kinetic potential $\psi^*(\dot{\varepsilon}^p)$ follows from $\psi(y)$ by the Legendre transformation

$$\psi^* = \max_y \{y\dot{\varepsilon}^p - \psi\} \ . \tag{4.17}$$

Finally, we assume a linear rate-sensitivity with a dual kinetic potential of the form

$$\psi^* = \frac{\eta}{2}(\dot{\varepsilon}^p)^2 \ , \tag{4.18}$$

where η is the non-Newtonian viscosity (see Sec. 4.4). Experiments show that η is highly sensitive to the strain rate $\dot{\varepsilon}$, temperature T and concentration of free volume, i.e., $\eta = \eta(\dot{\varepsilon}, T, \xi)$. This functional relationship plays a key role in the relaxation and flow of bulk metallic glasses [106, 27, 98].

4.3 Flow equation and kinetic potential

Based on the free volume theory by Cohen and Turnbull [113, 114, 115], Spaepen [106] derived a flow equation for metallic glasses under a shear stress τ of the form

$$\dot{\gamma}^p = 2\nu_0 \exp\big(-\frac{\alpha v^*}{v_f}\big)\exp\big(-\frac{\Delta G^{\mathrm{m}}}{kT}\big)\sinh\big(\frac{\tau\Omega}{2kT}\big) \ , \tag{4.19}$$

where $\dot{\gamma}^p$ is the plastic shear strain rate, v_f is the average free volume per atom, v^* is a critical volume (e.g. the effective hard-sphere volume of an atom), α is a geometrical factor of order unity, ν_0 is the frequency of atomic vibration, ΔG^{m} is the activation energy, Ω is the atomic volume, k is Boltzmann's constant, and T is the absolute temperature. According to Spaepen, (4.19) is valid for both homogeneous and inhomogeneous deformation. Homogeneous flow occurs at low stresses and high temperature, in which flow takes place uniformly with each volume element contributing an equal amount of strain, similar to liquid flow. On the other hand, inhomogeneous flow is observed at high stress and low temperature where the flow is localized in a thin band.

Following Steif *et al.* [108], a stress-dependent viscosity η_N may be defined as

$$\eta_N = \frac{\tau}{\dot{\gamma}^p} = \frac{\tau}{2\nu_0 \exp\big(-\frac{\Delta G^{\mathrm{m}}}{kT}\big)\sinh\big(\frac{\tau\Omega}{2kT}\big)}\exp\big(\frac{\alpha v^*}{v_f}\big) \ , \tag{4.20}$$

where it is evident that slight variations in the free volume v_f may give rise to large changes in the viscosity. For low stresses, $\sinh\big(\frac{\tau\Omega}{2kT}\big) \approx \frac{\tau\Omega}{2kT}$, and the expression for linear Newtonian viscosity is recovered:

$$\eta_N = \eta_0 \exp\big(\frac{\alpha}{\xi}\big) \tag{4.21}$$

where $\xi = \frac{v_f}{v^*}$ and $\eta_0 = \frac{kT}{\nu_0\Omega}\exp\big(\frac{\Delta G^{\mathrm{m}}}{kT}\big)$ which can be fitted using experimental data [26]. Alternatively, a phenomenological model based on entropy can be used to describe the viscosity, which gives a prefactor $\eta_0 = h/v^*$, where h is Planck's constant. This results in $\eta_0 = 4 \times 10^{-5}$Pa s for Vitreloy 1 [103]. From this, we see that the temperature effect on η_0 is negligible. By contrast, the increase of free volume will decrease the viscosity dramatically, indicating that free volume plays a key role in the strain softening of metallic glasses.

We model a solid undergoing homogeneous multiaxial stress by replacing the shear stress τ in

(4.19) with the thermodynamic force $\sigma - \sigma_c$ and $\dot{\gamma}^p$ with $\dot{\varepsilon}^p$. Akin to J_2 plasticity, we obtain a Perzyna-type kinetic relation of the form

$$\dot{\varepsilon}^p = 2R\exp\big(-\frac{\alpha}{\xi}\big)\sinh\big[\frac{(\sigma-\sigma_c)\Omega}{2kT}\big] \ , \tag{4.22}$$

where $R = \nu_0\exp\big(-\frac{\Delta G^m}{kT}\big)$ is a parameter with units of frequency. The inverse kinetic relation follows as

$$\sigma - \sigma_c = \frac{2kT}{\Omega}\operatorname{arcsinh}\big[\frac{\dot{\varepsilon}^p}{2R\exp\big(\frac{-\alpha}{\xi}\big)}\big] \ . \tag{4.23}$$

For homogeneous flow, i.e. at low stress and high temperature, (4.23) can be simplified to the linear relation

$$\sigma - \sigma_c = \eta_N \dot{\varepsilon}^p \tag{4.24}$$

where η_N is given by (4.21). It follows that the dual kinetic potential takes the form

$$\psi^* = \frac{1}{2}\eta_N \left(\dot{\varepsilon}^p\right)^2 , \tag{4.25}$$

and

$$y = \frac{\partial \psi^*}{\partial \dot{\epsilon}^p} = \sigma - \sigma_c \ . \tag{4.26}$$

We assume that (4.25) can be extended to non-Newtonian flow, i.e., (4.18), by replacing the Newtonian viscosity with a non-Newtonian viscosity, while still retaining a dual kinetic potential of the form (4.25). The nonlinear behavior of the inverse kinetic relation is thus made implicit by means of the non-Newtonian viscosity. As we show in Sec. 4.7, a non-Newtonian viscosity and the quadratic dual kinetic potential are sufficient to describe the non-linear behavior of metallic glasses.

It should be noted that the flow stress σ_c in (4.23) acts as a threshold stress that determines the yielding point of metallic glasses. The existence of such a threshold stress has previously been suggested by Taub [116, 117], who attributed the threshold stress to an increase of the internal energy of the material, akin to the manner it is used for the free energy (4.2) in the present model.

In the steady state, the flow stress remains constant for a given temperature and strain rate, while the plastic strain increases. This suggests that the flow stress is not a function of plastic strain. However, strong dependence on temperature and strain rate is observed experimentally

[27], which leads to a phenomenological expression for the flow stress of the form

$$\sigma_c = a\eta(T, \xi, \dot{\varepsilon})\dot{\varepsilon} \ , \tag{4.27}$$

where a is a constant of order unity, $\dot{\varepsilon}$ is the strain rate and $\eta(T, \xi, \dot{\varepsilon})$ is the non-Newtonian viscosity, which will be discussed in the next section. It follows that the internal (stored) energy of plastic work is given by

$$W^p(\varepsilon^p, T, \xi) = \int_0^{\varepsilon^p} \sigma_c \, d\varepsilon^p = \sigma_c \varepsilon^p \ . \tag{4.28}$$

4.4 Non-Newtonian viscosity

As discussed in the previous section, homogeneous flow in metallic glasses exhibits a Newtonian viscosity at low stresses and high temperatures, while nonlinear behavior is observed at higher stresses and lower temperatures. Lu *et al.* [27, 98] performed compression experiments on Vitreloy 1 samples under a wide range of temperatures and strain rates, and observed the transition from Newtonian flow to non-Newtonian flow. Based on the experimental data, Johnson *et al.* [104] proposed an expression for the non-Newtonian viscosity of the form

$$\eta(\eta_N, \dot{\varepsilon}, T) = \frac{\eta_N}{1 + \frac{\eta_N}{\eta_0}\left[\frac{\eta_0 \dot{\varepsilon}}{G}\right]^{b(T)}} \ , \tag{4.29}$$

where η_N is the Newtonian viscosity given by (4.21), G is the shear modulus and $b(T)$ is a fitting function dependent on temperature. This expression provides a good approximate solution at relatively high temperatures; it is not applicable, however, when the temperature decreases beyond the glass transition temperature. For instance, at room temperature ($T = 293$ K), we have $b(T) \approx 1$ and (4.29) reduces to $\eta|_{T=293} = \frac{G}{\dot{\varepsilon}}$. Using this viscosity in the dual kinetic potential (4.25), yields a corresponding thermodynamic force $y = G$, which is much higher than the yield stress of metallic glass. To extend (4.29) to lower temperatures, while keeping the high temperature dependency the same as before, we modify the expression for the viscosity to be

$$\eta(\eta_N, \dot{\varepsilon}, T) = \frac{\eta_N}{1 + \frac{\eta_N}{\eta_0}\left[\frac{\eta_0 \dot{\varepsilon}}{\sigma_0}\right]^{b(T)}} \ , \tag{4.30}$$

where σ_0 is the driving thermodynamic force of the metallic glass at room temperature and $b(T) = 1.0 - 5.0 \times 10^{-5}(T - T_0)$ for Vitreloy 1.

4.5 Free volume update

4.5.1 Annihilation and generation

It is believed that free volume plays an important role during the strain-localization of bulk metallic glasses. The change of free volume (and its concentration) is associated with micro structural change in the sense of a strain-disordering process [118]. Free volume can be regarded as the measure of disorder in the system, i.e., it can be created by the applied shear stress squeezing an atom into a vacancy smaller than itself (disordering) or annihilated by a series of atomic jumps towards metastable equilibrium (reordering) [106]. On the other hand, the changes of superimposed mean stress or pressure may also change the state of metallic glasses. The sole effect of mean stress, however, is to increase or decrease the initial free volume in the system [119]. Moreover, this effect can reasonably be neglected when the pressure is low compared to the yield stress [96]. Since the mean stress effect on the flow behavior of metallic glasses is still uncertain, we focus our study on the generation of free volume due to applied effective shear stress.

The net rate of change of the free volume for sufficiently large applied stresses, when the creation rate is greater than the annihilation rate, is given by [108]

$$\dot{v}_f = v^* \nu_0 \exp\left[-\frac{\Delta G^{\mathrm{m}}}{kT}\right] \exp\left[-\frac{\alpha v^*}{v_f}\right] \times \left[\frac{2\alpha kT}{v_f S}\left(\cosh\frac{\tau\Omega}{2kT} - 1\right) - \frac{1}{n_D}\right] , \tag{4.31}$$

where n_D is the number of jumps required to annihilate a free volume equal to v^*, S is a material constant given by $\frac{2}{3}\mu\frac{1+\nu}{1-\nu}$, ν is Poisson's ratio and μ is the shear modulus. By taking $\xi = \frac{v_f}{v^*}$ and replacing τ with the effective Mises stress σ, we obtain a formula for the rate of free volume concentration as

$$\dot{\xi} = R \exp\left[-\frac{\alpha}{\xi}\right] \left[\frac{\alpha}{c_1 \xi}\left(\cosh\frac{\sigma}{c_2} - 1\right) - \frac{1}{n_D}\right] , \tag{4.32}$$

where

$$c_1 = \frac{v^* S}{2kT} \quad \text{and} \quad c_2 = \frac{2kT}{\Omega} . \tag{4.33}$$

It should be noted, as mentioned by Huang *et al.* [111], that $\dot{\xi}$ is sensitive to the values of the parameters in this equation; therefore, a careful selection of the parameters based on experimetal data is in order, as discussed in Sec. 4.7.

Another process which can change the local free volume concentration is diffusion, by which free volume is redistributed until it is spatially uniform. If the free volume diffusion is modeled by a vacancy-like mechanism, the net rate of free volume concentration is then governed by a diffusion-production equation of the form [111]

$$\dot{\xi}_{\text{net}} = D\nabla^2\xi + \dot{\xi} \ , \tag{4.34}$$

where D is the diffusivity. Clearly, a steady state is reached when the net production $\dot{\xi}_{\text{net}} = 0$. The mechanisms of free volume diffusion in metallic glasses, however, are not well understood. Particularly, it is not clear that the free volume diffuses by a vacancy-like mechanism. In our model, therefore, we neglect it and consider only 'adiabatic' free volume generation and annihilation.

4.5.2 Effect of temperature

Extensive experiments have shown that temperature has a significant influence on free volume [101, 102, 103, 100, 99]. Once a steady state is achieved, free volume reaches its maximum. The temperature dependence of free volume concentration at steady state above the glass transition temperature T_g (625 K for Vitreloy 1) can be described approximately by the linear Vogel-Fulcher relation

$$\xi_{\text{linear}} \sim \alpha_\xi (T - T_{\text{ref}}) \ , \tag{4.35}$$

where α_ξ is a thermal coefficient and T_{ref} is a reference temperature. A more accurate but more complicated three-parameter relation is given by Cohen and Grest's free volume model [101]. In this model, the free volume is calculated by inverting the Newtonian viscosity, i.e.,

$$v_f = \frac{v^*}{\alpha} \ln(\frac{\eta_{\text{exp}}}{\eta_0}) \ , \tag{4.36}$$

where η_{exp} is the measured experimental viscosity. The calculated free volume is then fitted into a three-parameter equation, in terms of ξ,

$$\xi_{3\text{p}} = \frac{1}{2d_1}\left[T - T_{\text{ref}} + \sqrt{(T - T_{\text{ref}})^2 + d_2 T}\right]. \tag{4.37}$$

Based on experimental measurements of Vitreloy 1 undercooled liquid under quasi-static loading, Masuhr et al. [102] found these three parameters to be $\alpha d_1 = 4933$ K, $T_{\text{ref}} = 672$ K, and $d_1 = 162$ K where α is a geometrical factor as in (4.19). The transition from Vogel-Fulcher behavior, $\xi_{3\text{p}} \sim (T - T_{\text{ref}})$, for large T to Arrhenius behavior, $\xi_{3\text{p}} \sim T$, for small T is captured by this equation. As the temperature decreases, the free volume also decreases. When the glass transition temperature T_g is reached, however, the liquid solidifies and the free volume does not decrease further with a decrease in temperature. Wright *et al.* [120] proposed a cutoff value, i.e., the free volume concentration at a temperature lower than the glass transition temperature is given by a constant $\xi_{3\text{p}}|_{T=T_g}$.

Alternatively, similar to (4.36), we advance an expression for the free volume of the form

$$\xi_{\text{uni}} = \frac{1}{\alpha}\ln(\frac{\eta}{\eta_0}) \ , \tag{4.38}$$

where η is the non-Newtonian viscosity given by (4.30). This gives a universal expression for the free volume at various temperatures and strain rates:

$$\xi_{\text{uni}} = \frac{\xi_{3\text{p}}}{1 - \frac{\xi_{3\text{p}}}{\alpha}\ln\left[1 + \left(\frac{\eta_0\dot{\varepsilon}}{\sigma_0}\right)^{b(T)}\exp\left(\frac{\alpha}{\xi_{3\text{p}}}\right)\right]} \ . \tag{4.39}$$

As an example, we plot in Fig. 4.1 the temperature dependence of the free volume concentration at a strain rate of 10^{-4} s^{-1} for Vitreloy 1, which clearly shows that this dependence is well captured by (4.39). Moreover, it is noteworthy that this expression also encompasses the strain rate dependence of the free volume. It follows that the viscosity at any temperature and strain rate can be obtained simply by

$$\eta = \eta_0 \exp(\frac{\alpha}{\xi_{\text{uni}}}) \ . \tag{4.40}$$

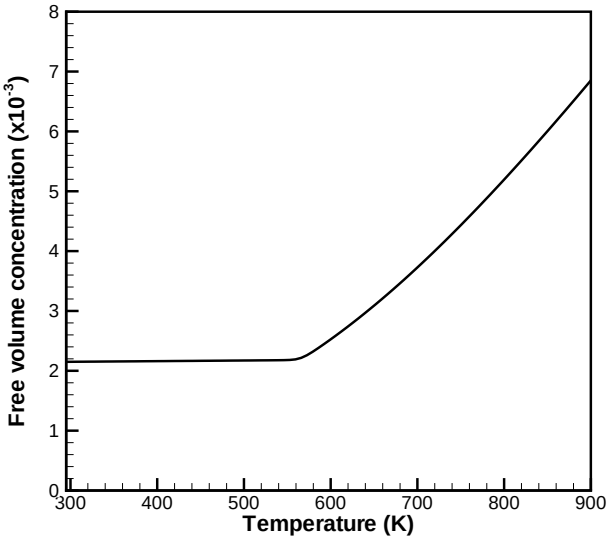

Figure 4.1: Temperature dependence of free volume concentration at a strain rate of 10^{-4} s^{-1}.

The temperature dependence of the viscosity at various strain rates is shown in Fig. 4.2. Evidently, the transition from Newtonian viscosity to non-Newtonian viscosity is well described by (4.40). Further validation of this expression is discussed in Sec. 4.7 by means of the simulation of a uniaxial compression test.

Finally, by considering both the effect of temperature and the net production of free volume, the total free volume concentration at state $\{\sigma,\ T\}$ can be written as

$$\xi(\sigma, T) = \xi_{\text{uni}} + \triangle t \dot{\xi} \ . \tag{4.41}$$

The initial free volume concentration at a stress-free state is therefore determined by $\xi_0 = \xi_{\text{uni}}$ and does not need to be specified initially as an *ad hoc* parameter.

4.6 Update algorithm

In this section, we describe an update algorithm for the BMG model by means of time-discretization, but we address first the issue of temperature rise in metallic glasses.

It is well known that, in the case of adiabatic heating, the temperature rise in most metals is due

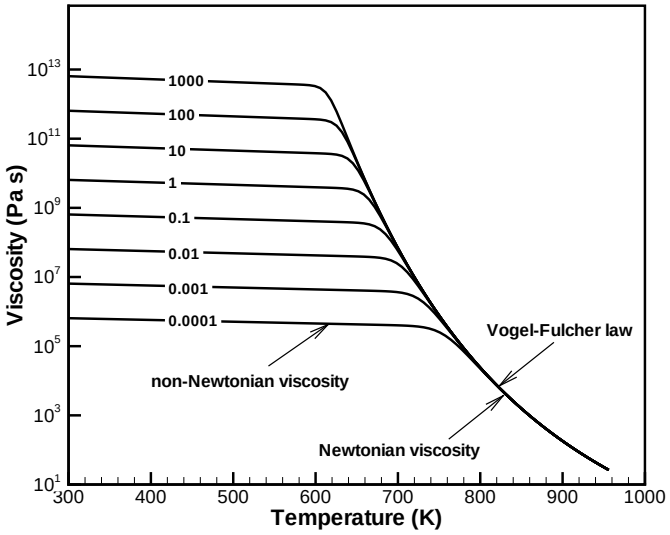

Figure 4.2: Viscosity of Vitreloy 1 dependent on temperature and strain rate, calculated from (4.39) and (4.40). The number on each curve indicates the strain rate (s^{-1}).

to the plastic deformation of the material. The fraction of plastic work converted into heat is either approximated to be a constant close to 1 [121], or updated within a variational thermodynamic framework, see Chapter 2. However, in the present model of metallic glasses, the temperature and free volume are directly related by the universal expression for the free volume (4.39). Following (4.39), the rate form of temperature rise, in terms of free volume, is given by

$$\rho_0 C_v \dot{T} = Q(T, \dot{\varepsilon})\dot{\xi} \ , \tag{4.42}$$

where

$$Q(T, \dot{\varepsilon}) = \frac{4\rho_0 C_v d_1 \sqrt{(T - T_{\text{ref}})^2 + d_1 T}}{4 d_1 \xi_{3\text{p}} + d_2} \frac{\xi_{3\text{p}}^3}{\xi_{\text{uni}}^2 \left[\xi_{3\text{p}} - \left(\frac{\eta_0 \dot{\varepsilon}}{\sigma_0} \right)^{b(T)} \exp \frac{\alpha}{\xi_{3\text{p}}} \right]} \tag{4.43}$$

in the case of $\dot{b}(T) \approx 0$. It follows from (4.42) that the temperature rise in metallic glasses is updated through the evolution of the free volume and cannot be modeled separately, i.e., the Taylor-Quinney relation is not applicable to metallic glasses. This may explain the discrepancies between temperature rise calculated by Wright *et al.* [110] from plastic work and experimental

observations [94]. In general, (4.42) can be written in the form of

$$\rho_0 C_v \dot{T} = Q(T, \dot{\varepsilon})\dot{\xi} - \nabla \cdot \boldsymbol{H} \ , \tag{4.44}$$

to account for the heat conducted away from the system, where $\boldsymbol{H}$ is the outward heat flux. In the cases of isothermal and adiabatic heating, we take the limits of $\dot{T} = 0$ and $\nabla \cdot \boldsymbol{H} = 0$, respectively.

Consider now a process of incremental deformation in which the deformation mapping is sampled at discrete times $t = 0, ..., t_n, t_{n+1} = t_n + \triangle t, ...$ We assume in addition that the incremental plastic behavior of the material is characterized by means of a variational update [12]. Define an incremental work function:

$$f_n(\boldsymbol{F}_{n+1}, T_{n+1}, \xi_{n+1}, \varepsilon^p_{n+1}) = A(\boldsymbol{F}_{n+1}, \boldsymbol{F}^p_{n+1}, T_{n+1}, \xi_{n+1}, \varepsilon^p_{n+1}) - A_n + \triangle t \phi^* \left(\frac{\triangle \varepsilon^p}{\triangle t} \right) \ . \tag{4.45}$$

The incremental strain-energy density $W_n(\boldsymbol{F}_{n+1}, T_{n+1}, \xi_{n+1})$ is determined by the problem:

$$W_n(\boldsymbol{F}_{n+1}, T_{n+1}, \xi_{n+1}) = \min_{\varepsilon^p_{n+1}} f_n(\boldsymbol{F}_{n+1}, T_{n+1}, \xi_{n+1}, \varepsilon^p_{n+1}) \ . \tag{4.46}$$

It follows that the stress update is given by

$$\boldsymbol{P}_{n+1} = \frac{\partial W_n}{\partial \boldsymbol{F}_{n+1}} \ . \tag{4.47}$$

In a manner similar to coupled thermo-mechanical problems (e.g., [122, 35]), the coupled mechanical and free volume updates are staggered by assuming constant free volume during the mechanical step and constant stress during the free volume step. In our implementation, a mechanical step is taken first based on the current distribution of free volume concentrations (and temperatures), with the generated free volume computed from (4.41). The corresponding temperature rise is then calculated using (4.44). The resulting free volume concentrations (and temperatures) are then incorporated into the general formulation of the finite deformation model described in Sec. 4.2, which completes one time-stepping cycle. This staggered procedure is summarized in Box 1.

i) Initialize $\xi_1 = \xi_0 + \triangle t\dot{\xi}, n = 0$.

ii) Compute T_{n+1} corresponding to ξ_{n+1} using (4.44).

iii) Mechanical step:

$$\{\boldsymbol{F}_n, \boldsymbol{P}_n, \xi_{n+1}, T_{n+1}\} \rightarrow \{\boldsymbol{F}_{n+1}, \boldsymbol{P}_{n+1}, \xi_{n+1}, T_{n+1}\}$$

iv) Free volume step:

$$\{\boldsymbol{F}_{n+1}, \boldsymbol{P}_{n+1}, \xi_{n+1}, T_{n+1}\} \rightarrow \{\boldsymbol{F}_{n+1}, \boldsymbol{P}_{n+1}, \xi_{n+2}, T_{n+1}\}$$

v) $n \rightarrow n + 1$, go to ii)

Box 1. Staggered procedure

It should be noted that, due to the staggered integration of the coupled mechanical and free volume updates, the free volume concentration ξ remains fixed during a mechanical step and, therefore, plays the role of a known parameter during a stress update.

4.7 Experimental validation of Vitreloy 1 under uniaxial compression

Geometry setup

A simple validation of the BMG model under uniaxial compression is performed by using the geometric model shown in Fig. 4.3. The model represents two rigid blocks separated by a shear band. Using suitable boundary conditions, the motion of the blocks is constrained to the plane of the shear band.

We choose global axes such that the relative motion of the blocks is constrained to the $x_1 - x_2$ plane. The shear band is inclined by an angle β relative to the x_1- axis. We additionally introduce local axes $x_1' - x_2'$ such that the x_1' axis is aligned with the shear band. With these assumptions,

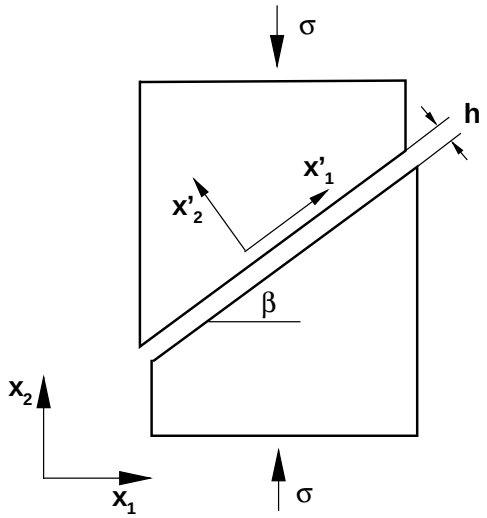

Figure 4.3: Geometry of shear band in specimen subjected to uniaxial compression.

the deformation gradient of the band at time t_{n+1} is

$$\boldsymbol{F}' = \begin{pmatrix} 1 & (u_1/h)\cos\beta + (u_2/h)\sin\beta & 0 \\ 0 & 1 - (u_1/h)\sin\beta + (u_2/h)\cos\beta & 0 \\ 0 & 0 & 1 \end{pmatrix} , \tag{4.48}$$

where $\{u_1, u_2\}$ are the global components of the displacement of the upper block relative to the lower block and h is the band thickness. We assume that the test takes place under displacement control and, consequently, u_2 is prescribed. Thus, the incremental work of deformation per unit cross-sectional area of the specimen is

$$E_n = \frac{h}{\cos\beta} W_n \ , \tag{4.49}$$

where W_n is defined by (4.46), and consequently $\boldsymbol{P}'$ is given by (4.47). The equilibrium condition for the lateral displacement u_1 is therefore

$$\frac{\partial E_n}{\partial u_1} = \frac{1}{\cos\beta}(P'_{12}\cos\beta - P'_{22}\sin\beta) = 0 \ . \tag{4.50}$$

This equation may be solved for u_1, e.g., by using a Newton-Raphson iteration. By work-conjugacy, the compressive axial stress in the specimen follows as

$$\sigma = P_{22} = \frac{\partial E_n}{\partial u_2} = P'_{22} + P'_{12} \tan\beta \ , \tag{4.51}$$

while the compressive axial strain is

$$\epsilon = \frac{u_2}{h\cos\beta} \ . \tag{4.52}$$

Plotting $\sigma \sim \epsilon$ gives the stress-strain curves. In the case of Vitreloy 1 bulk metallic glass, we choose $\beta = 45^o$ based on the experimental observation [93].

Mechanical Properties of $Zr_{41.2}Ti_{13.8}Cu_{12.5}Ni_{10}Be_{22.5}$ (Vitreloy 1)

We now turn to the selection of suitable material parameters for the modeling of Vitreloy 1. There are two types of parameters: some of them are general mechanical properties which are directly obtainable from simple mechanical experiments, such as Young's modulus and Poisson ratio [93, 94, 27, 98], while others need to be calculated based on available experimental data.

Recent experimental data on Vitreloy 1 by Lu *et al.* [27, 98] at various strain rates and temperatures were used for the determination of the second type of parameters. For example, a numerical fit of the authors' viscosity data for Vitreloy 1 results in an initial free volume concentration $\xi_0 = 0.002623$ at room temperature ($T = 295$K) and strain rate of $1 \times 10^{-4}\text{s}^{-1}$. Other numerical fits were used to obtain the temperature dependence of free volume concentration and the viscosity shown in Fig. 4.1 and 4.2, respectively.

The relevant mechanical properties and parameters of Vitreloy 1 used for our validation are listed in Table 4.1.

Validation Results

The objective of the first validation is to reproduce the quasi-static constitutive behavior of Vitreloy 1 at room temperature reported earlier by Bruck et al. [93]. As in the authors' test, the temperature and strain rate are set to $T = 295$ K and $\dot{\varepsilon} = 1.0 \times 10^{-4}$ s^{-1}, respectively. In addition, we assume that the whole procedure is under an isothermal condition. A comparison between the numerical

Young's modulus (at room temperature)	$E = 96$ GPa
Poisson's ratio (at room temperature)	$\nu = 0.36$
Yield stress (at room temperature)	$\sigma_y = 1.9$ GPa
Mass density (at room temperature)	$\rho = 6000$ kgm^{-3}
Melting temperature	$T_m = 936$ K
Transition temperature	$T_g = 625$ K
Reference temperature	$T_0 = 293$ K
Specific heat at constant volume	$C_v = 240$ J$(\text{kg} \cdot \text{K})^{-1}$
Thermal expansion coefficient	$\alpha_T = 4.0 \times 10^{-5}$ K^{-1}
Material parameter for flow stress	$a = 1.0$
Material parameter for η_N	$\eta_0 = 4.0 \times 10^{-5}$ Pa $\cdot$ s
Material parameter for $\xi_{\text{temp+rate}}$	$\sigma_0 = 0.5\sigma_y$
Geometrical factor	$\alpha = 0.105$
Number of jumps for annihilation	$n_D = 3$
Material parameter for $\dot{\xi}$	$c_1 = 135.6$
Material parameter for $\dot{\xi}$	$c_2 \approx (1.233 + 0.033 \log_{10} \dot{\varepsilon})\sigma_c$
Material parameter for $\dot{\xi}$	$R \approx (2.93 + 0.233 \log_{10} \dot{\varepsilon})T_0/T \ \times 10^{10}$ s^{-1}

Table 4.1: Mechanical properties and parameters for Vitreloy 1 ($Zr_{41.2}Ti_{13.8}Cu_{12.5}Ni_{10}Be_{22.5}$).

results and the experimental data is plotted in Fig. 4.4. The onset of yielding (1.9 GPa) and the elastic limit (0.02) are well captured by the model. Dynamic simulations at room temperature are also conducted by allowing $\dot{\varepsilon}$ to vary within the range of $10^{-4} \sim 10^4$ s^{-1}. No significant differences are observed in the stress-strain curves at room temperature due to this variation, as reported by experiments [94, 27].

Note that, after reaching a peak, the stress continues to decrease until a steady state is reached. Concurrently, the free volume concentration decreases in the early stage and then increases until it reaches the steady state, as shown in Fig. 4.5. To the best of our knowledge, this is the first time that a theoretical prediction of the free volume for a real bulk metallic glass is obtained, although qualitative analyses can be found elsewhere (e.g., [108, 111]). The steady state of the flow stress at room temperature, however, was not observed in the experiments due to the forming of shear bands which caused the failure of the specimens. To replicate this behavior with the model, we update the shear band temperatures adiabatically corresponding to the changes of the concentrations of free volume, i.e., (4.44). The calculated temperature evolutions are plotted in Fig. 4.6 at various strain rates. Note that the temperature decreases in the early stage and then increases, forming a dip on each curve. This indicates that the specimen cools and absorbs heat at small strains, specially

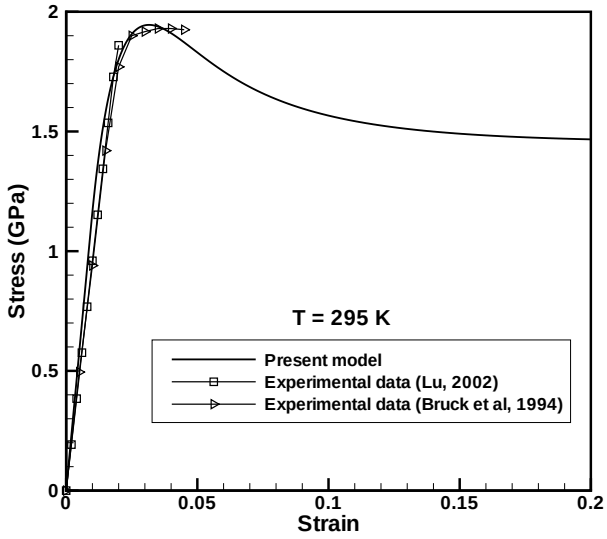

Figure 4.4: Quasi-static compression behavior of $Zr_{41.2}Ti_{13.8}Cu_{12.5}Ni_{10}Be_{22.5}$ BMG at room temperature and strain rate $\dot{\varepsilon} = 1.0 \times 10^{-4}$ s^{-1}. Experimental data (symbols) taken from Bruck et al. [93].

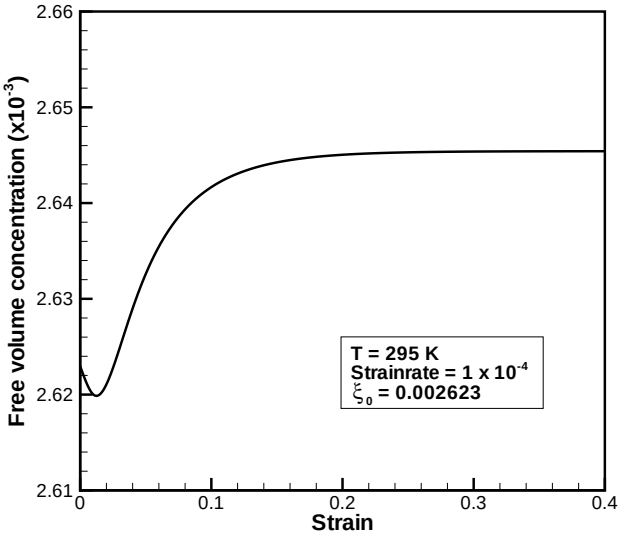

Figure 4.5: Free volume concentration vs. shear strain at room temperature (295 K) and strain rate of 1×10^{-4}s^{-1}.

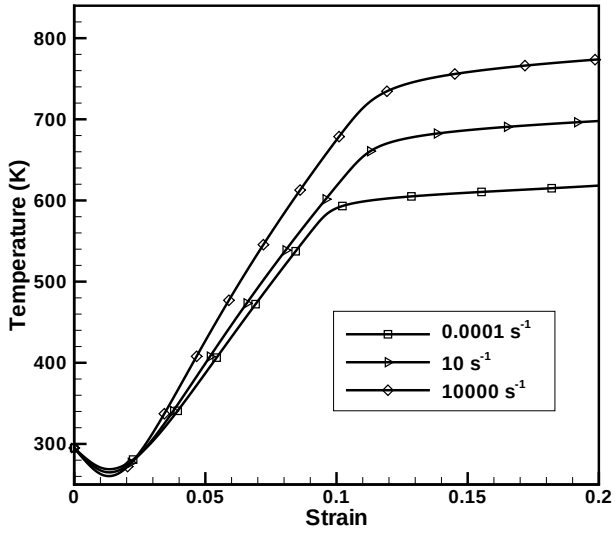

Figure 4.6: Temperature updates with adiabatic heating at strain rates of $\dot{\varepsilon} = 1.0 \times 10^{-4}$ s^{-1}, $\dot{\varepsilon} = 10$ s^{-1} and $\dot{\varepsilon} = 1.0 \times 10^{4}$ s^{-1}.

during the elastic region, which is consistent with the experimental observation that temperature rise due to adiabatic heating occurs only after the onset of inhomogeneous deformation (yielding) [94]. As shown in Fig. 4.6, significant temperature increases are also captured by the model. For instance, at a strain rate of 1×10^{4}s^{-1}, a temperature higher than 780 K is obtained which keeps increasing as the loading continues. This reproduces Bruck *et al.*'s experimental results [94], in which near-melting temperatures are measured by a high speed infrared thermal detector. The corresponding stress-strain curves are shown in Fig. 4.7. Comparing to the isothermal process, a significant decrease of the stress, i.e., strong strain softening, is obtained, which we believe accounts for the inhomogeneous deformation in shear bands. Thus, we conclude that the increase of free volume leads to strain softening in bulk metallic glasses, while the increase of the temperature (corresponding to the increase of free volume) accelerates the localization of the deformation and the failure of the material.

The influence of temperature in the stress-strain curve of Vitreloy 1 during homogenous isothermal deformation is investigated by performing numerical tests at various temperatures for strain rates of 1.0×10^{-4} s^{-1} (Fig. 4.8) and 1.0×10^{-1} s^{-1} (Fig. 4.9). The figures clearly show that the ma-

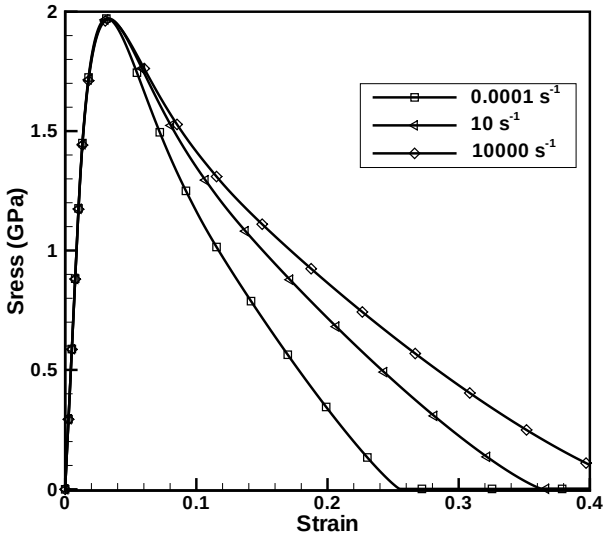

Figure 4.7: Stress-strain curves with adiabatic heating at strain rates of $\dot{\varepsilon} = 1.0 \times 10^{-4}$ s^{-1}, $\dot{\varepsilon} = 10$ s^{-1} and $\dot{\varepsilon} = 1.0 \times 10^{4}$ s^{-1}.

terial undergoes softening with increasing temperature. The softening becomes more pronounced as the temperature approaches the transition temperature, T_g, as is also observed experimentally in Vitreloy 1 bulk metallic glass [27]. Conversely, the theory predicts strain softening with the increase of strain for a given temperature in the range 573 K $\sim$ 623 K for strain rates of 1.0×10^{-4} s^{-1}, and an evident peak stress is observed. Eventually, the steady state is approached when the net production of free volume is zero, and the subsequent behavior is ostensibly ideally plastic.

The numerical stress-strain curves for Vitreloy 1 at various strain rates for a given temperature of 643 K are shown in Fig. 4.10. The figures show that the axial compressive stress of Vitreloy 1 increases with the increase of strain rate. Note, however, that this only happens when the temperature is high enough, for instance, close to the transition temperature for Vitreloy 1. As a limiting case, no strain rate effects are observed at room temperature, both in experiments [94] and in the present model.

According to Lu's experiments [27], no shear bands are observed to appear at relatively high temperatures. For instance, at $\dot{\varepsilon} = 1.0 \times 10^{-4}$ s^{-1}, the material undergoes homogeneous deformation when $T \geq 573$ K. The geometrical model, however, is still valid since our attention here is focused

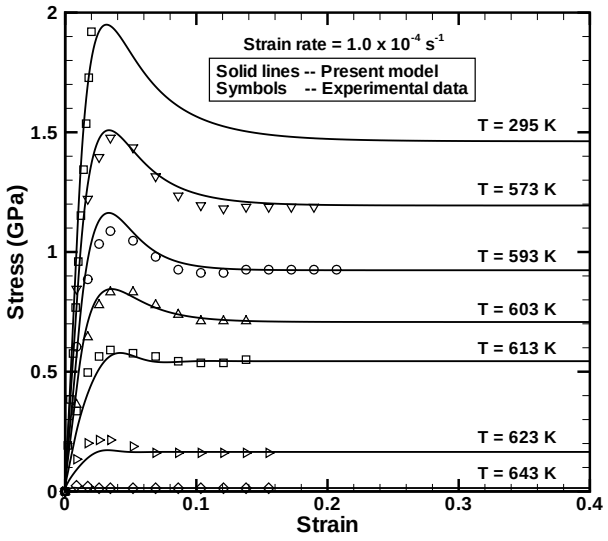

Figure 4.8: The effect of temperature on $Zr_{41.2}Ti_{13.8}Cu_{12.5}Ni_{10}Be_{22.5}$ BMG subjected to uniaxial compression at a strain rate $\dot{\varepsilon} = 1.0 \times 10^{-4}$ s^{-1}. Experimental data (symbols) taken from Lu [27].

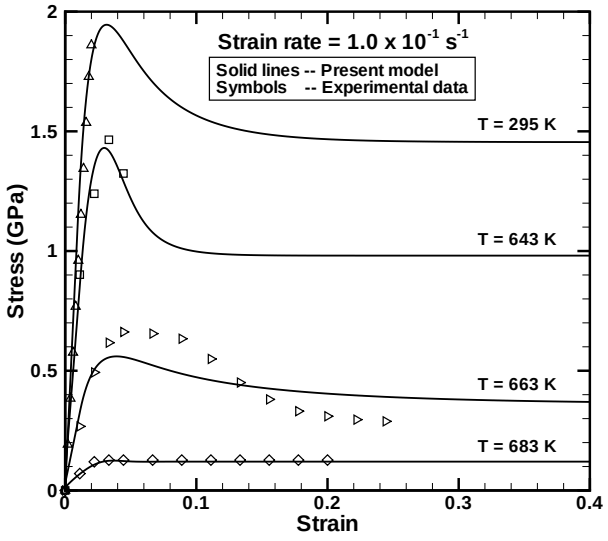

Figure 4.9: Temperature effects of uniaxial compression behavior of $Zr_{41.2}Ti_{13.8}Cu_{12.5}Ni_{10}Be_{22.5}$ BMG at strain rate $\dot{\varepsilon} = 1.0 \times 10^{-1}$ s^{-1}. The experimental curves (symbols) are taken from Lu [27].

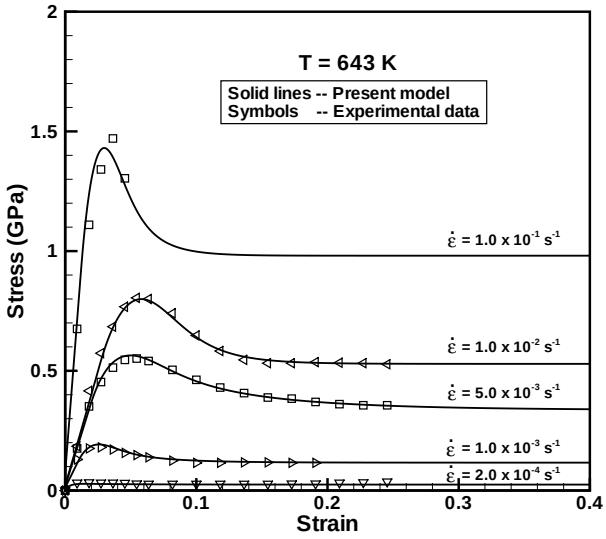

Figure 4.10: Strain rate effects of uniaxial compression behavior of $Zr_{41.2}Ti_{13.8}Cu_{12.5}Ni_{10}Be_{22.5}$ BMG at temperature $T = 643$ K. The experimental curves (symbols) are taken from Lu [27].

on the constitutive behavior of the material instead of its failure mechanism.

The excellent agreement between the present model and experimental data (Fig. 4.4 $\sim$ Fig. 4.10) demonstrates that our continuum model captures very well the key features of the behavior of bulk metallic glasses. Moreover, it is noteworthy that the model can be easily implemented in a finite element code, which makes possible the effective numerical simulation of the dynamic behavior of bulk metallic glasses, as shown in next section.

4.8 Shear banding of metallic glass plate under bending

It is well known that bulk metallic glasses fail at room temperature without significant plastic deformation [93, 94, 27]; but upon yielding, metallic glasses tend to form localized shear bands. The localization of shear is associated with the strain softening caused mainly by the local increase of the free volume. More interestingly, a recent experimental study shows that shear bands in a plate under bending are likely to form a pattern with an average spacing associated with the plate thickness [28]. One argument which tries to rationalize this phenomenon is that the strain relaxation of the material in the vicinity of the shear band causes the shear band spacing [28]. In

this section, we present a numerical investigation of the shear band spacing in a Vitreloy 106 bulk metallic glass plate under symmetric bending.

In the previous section we mentioned that the model of bulk metallic glasses is suitable for use in finite element calculations. This, together with the development of variational strain-localization finite elements (cf Chapter 3), makes it possible to perform finite element simulation of the shear banding of bulk metallic glasses. For simplicity, we assume here that the shear band thickness is constant and consider the variational thickness update discussed in Chapter 3 for further studies.

As shown in Fig. 4.11, we consider a metallic glass plate with thickness of 0.6 mm and length of 3 mm subjected to plane-strain bending, with a minimum element size of 30 μm. The width of plate is set to 0.06 mm to reduce the mesh size. For simplicity, only the top half of the plate is meshed. We assume that the mid-plane acts as a neutral surface (no lateral strain), where a displacement boundary condition is applied by changing the radius of curvature with a bending angle rate of 1×10^4 s^{-1}. The three-dimensional computational mesh is shown in Fig. 4.11. Strain-localization elements are inserted adaptively between the surfaces of 10-node tetrahedral elements when the shear stress reaches a critical level of $\sigma_y/\sqrt{3}$ (where σ_y is the yield stress). Since the material properties of the Vitreloy 1 family are almost the same [99], we use the same material constants collected in Table 4.1 for Vitreloy 106. The shear band thickness used in the strain-localization elements is assumed to be an empirical constant of 1 μm.

The deformed configuration of the plate at 4 μs is shown in Fig. 4.12. The shear-band-induced displacement jumps are readily visible, resulting in an average shear band spacing of 90 μm, which is 15% of the plate thickness. It is noteworthy that the formation of multiple shear bands in metallic glasses under bending comes naturally from the finite element simulations. Due to the assumption that the material is homogeneous and isotropic, it is noted that a number of stain-localization elements are inserted at the early stage of bending during the simulation. When some of them start to propagate, their nearby stress fields are relaxed. The propagating strain-localization elements then dominate and form macro-visible shear bands with a certain band spacing, while most other stain-localization elements are arrested and staticized.

Numerical simulations of shear band spacing at various plate thicknesses are also conducted. The obtained shear band spacing is observed to increase with increasing plate thickness, as shown

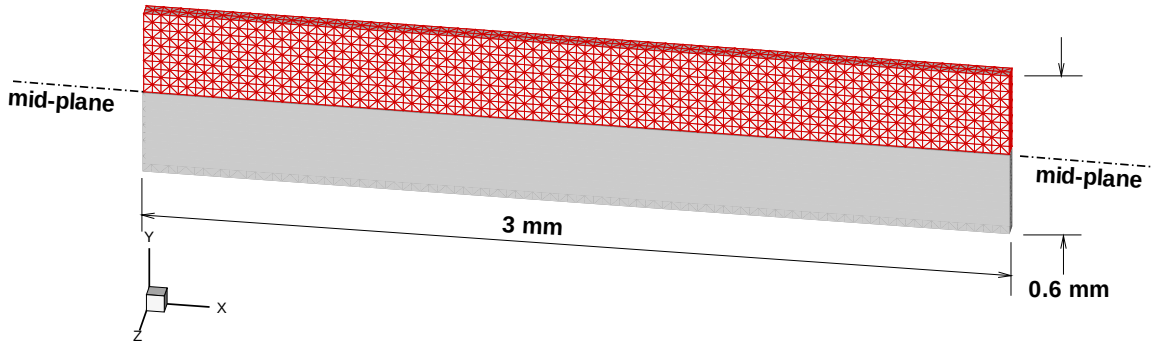

Figure 4.11: Geometry and mesh for plane-strain bending. The top half of the plate is meshed with 6664 tetrahedral elements and 13989 nodes. Displacement boundary conditions are applied along the mid-plane.

in Fig 4.13. This relationship is similar to the experimental observations by Conner *et al.* [28]. The existence of multiple shear bands in thin plates, with typical thickness less than 1 mm, delays the failure of metallic glasses. Thus, it suggests that very thin metallic glass specimen might exhibit particularly high ductility corresponding to monolithic metallic glasses.

4.9 Summary and conclusions

We present a variational finite-deformation constitutive model for bulk metallic glasses based on the evolution of free volume. In the staggered mechanical and free volume update procedure, free volume acts as a known parameter during the mechanical step. A universal free volume equation as a function of the temperature and strain rate is proposed to model the transition from Newtonian flow to non-Newtonian flow. It is shown that the strain softening of bulk metallic glasses is due to the increase of free volume, while temperature rise accelerates the localization of deformation. The validation of the model is demonstrated through the simulation of a uniaxial compression test, and the prediction of shear band spacing for a BMG plate subjected to bending simulated using finite elements. The agreement between experimental observations and the predictions of the model is remarkable.

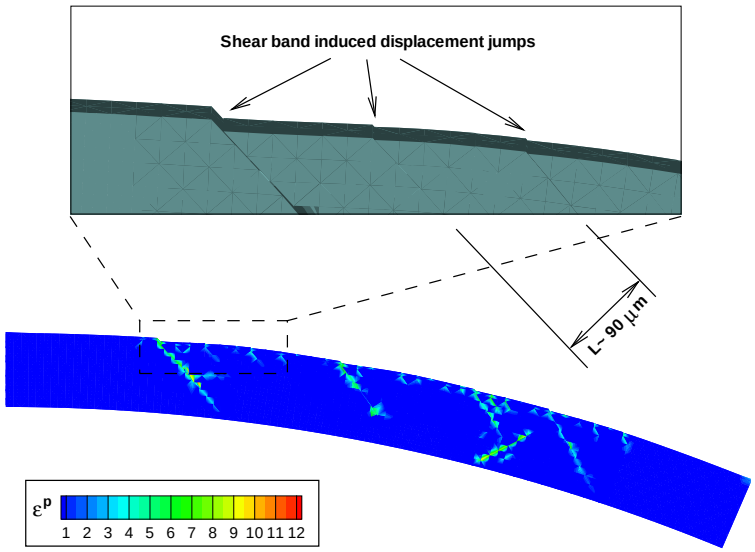

Figure 4.12: Finite element simulation of BMG plate in bending. Contours of effective plastic strain. The calculated shear band spacing is about 15% of the plate thickness (inset).

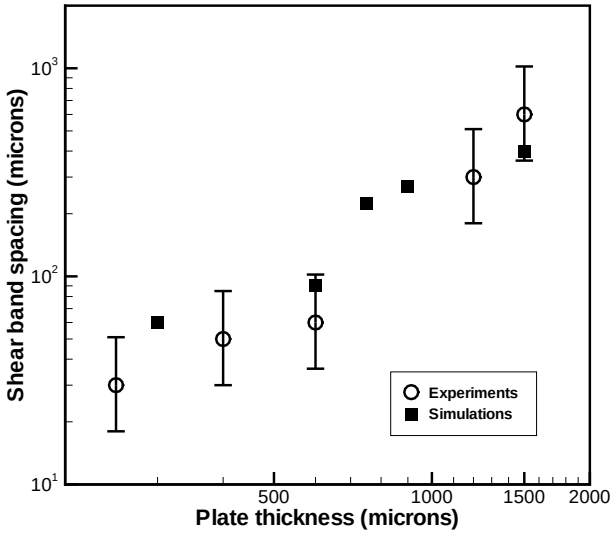

Figure 4.13: Shear band spacing as a function of plate thickness. Experimental data are taken from [28].

Chapter 5

Conclusions and future work

We have developed a variational formulation for general coupled thermomechanical problems in dissipative materials including finite elastic and plastic deformation, non-Newtonian viscosity, rate sensitivity, arbitrary flow and hardening rule, and heat conduction. We show that there exists a potential function such that both energy conservation and linear momentum balance are the Euler-Lagrange equations of its first variation. The time-discretized version of the variational formulation generalizes the isothermal approach [12] under a variational thermodynamic framework. Based on the variational formulation, heat equation for thermoelasto-viscoplastic materials is then studied as one of the Euler-Lagrange equations obtained from the first variation of an energy potential, and the temperature rise thus calculated in a one-dimensional case is compared with experimental data [20]. In addition, we discuss briefly the energy-momentum tensor and its configurational forces introduced by the existence of a thermal potential in the variational formulation.

As an important application , we have used the variational formulation to optimize the shear band thickness in strain localization process. We show that this optimization takes the form of a configurational-force equilibrium and results in a well-defined band thickness. We further implement displacement discontinuities into a class of strain-localization finite elements. These elements consist of two surfaces, attached to the abutting volume elements, which can separate and slip relative to each other, and thus enable the accurate and efficient simulation of the dynamical formation of stain localization. The predictive ability of the approach is demonstrated by means of simulations of Guduru *et al.* [22] dynamic shear-band tests in pre-notched C300 steel specimens.

Following the variational framework, we also present a finite-deformation continuum model for bulk metallic glasses. By modeling free volume as an order parameter in the proposed staggered

solution procedure, we show that it is the increase of free volume (and thus the decrease of viscosity) that plays an important role in the strain softening of bulk metallic glasses, while temperature rise itself accelerates the localization of the deformation. The model reproduces the constitutive behavior of Vitreloy 1 bulk metallic glass at various strain rates and temperatures [27]. Further validation is obtained by finite element simulation of shear banding in a Vitreloy 1 plate subjected to symmetric bending [28].

Nevertheless, the power of variational principles is far from being fully exploited. In order to take advantage of these variational principles, some of the extensions and enhancements may include:

1. Powerful theories in calculus of variations could be used to study the existence and uniqueness of solutions when the governing equations are rephrased in a form of variational potential functional [123, 124]. In this case, quasi-convexity or rank-one convexity of the pseudo-thermoelastic strain energy density can be studied, with applications to bifurcation and strain localization of materials.

2. The simplicity of the strain-localization element introduced in Chapter 3, which is designed to simply bridge volume elements, is also the source of the main limitation of the method, namely, that the singular set, e.g., the shear band path, is restricted by the computational mesh. This difficulty can be obviated by an appropriate choice of mesh in cases where the singular set is known beforehand. In the general case, the optimality of the singular set can be ensured by means of mesh adaption. A particularly appealing approach consists of extending the minimum principle which governs the solution to include the nodal positions in the reference configuration [125]. In this approach, the same variational principle yields the solution, the optimal mesh, and, by extension, the optimal singular set.

3. Instead of treating the free volume, which plays an important role in the deformation of bulk metallic glasses, as an order parameter, it is possible to embed it into a variational framework such that its evolution also obeys a rule of minimum principle. This could be done by rephrasing the generation-diffusion equation into a energy potential form akin to the way of dealing with heat conduction, which then serves as a basis for variational shear band

thickness update for bulk metallic glasses.

Finally, the predictive ability of strain-localization finite elements should see its future as a powerful tool in simulating complex dynamic behavior of materials, including shear banding, cracking and fragmentation, by combining them with other finite element strategies such as cohesive elements [21, 126], contact algorithms [127], mesh adaption [125] and parallel techniques [128].

Bibliography

[1] J.T. Oden and J.N. Reddy. *Variational methods in theoretical mechanics*. Springer-Verlag, 1976.

[2] O.C. Zienkiewicz and R.L. Taylor. *The finite element method*, volume 1, Basic formulation and linear problems. McGraw-Hill book company, forth edition, 1991.

[3] C. Miehe. Strain-driven homogenization of inelastic microstructures and composites based on an incremental variational formulation. *International Journal for Numerical Methods in Engineering*, 55:1285–1322, 2002.

[4] R. Verfürth. *A review of a posteriori error estimation and adaptive mesh-refinement techniques*. John Wiley & Sons and B. G. Teubner Publishers, New York, NY, 1996.

[5] T. Belytschko and M. Tabbara. H-adaptive finite element methods for dynamic problems, with emphasis on localization. *International Journal for Numerical Methods in Engineering*, 36:4245–4265, 1993.

[6] A.M. Cuitino and M. Ortiz. A material-independent method for extending stress update algorithms from small-strain plasticity to finite plasticity with multiplicative kinematics. *Engineering Computations*, 9:437–451, 1992.

[7] N.S. Lee and K.J. Bathe. Error indicators and adaptive remeshing in large deformation finite element analysis. *Finite Elements in Analysis and Design*, 16:99–139, 1993.

[8] M. Ortiz and J. J. Quigley. Adaptive mesh refinement in strain localization problems. *Computer Methods in Applied Mechanics and Engineering*, 90:781–804, 1991.

[9] R. Radovitzky and M. Ortiz. Error estimation and adaptive meshing in strongly nonlinear dynamic problems. *Computer Methods in Applied Mechanics and Engineering*, 172:203–240, 1999.

[10] W. Han, S. Jensen, and B.D. Reddy. Numerical approximations of problems in plasticity: error analysis and solution algorithms. *Numerical Linear Algebra Applications*, 4:191–204, 1997.

[11] W. Han, B.D. Reddy, and G.C. Schroeder. Qualitative and numerical analysis of quasi-static problems in elstoplasticity. *SIAM Journal of Numerical Analysis*, 34:143–177, 1997.

[12] M. Ortiz and L. Stainier. The variational formulation of viscoplastic constitutive updates. *Computer Methods in Applied Mechanics and Engineering*, 171(3-4):419–444, 1999.

[13] M.A. Biot. Thermoelasticity and irreversible therodynamics. *Journal of Statistical Physics*, 27:250–253, 1956.

[14] G. Herrmann. On variational principles in thermoelasticity and heat conduction. *Quarterly of Applied Mathematics*, 22:151–155, 1963.

[15] M. Ben-Amoz. On a variational theorem in coupled thermoelasticity. *Journal of Applied Mechanics*, 32:943–945, 1965.

[16] G. Batra. On a principle of virtual work for thermo-elastic bodies. *Journal of Elasticity*, 21:131–146, 1989.

[17] J.C. Simo and C. Miehe. Associative coupled thermoplasticity at finite strains: Formulation, numerical analysis and implementation. *Computer Methods in Applied Mechanics and Engineering*, 98:41–104, 1992.

[18] F. Armero and J.C. Simo. A priori stability estimates and unconditionally stable product formula algorithms for nonlinear coupled thermoplasticity. *International Journal of Plasticity*, 9:749–782, 1993.

[19] M.M. Vainberg. *Variational methods for the study of nonlinear operators.* Holden-Day, Inc, 1964.

[20] J. Hodowany, G. Ravichandran, A.J. Rosakis, and P. Rosakis. Partition of plastic work into heat and stored energy in metals. *Experimental Mechanics*, 40(2):113–123, 2000.

[21] M. Ortiz and A. Pandolfi. Finite-deformation irreversible cohesive elements for three-dimensional crack-propagation analysis. *International Journal for Numerical Methods in Engineering*, 44:1267–1282, 1999.

[22] P.R. Guduru, A.J. Rosakis, and G. Ravichandran. Dynamic shear bands: an investigation using high speed optical and infrared diagnostics. *Mechanics of Materials*, 33:371–402, 2001.

[23] S. Aubry, M. Fago, and M. Ortiz. A constrained sequential-lamination algorithm for the simulation of sub-grid microstructure in martensitic materials. *Computer Methods in Applied Mechanics and Engineering*, 192:2823–2843, 2003.

[24] M. Ortiz, E.A. Repetto, and L. Stainier. A theory of subgrain dislocation structures. *Journal of the Mechanics and Physics of Solids*, 48:2077–2114, 2000.

[25] S. Aubry and M. Ortiz. The mechanics of deformation-induced subgrain-dislocation structures in metallic crystals at large strains. *Proceedings of the Royal Society of London*, 451:3131–3158, 2003.

[26] W.L. Johnson. Bulk glass-forming metallic alloys: science and technology. *MRS Bulletin*, October:42–56, 1999.

[27] J. Lu. *Mechanical behavior of a bulk metallic glass and its composite over a wide range of strain rates and temperatures.* PhD thesis, California Institute of Technology, 2002.

[28] R.D. Conner, W.L. Johnson, N.E. Paton, and W.D. Nix. Shear bands and cracking of metallic glass in bending. *Journal of Applied Physics*, 94:904–911, 2003.

[29] B.D. Coleman and W. Noll. The thermodynamics of elastic materials with heat conduction and viscosity. *Archive for Rational Mechanics and Analysis*, 13(3):167–178, 1963.

[30] E.H. Lee. Elastic-plastic deformation at finite strains. *Journal of Applied Mechanics*, 36, 1969.

[31] J. Lubliner. On the thermodynamic foundations of non-linear solid mechanics. *International Journal of Non-Linear Mechanics*, 7:237–254, 1972.

[32] J.R. Rice. Inelastic constitutive relations for solids: an internal-variable theory and its applications to metal plasticity. *Journal of the Mechanics and Physics of Solids*, 19:433, 1971.

[33] G.I. Taylor and H. Quinney. The latent heat remaining in a metal after cold working. *Proceedings of the Royal Society of London*, A163:157–181, 1937.

[34] G.T. Camacho and M. Ortiz. Adaptive Lagrangian modelling of ballistic penetration of metallic targets. *Computer Methods in Applied Mechanics and Engineering*, 142:269–301, 1997.

[35] T.D. Marusich and M. Ortiz. Modelling and simulation of high-speed machining. *International Journal for Numerical Methods in Engineering*, 38:3675–3694, 1995.

[36] J.J. Mason, A.J. Rosakis, and G. Ravichandran. On the strain and strain-rate dependence of plastic work converted to heat: an experimental study using high-speed infrared detectors and the kolsky bar. *Mechanics of Materials*, 17:135–145, 1994.

[37] J. Hodowany, G. Ravichandran, A.J. Rosakis, and P. Rasakis. Partition of plastic work into heat and stored energy in metals. *Experimental Mechanics*, 40:113–123, 2000.

[38] P. Rosakis, A.J. Rosakis, G. Ravichandran, and J. Hodowany. A thermodynamic internal variable model for the partition of plastic work into heat and stored energy in metals. *Journal of the Mechanics and Physics of Solids*, 48(3):581–607, 2000.

[39] M.A. Meyers. *Dynamic behavior of materials*. New York: Wiley, 1994.

[40] J.D. Matthew. *Titanium – A technical guide*. ASM, 2000.

[41] J.D. Eshelby. The elastic energy-momentun tensor. *Journal of Elasticity*, 5:321–335, 1975.

[42] J.R. Rice. A path independent integral and the approximate analysis of strain concentration by notches and cracks. *Journal of Applied Mechanics*, 35:379, 1968.

[43] A.C. Palmer and J.R. Rice. The growth of slip surfaces in the progressive failure of over-consolidated clay. *Proceedings of the Royal Society of London*, 332:527, 1973.

[44] S. Sagat, C.K. Chow, M.P. Puls, and C.E. Coleman. Delayed hydride cracking in zirconium alloys in a temperature gradient. *Journal of Nuclear Materials*, 279:107–117, 2000.

[45] J.H. Brunton, J.E. Field, G.P. Thomas, and M.P.W. Wilson. The deformation of metals by high velocity impact. *Metals for the Space Age, Plansee Proceedings 1964*, pages 137–148, 1965.

[46] M.E. Backman. Damage mechanics and terminal ballistics research. Technical report, US Naval Weapons Center, China Lake, California, 1969.

[47] J.V. Craig and T.A. Stock. Microstructural damage adjacent to bullet holes in 70-30 brass. *Journal of the Australasian Institute of Metals*, 15:1–5, 1970.

[48] T.A.C. Stock and K.R.L. Thompson. Penetration of aluminium alloys by projectiles. *Metal. Trans.*, 1:219–224, 1970.

[49] M.E. Backman and S.A. Finnegan. The propagation of adiabatic shear band. *Metallurgical Effects of High Strain Rates*, 16:531–543, 1973.

[50] A.L. Wingrove. Influence of projectile geometry on adiabatic shear and target failure. *Metallurgical Transactions*, 4:1829–1833, 1973.

[51] H.C. Rogers. Adiabatic plastic deformation. *Annual Review of Materials Science*, 9:283–311, 1979.

[52] P.W. Leech. Observations of adiabatic shear band formation in 7039 aluminum-alloy. *Metallurgical Transactions A*, 10:1900–1903, 1985.

[53] S.P. Timothy. The structure of adiabatic shear bands in metals: A critical review. *Acta Metallurgica*, 35:301–306, 1987.

[54] L.S. Costin, E.E. Crisman, R.H. Hawley, and J. Duffy. On the localization of plastic flow in mild steel tubes under dynamic torsional loading. *Proc. 2nd Conference on the Mechanical Poperties of Materials at High Rates of Strain*, pages 90–100, 1979.

[55] K.A. Hartley. *Temperature profile measurement during shear band formation in steels at high strain rates.* PhD thesis, Brown University, 1986.

[56] K.A. Hartley, J. Duffy, and R.H. Hawley. Measurementof the temperature profile during shear band formation in steels deforming at high strain rates. *Journal of the Mechanics and Physics of Solids*, 35:283–301, 1987.

[57] A. Marchand and J. Duffy. An experimental-study of the formation process of adiabatic shear bands in a structural-steel. *Journal of the Mechanics and Physics of Solids*, 36:251–end, 1988.

[58] K. Cho, S. Lee, S.R. Nutt, and J. Duffy. Adiabatic shear band formation during dynamic torsional deformation of an HY-100 steel. *Acta Metallurgica et Materialia*, 41:923–932, 1993.

[59] T.W. Wright and R.C. Batra. Further results on the initiation and growth of adiabatic shear bands at high-strain rates. *Journal de physique-Paris*, 46:323–330, 1985.

[60] G. Gioia and M. Ortiz. The morphology and folding patterns of buckling-driven thin-film blisters. *Journal of the Mechanics and Physics of Solids*, 42:531–559, 1994.

[61] M. Zhou, A.J. Rosakis, and G. Ravichandran. Dynamically propagating shear bands in impact-loaded prenotched plates. 1. Experimental investigations of temperature signatures and propagation speed. *Journal of the Mechanics and Physics of Solids*, 44(6):981–1006, 1996.

[62] M. Zhou, A.J. Rosakis, and G. Ravichandran. Dynamically propagating shear bands in impact-loaded prenotched plates. 2. Numerical simulations. *Journal of the Mechanics and Physics of Solids*, 44(6):1007–1025, 1996.

[63] R. Dormeval. The adiabatic shear phenomenon. *Materials at High Strain Rates*, pages 47–70, 1987.

[64] G.R. Johnson, J.M. Hoegfeldt, U.S. Lindholm, and A. Naguy. Response of various metals to large torsional strains over a large range of strains rates, parts 1 and 2. *Journal of Engineering Materials and Technology*, 105:42–53, 1983.

[65] X.L. Huang. *Deformed shear bands and ductile fracture*. PhD thesis, Institute of Mechanics, Beijing, 1987.

[66] J.H. Giovanola. Adiabatic shear loading under pure shear loading, parts 1 and 2. *Mechanics of Materials*, 7:59–87, 1988.

[67] Y.B. Xu, Z.G. Wang, X.L. Huang, D. Xing, and Y.L. Bai. Microstructure of shear localization in low carbon ferrite-pearlite steel. *Materials Science and Engineering*, A114:81–87, 1989.

[68] I. Vardoulakis. Bifurcation analysis of the triaxial test on sand samples. *Acta Mechanica*, 32(1-3):35–54, 1979.

[69] I. Vardoulakis and B. Graf. Calibration of constitutive models for granular-materials using data from biaxial experiments. *Geotechnique*, 35(3):299–317, 1985.

[70] Y. Leroy and M. Ortiz. Localization analysis under dynamic loading. *Institute of Physics Conference Series*, 102:257–265, 1989.

[71] Y. Leroy and M. Ortiz. Finite-element analysis of transient strain localization phenomena in frictional solids. *International Journal for Numerical and Analytical Methods in Geomechanics*, 14(2):93–124, 1990.

[72] H.C. Rogers. Tensile fracture of ductile metals. *Transanctions of Metallurgical Society A.I.M.E.*, 218:498–506, 1960.

[73] C.D. Beachem. Electron fractographic study of influence of plastic strain conditions upon ductile rupture processes in metals. *Transactions of the American Society of Metals*, 56:318–326, 1963.

[74] J. Gurland and J. Plateau. Mechanism of ductile rupture of metals containing inclusions. *Transactions of the American Society of Metals*, 56:442–455, 1963.

[75] C.D. Beachem and G.R. Yoder. Elasto-plastic fracture by homogeneous microvoid coalescence tearing along alternating shear planes. *Metallurgical Transactions*, 4:1145–1153, 1973.

[76] T.B. Cox and J.R. Low. Investigation of the plastic fracture of Aisi 4340 and 18 Nickel-200 grade maraging steels. *Metallurgical Transactions*, 5:1457–1470, 1974.

[77] J.Q. Clayton and J.F. Knott. Observations of fibrous fracture modes in a prestrained low-alloy steel. *Metal Science*, 10:63–71, 1976.

[78] V. Tvergaard. Material failure by void growth to coalescence. *Advances in Applied Mechanics*, 27:83–151, 1990.

[79] M. Ortiz, Y. Leroy, and A. Needleman. A finite-element method for localized failure analysis. *Computer Methods in Applied Mechanics and Engineering*, 61(2):189–214, 1987.

[80] J.F. Molinari and M. Ortiz. Three-dimensional adaptive meshing by subdivision and edge-collapse in finite-deformation dynamic-plasticity problems with application to adiabatic shear banding. *International Journal for Numerical Methods in Engineering*, 53(5):1101–1126, 2002.

[81] S. Jun and S. Im. Multiple-scale meshfree adaptivity for the simulation of adiabatic shear band formation. *Computational Mechanics*, 25:257–266, 2000.

[82] S. Li, W.K. Liu, D. Qian, P.R. Guduru, and A.J. Rosakis. Dynamic shear band propagation and micro-structure of adiabatic shear band. *Computer Methods in Applied Mechanics and Engineering*, 191:73–92, 2001.

[83] S. Li, W.K. Liu, A.J. Rosakis, T. Belytschko, and W. Hao. Mesh-free galerkin simulations of dynamic shear band propagation and failure mode transition. *International Journal of Solids and Structures*, 39:1213–1240, 2002.

[84] J.C. Simo and T.J.R. Hughes. *Computational inelasticity*. New York: Springer, 1997.

[85] G. Gioia and M. Ortiz. The two-dimensional structure of dynamic boundary layers and shear bands in thermoviscoplastic solids. *Journal of the Mechanics and Physics of Solids*, 44(2):251–292, 1996.

[86] T.W. Wright and G. Ravichandran. Canonical aspects of adiabatic shear bands. *International Journal of Plasticity*, 13(4):309–325, 1997.

[87] Q. Xue, M.A. Meyers, and V.F. Nesterenko. Self-organization of shear bands in titanium and Ti-6Al-4V alloy. *Acta Materialia*, 50:575–596, 2002.

[88] J.C. Simo and D.D. Fox. On a stress resultant geometrically exact shell model. 1. Formulation and optimal parametrization. *Computer Methods in Applied Mechanics and Engineering*, 72:267–304, 1989.

[89] J.C. Simo, D.D. Fox, and M.S. Rifai. On a stress resultant geometrically exact shell model. 2. The linear-theory – computational aspects. *Computer Methods in Applied Mechanics and Engineering*, 73:53–92, 1989.

[90] A.-S. Bonnet-Lebouvier, A. Molinari, and P. Lipinski. Analysis of the dynamic propagation of adiabatic shear bands. *International Journal of Solids and Structures*, 39:4249–4269, 2002.

[91] W. Klement, R.H. Willens, and P. Duwez. Non-crystalline structure in solidified gold-silicon alloys. *Nature*, 187:869–870, 1960.

[92] A. Peker and W.L. Johnson. A highly processable metallic glass: $Zr_{41.2}Ti_{13.8}Cu_{12.5}Ni_{10}Be_{22.5}$. *Applied Physics Letters*, 63:2342–2344, 1993.

[93] H.A. Bruck, T. Christman, A.J. Rosakis, and W.L. Johnson. Quasi-static constitutive behavior of $Zr_{41.2}Ti_{13.8}Cu_{12.5}Ni_{10}Be_{22.5}$ bulk amorphous alloys. *Acta Materialia*, 30:4296–434, 1994.

[94] H.A. Bruck, A.J. Rosakis, and W.L. Johnson. The dynamic compressive behavior of beryllium bearing bulk metallic glasses. *Journal of Materials Research*, 11:503–511, 1996.

[95] R.D. Conner, A.J. Rosakis, W.L. Johnson, and D.M. Owen. Fracture toughness determination for a beryllium-bearing bulk metallic glass. *Scripta Metallurgica*, 37(1373-1378), 1997.

[96] P. Lowhaphandu, L.A. Ludrosky, A.L. Motgomery, and J.J. Lewandowski. Deformation and fracture toughness of a bulk amorphous Zr-Ti-Ni-Cu-Be alloy. *Intermetallics*, 8:487–492, 2000.

[97] G. Subhash, R.J. Dowding, and L.J. Kecskes. Characterization of uniaxial compressive response of bulk amorphous Zr-Ti-Cu-Ni-Be alloy. *Materials Science and Engineering*, A334:33–40, 2002.

[98] J. Lu, G. Ravichandran, and W.L. Johnson. Deformation behavior of the $Zr_{41.2}Ti_{13.8}Cu_{12.5}Ni_{10}Be_{22.5}$ bulk metallic glass over a wide range of strain-rates and temperatures. *Acta Materialia*, 51:3429–3443, 2003.

[99] W.J. Johnson. Bulk amorphous metal – an emerging engineering material. *Journal of Materials*, March:40–43, 2002.

[100] R. Busch, A. Masuhr, and W.L. Johnson. Thermodynamics and kinetics of Zr-Ti-Cu-Ni-Be bulk matallid glass forming liquids. *Materials Science and Engineering*, A304-306:97–102, 2001.

[101] M.H. Cohen and G.S. Grest. Liquid-glass transition, a free-volume approach. *Physics Review B*, 20(3):1077–1098, 1979.

[102] A. Masuhr, R. Busch, and W.L. Johnson. Thermodynamics and kinetics of the $Zr_{41.2}Ti_{13.8}Cu_{12.5}Ni_{10}Be_{22.5}$ bulk metallic glass forming liquid: glass formation from a strong liquid. *Journal of Non-Crystalline Solids*, 250-252:566–571, 1999.

[103] A. Masuhr, T.A. Waniuk, R. Busch, and W.L. Johnson. Time scales for viscous flow, atomic tranport, and crystallization in the liquid and supercooled liquid states of $Zr_{41.2}Ti_{13.8}Cu_{12.5}Ni_{10}Be_{22.5}$. *Physical Review Letters*, 82:2290–2293, 1999.

[104] W.L. Johnson, J. Lu, and M.D. Demetriou. Deformation and flow in bulk metallic glasses and deeply undercooled glass forming liquids – a self consistent dynamic free volume model. *Intermerallics*, 10:1039–1046, 2002.

[105] M.H. Chen and M. Goldstein. Anomalous viscoelastic behavior of metallic glasses of Pd-Si-based alloys. *Journal of Applied Physics*, 43(1642-&), 1972.

[106] F. Spaepen. A microscopic mechanism for steady state inhomogeneous flow in metallic glasses. *Acta Metallurgica*, 25:407–415, 1977.

[107] A.S. Argon. Plastic deformation in metallic glasses. *Acta Metallurgica*, 27:47–58, 1979.

[108] P.S. Steif, F. Spaepen, and J.W. Hutchinson. Strain localization in amorphous metals. *Acta Metallurgica*, 30:447–455, 1982.

[109] H.J. Leamy, H.S. Chen, and T.T. Wang. Plastic flow and fracture of metallic glass. *Metallurgical Transactions*, 3:699–&, 1972.

[110] W.J. Wright, R. Saha, and W.D. Nix. Deformation mechanics of the $Zr_{40}Ti_{14}Ni_{10}Cu_{12}Be_{24}$ bulk metallic glass. *Metallurgical Transactions*, 42:642–649, 2001.

[111] R. Huang, Z. Suo, J.H. Prevost, and W.D. Nix. Inhomogeneous deformation in metallic glasses. *Journal of the Mechanics and Physics of Solids*, 50:1011–1027, 2002.

[112] M. Ortiz, R.A. Radovitzky, and E.A. Repetto. The computation of the exponential and logarithmic mappings and their first and second linearizations. *International Journal for Numerical Methods in Engineering*, 52:1431–1441, 2001.

[113] M.H. Cohen and D. Turnbull. Molecular transport in liquids and glasses. *Journal of Chemical Physics*, 31:1164–1169, 1959.

[114] D. Turnbull and M.H. Cohen. Free-volume model of the amorphous phase: Glass transition. *Journal of Chemical Physics*, 34:120–125, 1961.

[115] D. Turnbull and M.H. Cohen. On the free-volume model of the liquid-glass transition. *Journal of Chemical Physics*, 52:3028–3041, 1970.

[116] A.I. Taub. Threshold stresses in amorphous-alloys. 1. Flow. *Acta Metallurgica*, 30(12):2117–2127, 1982.

[117] A.I. Taub. Threshold stresses in amorphous-alloys. 2. Structural relaxation. *Acta Metallurgica*, 30(12):2129–2133, 1982.

[118] D.E. Polk and D. Turnbull. Flow of melt and glass forms of metallic alloys. *Acta Metallurgica*, 20(4):593–&, 1972.

[119] K.M. Flores and R.H. Dauskardt. Mean stress effects on flow localization and failure in bulk metallic glass. *Acta Materialia*, 49(2527-2537), 2001.

[120] W.J. Wright, T.C. Hufnagel, and W.D. Nix. Free volume coalescence and void formation in shear bands in metallic glass. *Journal of Applied Physics*, 93(3):1432–1437, 2003.

[121] G. I. Taylor and H. Quinney. The plastic distortion of metals. *Philosophical Transactions of the Royal Society of London A*, 230:323–362, 1931.

[122] J. Lemonds and A. Needleman. Finite-element analyses of shear localization in rate and temperature-dependent solids. *Mechanics of Materials*, 5(4):339–361, 1986.

[123] J.E. Marsden and T.J.R. Hughes. *Mathematical foundations of elasticity*. Prentice-Hall, Englewood Cliffs, N.J., 1983.

[124] M. Silhavy. *The mechanics and thermodynamic of continuous media*. New York: Springer, 1997.

[125] P. Thoutireddy and M. Ortiz. A variational r-adaption and shape-optimization for finite-deformation elasticity. *International Journal for Numerical Methods in Engineering*, 60, 2004. to appear.

[126] C. Yu, A. Pandolfi, M. Ortiz, D. Coker, and A.J. Rosakis. Three-dimensional modeling of intersonic shear-crack growth in asymmetrically loaded unidirectional composite plates. *International Journal of Solids and Structures*, 39(25):6135–6157, 2002.

[127] C. Kane, E. A. Repetto, M. Ortiz, and J. E. Marsden. Finite element analysis of nonsmooth contact. *Computer Methods in Applied Mechanics and Engineering*, 180:1–26, 1999.

[128] W. Gropp, E. Lusk, and A. Skiellum. *Using MPI – Portable paraller programming with the message-passing interface*. The MIT Press, Cambridge, Massachustts, second edition, 1999.